João Pedro de Sousa Oliveira

Licenciado em Engenharia de Materiais

Correlation Between the Mechanical Cycling Behavior and Microstructure in Laser Welded Joints Using NiTi Memory Shape Alloys

Dissertação para obtenção do Grau de Mestre em Engenharia de Materiais

Orientador: Doutor Francisco Manuel Braz Fernandes, Professor Associado com Agregação, Faculdade de Ciências e Tecnologia da Universidade Nova de Lisboa

Co-orientador: Doutora Rosa Maria Mendes Miranda, Professora Associada com Agregação, Faculdade de Ciências e Tecnologia da Universidade Nova de Lisboa

Júri:

Presidente:	Prof. Doutor Rui Jorge Cordeiro Silva
Arguente:	Prof. Doutora Maria Luísa Coutinho Gomes de Almeida
Vogais:	Prof. Doutor Francisco Manuel Braz Fernandes
	Prof. Doutora Rosa Maria Mendes Miranda

FACULDADE DE CIÊNCIAS E TECNOLOGIA
UNIVERSIDADE NOVA DE LISBOA

Julho 2012

Correlation Between the Mechanical Cycling Behavior and Microstructure in Laser Welded Joints Using NiTi Memory Shape Alloys

Agradecimentos

Este trabalho não poderia ter sido realizado sem a ajuda e colaboração dos meus orientadores: Professor Doutor Braz Fernandes e Professora Doutora Rosa Miranda. O seu apoio foi fundamental para a realização deste trabalho e tenho de agradecer por toda a ajuda que me prestaram, disponibilidade total para esclarecer as dúvidas que foram surgindo ao longo deste trabalho e pela sua amizade.

Gostaria de agradecer ao financiamento da FCT/MCTES para o projecto 'Joining micro to small scale systems in shape memory alloys using last generation infrared lasers' (PTDC/EME-TME/100990/2008).

Agradeço o apoio de DESY para o tempo de feixe I-20100250 EC na linha P-07 (HEMS, PETRA-III).

Quero também agradecer à Joana Duarte pela companhia que me foi fazendo e amizade que me deu durante estes anos. Não posso deixar de recordar os meus colegas que me foram acompanhando ao longo destes anos: Ruben Raposo, Salomé Moço, Andreia Alexandrino, Sara Gil e todos os outros que aqui não refiro. Ao Dr. Mahesh um agradecimento pela ajuda que foi dando ao longo desta tese.

Aos meus pais, por todo o seu apoio e por me terem providenciado tudo aquilo que necessitei e que me permitiu chegar até aqui. Grande parte deste trabalho é para eles.

Por último, mas talvez mais a importante, quero agradecer à Andreia. Foi ela que me possibilitou a estabilidade para fazer este trabalho e foi um grande suporte ao longo destes 5 anos. Obrigado!

Acknowledgments

This work would not be possible with the help and collaboration of my supervisors: Professor Braz Fernandes and Professor Rosa Miranda. Their support was fundamental and essential for this work and I have to thank them for all their help, total availability to answer my questions and by their friendship.

I would like to thank the funding of FCT/MCTES for the project 'Joining micro to small scale systems in shape memory alloys using last generation infrared lasers' (PTDC/EME-TME/100990/2008).

Support from DESY for the beamtime I-20100250 EC at beamline P-07 (HEMS, PETRA-III) is gratefully acknowledged.

I would like also to thank to Joana Duarte for her friendship along all these years. I must remind my colleagues: Ruben Raposo, Salomé Moço, Andreia Alexandrino, Sara Gil and all others that I do not refer here. I also thank to Dr. Mahesh for his help during this thesis.

To my parents, for all their support, and for giving me all that I needed. This allowed me to complete this stage. Great part of this work is for them.

For last, but not least, I want to express my gratitude to Andreia. She allowed the stability required for make this work and was of a great support during these 5 years. Thank you!

Aos meus pais. Por tudo.

Que um dia eu seja aquilo que me ensinaram.

Resumo

A necessidade de técnicas de união avançadas para ligas com memória de forma é algo da maior importância, pois as propriedades funcionais destas ligas, em particular o efeito memória de forma e a superelasticidade, apresentam soluções únicas para diversas aplicações. Na literatura têm-se notado esforços no sentido de promover a união destas ligas com recurso a soldadura laser, apesar dos resultados em termos das propriedades mecânicas serem, em geral, mais limitados que o material base.

Neste trabalho, o principal objectivo é a correlação da microestrutura de soldaduras laser similares de NiTi com o seu comportamento mecânico à ciclagem. Um protocolo para a ciclagem mecânica destas soldaduras foi utilizado para analisar o comportamento superelástico das soldaduras. O efeito memória de forma foi também estudado através de testes de dobragem. Estudos com difracção de raios-X permitiram a identificação das diferentes fases existentes no material base, zona termicamente afectada e na zona de fusão das soldaduras. Imagens SEM das superfícies de fractura foram também analisadas.

Foi observado o comportamento superelástico das soldaduras durante os ensaios mecânicos. O efeito memória de forma foi também observado nas soldaduras, mesmo quando estas tinham sido previamente sujeitas a ensaios de ciclagem. Os parâmetros de soldadura influenciam o comportamento mecânico à ciclagem das amostras. Em particular, existe uma gama de valores de entrega térmica introduzida durante a soldadura que permite a obtenção de um bom comportamento mecânico à ciclagem das soldaduras.

Palavras-chave: Ligas com memória de forma, NiTi, Soldadura laser, Nd:YAG, Superelasticidade, Efeito memória de forma, Difracção de raios-X

Abstract

The demand of emerging joining techniques for shape memory alloys has become of great importance, as their functional properties, namely shape memory effect and superelasticity, present unique solutions for state-of-the-art applications. Literature shows that significant efforts have been conducted on laser welding of these alloys, although very limited results concerning mechanical properties are reported.

In this study, the main objective was to correlate the microstructure of similar NiTi welds with its mechanical behavior. A set of cycling tests was used in order to analyze the superelastic behavior of the welds. Also, shape memory effect was evaluated by means of a bending and free-recovery test. X-ray diffraction analysis allowed to identify the existing phases in the base material, heat affected zone and fusion zone. SEM images of fracture surfaces were also analyzed.

It was observed the superelastic behavior of the welds during the mechanical tests. Also shape memory effect was shown to exist on welded samples even after cycling. X-ray diffraction showed a microstructural gradient across the samples. The welding parameters influence the mechanical behavior under cycling of the welds. In particular, there is a specific range of values of heat input introduced during welding that allow obtaining a good mechanical behavior under cycling of the welds.

Key-words: Shape memory alloys, NiTi, Laser welding, Nd:YAG, Superelasticity, Shape memory Effect, X-ray diffraction

Abbreviations

A_f – Austenite finish temperature

A_s – Austenite start temperature

A^{σ}_s – Start transformation temperature of austenite at a given stress

A^{σ}_f – Finish transformation temperature of austenite at a given stress

BCC – Body centered cubic

BM – Base material

FZ – Fusion zone

HAZ – Heat affected zone

HI – Heat input

M_f – Martensite finish temperature

M_s – Martensite start temperature

M^{σ}_s – Start transformation temperature of martensite at a given stress

M^{σ}_f – Finish transformation temperature of martensite at a given stress

PE – Pseudoelasticity

SE – Superelasticity / superelastic effect

SIM – Stress induced martensite

SMA – Shape memory alloy

SME – Shape memory effect

UTS – Ultimate tensile strength

σ_s – Detwinning start stress

σ_f – Detwinning finish stress

σ^{As} – Minimum stress level to start inducing the transformation from martensite to austenite

σ^{Ms} – Minimum stress level to start inducing the transformation from austenite to martensite

Ω – Permanent deformation angle

Θ – Bragg's angle

Nomenclature

DSC – Differential Scanning Calorimetry

LASER – Light Amplification by Stimulated Emission of Radiation

Nd:YAG – Neodymium-doped Yttrium Aluminum Garnet

SEM – Scanning Electron Microscopy

TIG – Tungsten Inert Gas

XRD – X-Ray Diffraction

Contents

List of Figures

List of Tables

Preâmbulo

O trabalho desenvolvimento no âmbito desta tese de mestrado visa correlacionar as características microestruturais e o comportamento mecânico à ciclagem de ligas com memória de forma Ni-Ti soldadas por laser.

Este trabalho inicia-se com uma introdução teórica sobre as ligas com memória de forma Ni-Ti e as suas características, fazendo também uma pequena introdução à soldadura laser e à sua influência na união deste tipo de ligas.

Posteriormente faz-se a apresentação dos protocolos e métodos experimentais utilizados durante a realização deste trabalho e de seguida apresentam-se os resultados obtidos.

Os resultados são discutidos com vista a poderem retirar-se conclusões relativamente à influência do processo de soldadura no comportamento mecânico à ciclagem destas ligas.

Preamble

The work developed during this Master Thesis aims to correlate de microstructural characteristics of laser welded Ni-Ti shape memory alloys and their mechanical behavior under cyclic load/unload.

This work begins with an introduction about shape memory alloys and its characteristics and with a minor introduction to laser welding and its influence in the joining of these alloys.

Next, the protocols and experimental methods used in this work are presented, followed by the presentation of the experimental results obtained.

The results are discussed in order to draw conclusions regarding the influence of the welding parameters on the mechanical behavior of these alloys under cyclic load/unload laser welded Ni-Ti shape memory alloys.

Objectivos

O presente trabalho visa estabelecer relações entre as características microestruturais apresentadas por ligações soldadas a laser de ligas Ni-Ti com memória de forma e o seu comportamento mecânico à ciclagem. Para tal, foram utilizadas técnicas de caracterização estrutural, como a difracção de raios-x, de modo a compreender o papel que os diferentes constituintes estruturais têm no desempenho final das uniões soldadas a laser, tanto quanto ao comportamento superelástico em ciclos sucessivos de carga e descarga, como para o efeito de memória de forma.

Objectives

The present work aims to establish a relation between the microstructural characteristics of laser welded NiTi joints and its mechanical behavior to cycling. Structural characterization techniques, such as x-ray diffraction have been used in order to understand the role of the different microstructural constituents on the performance of laser welded joints not only under successive loading/unloading under superelastic regime, but also for the shape memory effect.

1 - Introduction

1.1 -Shape Memory Alloys

Shape memory alloys (SMAs) are a unique class of shape memory materials with the ability to recover their shape when the temperature is increased. An increase in temperature can result in shape recovery even under high applied loads. SMAs can also absorb and dissipate mechanical energy by undergoing a reversible hysteretic shape change when subjected to applied mechanical cyclic loading. These characteristics have made SMAs very popular for applications such as sensing and actuation, absorption and vibration damping. The application of SMAs spans a wide variety of industrial sectors such as aerospace automotive, biomedical and oil exploration. [1]

Until 1949 the martensitic transformation was established as an irreversible process. However in that year Kurdjumov and Khandros presented the concept of thermoelastic martensitic transformation, which explained the reversible transformation of martensite. Their work was performed in CuZn and CuAl alloys and, some years latter, the thermoelastic martensitic transformation was demonstrated for other alloys such as InTl. Despite the discovery of the reversible martensitic transformation for different alloys, this effect was not utilized until 1963. In that year Buehler and their coworkers discovered the shape memory effect (SME) in NiTi while investigating different materials that could be used for heat shielding. [2] The term "NiTiNOL" is also connoted with NiTi in honor of its discovery at the Naval Ordnance Laboratory (NOL). The discovery of this new alloy triggered active research interest into SMAs. The effects of heat treatment, composition and microstructure were extensively investigated and began to be understood then.

Despite Ni-Ti alloys have many common characters with other SMAs by exhibiting SME, Superelasticity (SE) and two-way SME (also known as the all round SME) they also exhibit many other characteristics, which are quite unique compared to other SMAs, aside to the good mechanical properties of Ni-Ti alloys which are comparable to other engineering metals. Ni-Ti alloys exhibit quite a low elastic anisotropy as low as nearly 2, although most of the other SMAs exhibit the value of about 10 or more. The elastic constant C_{44} decreases with decreasing temperature, which is the opposite behavior in most of other shape memory and normal alloys. In addition to the properties described previously, Ni-Ti alloys also exhibit other remarkable properties. Although it is a kind of intermetallic compound, it is quite ductile, and under certain conditions 60% cold working being possible. One of the reasons for such a great ductility probably lies in the low elastic anisotropy described previously. This kind of alloys also exhibit excellent corrosion and abrasion resistance. Because of the excellent properties as the ones described above, most of the applications have been done for Ni-Ti alloys among many SMAs. Flaps in air-conditioner, coffee maker, brassiere, antennas for mobile phones, medical applications such as orthodontic wires and stents are some of the applications of Ni-Ti alloys. [3] It must be noticed that Ni-Ti alloys are also biocompatible which make them suitable for being used as part of biomedical devices. [4]

1.1.1 - Phase Diagram of the Ni-Ti System

The phase diagram of Ni-Ti alloy system is very used for heat-treatments of the alloys and improvement of their properties. This phase diagram (Figure 1) has been vastly studied and

has suffered some modifications along the time. NiTi is an intermetallic that, at low temperature, only exists in a very narrow band of compositions (near equiatomic).

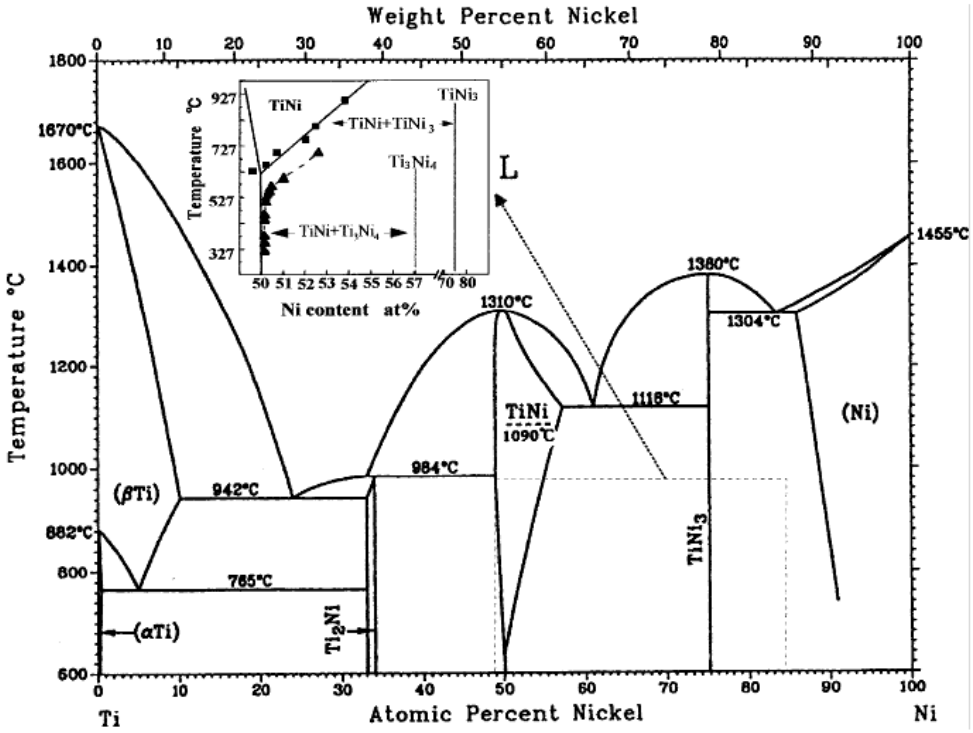

Figure 1 – Phase diagram of a Ni-Ti alloy in which is highlighted the phase equilibrium between. [3]

The phase diagram allows us to notice the existence of a stability domain of the austenitic phase (B2). This domain is characterized, for Ni-rich alloys, by a strong variation of the solubility limit with the increase of temperature. For Ti-rich alloys this variation is very slight. At low temperatures the extension of the stability domain of the austenitic phase is practically nonexistent.

Generally, SMAs have two different phases, each one with different crystal structures and, as a consequence, with different properties. The high temperature phase is called austenite and the low temperature phase is called martensite. The transformation from one structure to another does not occur by diffusion of atoms but rather by shear lattice distortion. This kind of transformation is known as martensitic transformation. Each martensitic crystal formed can have a different orientation direction, called a variant. The assembly of martensitic variants may exist in two forms: twinned martensite, which is formed by a combination of "self-accomodated" martensitic variants, and detwinned or reoriented martensite in which a specific variant is dominant.

The reversible phase transformation from austenite, also known as parent phase, to martensite, or product phase, and vice versa, form the basis for the unique behavior of SMAs. [1]

The parent phase in Ni-Ti alloys has a cubic B2 (BCC, Body Centered Cubic) structure, while martensite has a B19' (monoclinic structure). It should be noticed that in Ni-Ti alloys a third

phase could sometimes appear between austenite and martensite. That phase is called R-phase and has a trigonal structure.

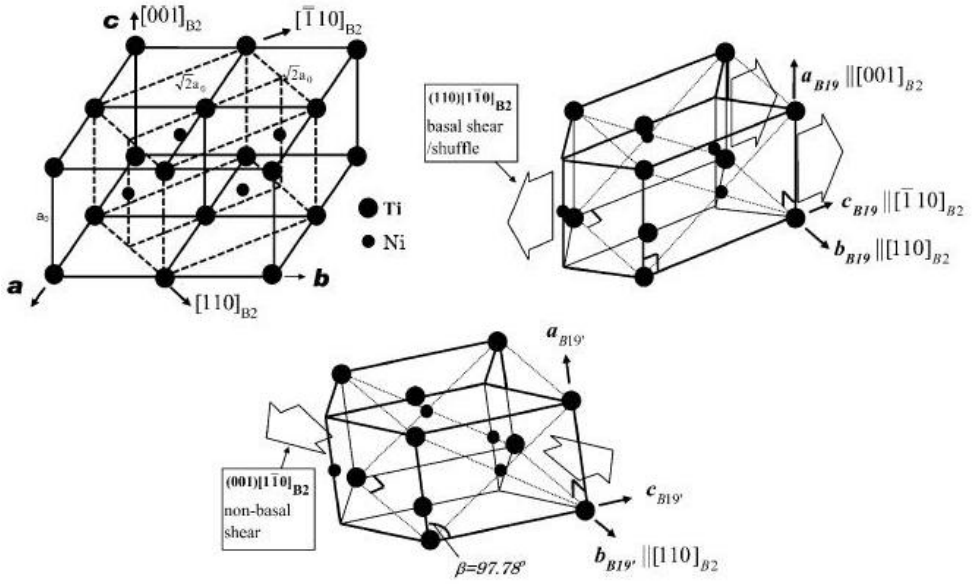

Figure 2 – Crystal structure of B2 austenite (top on the left), B19 martensite (top on the right) and B19' martensite (bottom). [3]

1.1.2 - Martensitic Transformation Temperature

Experimentally is known that the martensitic transformation temperature is strongly dependent on the composition and/or alloying elements. NiTi is not a line-compound with a fixed composition: it shows a certain capability to dissolve some excess of Ni in the Ni-rich side but cannot dissolve the excess of Ti as it is depicted in Figure 1 (almost vertical line on the Ti-rich side but Ni-rich side has some solubility, up to 6% at 1000 °C). [3]

Figure 3 shows that the transformations temperature M_s is strongly dependent on Ni concentration. However, in the Ti-rich side the transformation temperature is almost composition independent due to the fact that the solubility limit on NiTi in the Ti-rich side is practically vertical and thus is not possible to get Ti-rich Ni-Ti solid solution. This means that Ti-rich alloys will show a similar behavior as 50 at%Ni-Ti. On the Ni-rich side, an increase on the Ni content causes a drastic decrease of the transformation temperature M_s. Theoretically, this transformation temperature will drop to near 0 K when the mole fraction of Ni slightly exceeds 51.5%.

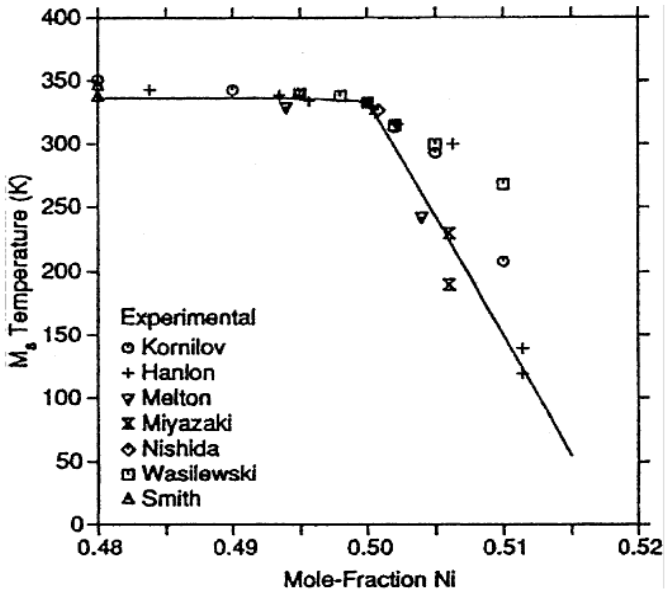

Figure 3 – Transformation temperature as a function of Ni content for binary Ni-Ti alloys. [3]

1.1.3 - Phase Transformation in SMAs

As mentioned before the reversible transformation from austenite to martensite and vice versa are the basis for the unique behavior of SMAs.

Upon cooling, and without any load applied, the crystal structure changes from austenite to martensite. This phase transition is called the forward or direct transformation. This transformation is due to the formation of several martensitic variants, which are up to 24 in Ni-Ti alloys. The arrangement of variants occurs in such a way that the average macroscopic shape change is negligible, resulting in twinned martensite. When heating from the martensite phase, there is a transformation of the crystal structure back to austenite, which is called reverse transformation. During this transformation there is no associated shape change.

The schematic of the crystal structure of twinned martensite and austenite for an SMA and the transformation between them is shown in Figure 4. During the forward transformation, without any load applied, austenite begins to transform to twinned martensite at the martensitic start temperature (M_s) and the transformation will be completed at martensite finish temperature (M_f). At this point the material is fully twinned martensite. Upon heating, the reverse transformation occurs at austenitic start temperature (A_s) and the transformation is fully completed at austenite finish temperature (A_f).

If a mechanical load is applied to the material in the twinned martensitic state it is possible to detwin the martensite by reorienting a certain number of variants (Figure 5). This detwinning process will induce a macroscopic shape change where the deformed configuration is retained when the applied load is released. A subsequent heating of the material above A_f will cause a reverse transformation from detwinned martensite to austenite which will lead to complete shape recovery (Figure 6). Cooling back to a temperature below M_f will lead to the formation of twinned martensite again with no associated shape change observed. The process described above is referred to as the SME. The load applied must be large enough to start the detwinning process. The minimum amount of stress required to the beginning of this process in termed

detwinning start stress (σ_s). The complete detwinning process will occur when the detwinning finish stress (σ_f) is reached.

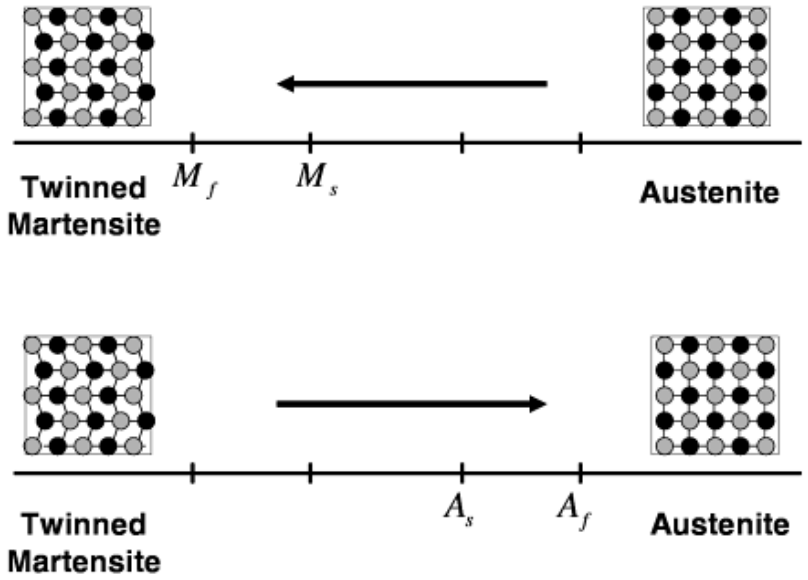

Figure 4 – Temperature-induced phase transformation of na SMA without mechanical loading. [1]

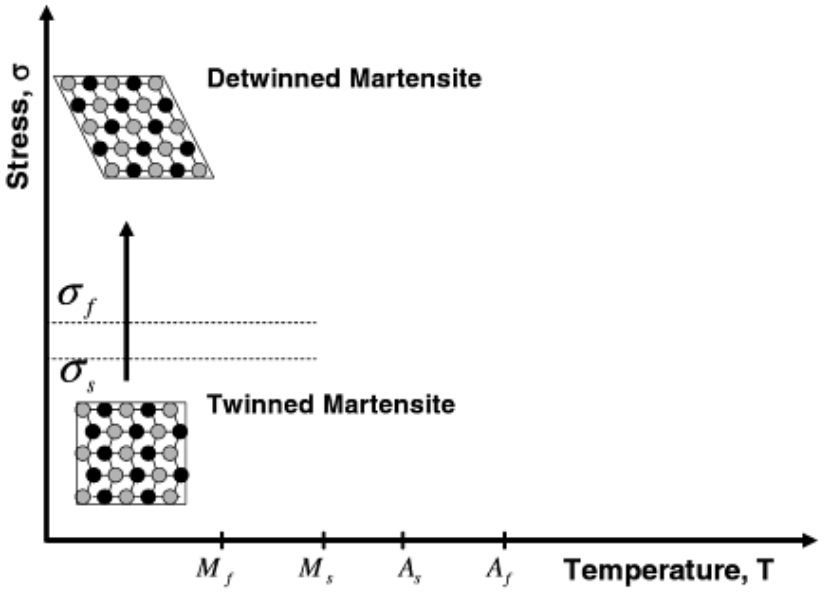

Figure 5 – Schema showing the passage from twinned to detwinned martensite. [1]

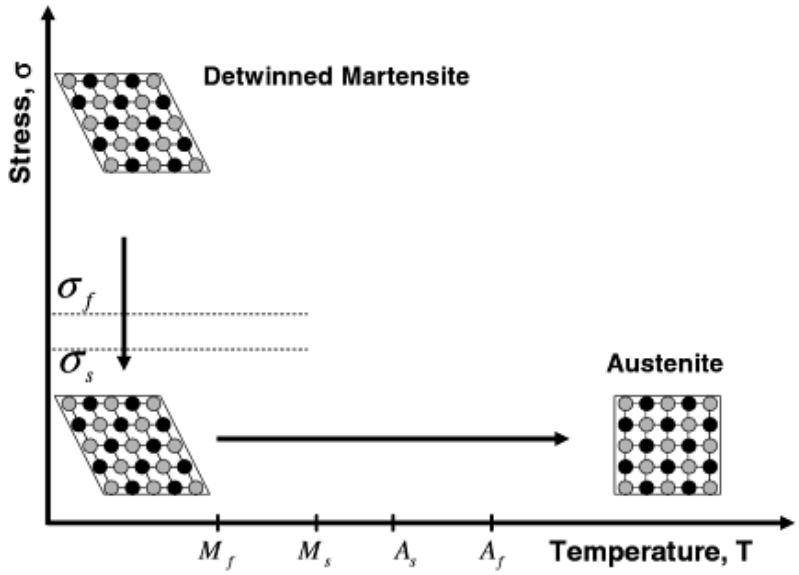

Figure 6 – Schema of the SME for an SMA. [1]

Since the forward and reverse transformations occur over a range of temperatures (M_s to M_f, A_s to A_f) for a given SMA composition, it is possible to construct transformation regions in the stress-temperature space. The transformation temperatures strongly depend on the magnitude of the applied load, with higher values of applied load leading to higher transformation temperatures, as shown in Figure 7. Under an applied uniaxial load with a corresponding stress, σ, the new transformation temperatures are represented as M^{σ}_{f}, M^{σ}_{s}, A^{σ}_{s} and A^{σ}_{f} for martensitic finish, martensitic star, austenitic star and the austenitic finish temperatures, respectively.

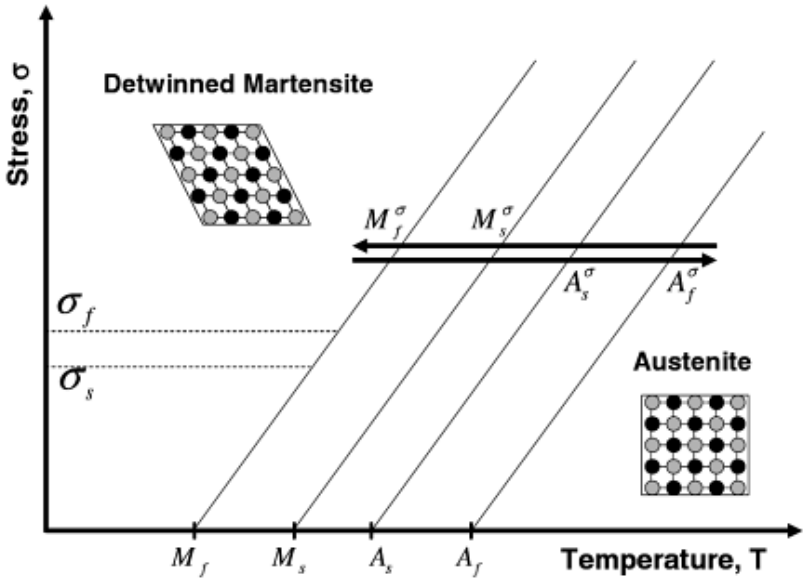

Figure 7 – Temperature-induced phase transformation in the presence of applied load. [1]

1.1.3.1 - Superelasticity

SE as well as SME is a special characteristic present in SMAs, in particular in Ni-Ti alloys.

Taking into consideration the Figure 8, it is possible to observe that, for a constant temperature above A_f, it is possible to have the stress induced phase transformation from austenite to martensite. This martensitic transformation is the basis of the superelastic effect. The load applied will give rise to a stress-induced martensite (SIM) with shape modification. It must be noticed that this martensite is detwinned martensite.

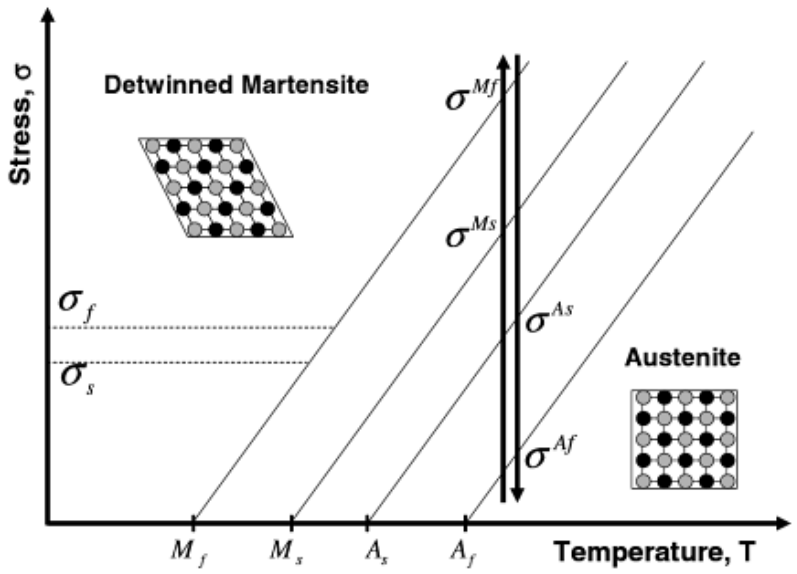

Figure 8 – Schema of superelastic effect. [1]

To illustrate the superelastic effect let us consider the cycling load presented in Figure 9. From A do B the parent phase undergoes elastic loading. Point B is the minimum stress level to start inducing the transformation from austenite to martensite (σ^{Ms}). This transformation occurs because austenite becomes unstable and SIM starts to form. [5] Note that the stress-induced transformation from austenite to martensite is accompanied by generation of large inelastic strains as shown in Figure 9. From B to C the transformation from austenite to martensite proceeds and simultaneously martensite variants are being re-oriented, meaning that we can have both twinned and detwinned martensite, but at the end we will only have detwinned martensite due to the re-orientation of twinned martensite during this stage. At point C we reach the stress level where the martensitic transformation is over (σ^{Mf}). From C to D there is the elastic loading of the detwinned martensite. By decreasing the stress applied during unloading, martensite will unload (elastically) from point D to E. Point E marks the beginning of the transformation from detwinned martensite do austenite (σ^{As}). The reverse transformation occurs due to the thermodynamic destabilization of martensite. This process is accompanied by the recovery of the strain due to phase transformation at the end of unloading. At point F we reach the complete transformation from martensite to austenite and the material will continue to unload until A. Note that if after point D we kept raising the stress level, we would only cause the plastic deformation of the detwinned martensite.

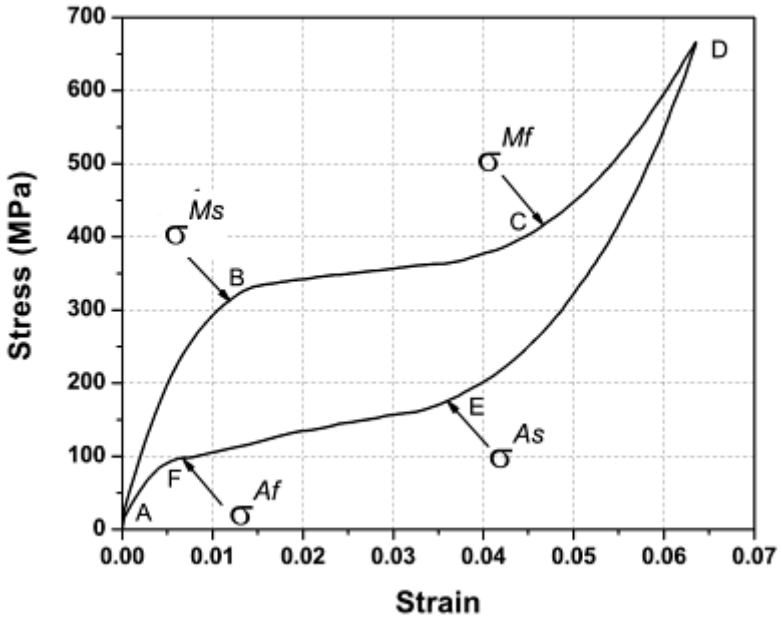

Figure 9 – Typical SMA superelastic cycling load. [1]

The hysteresis loop represented in the σ-ε space represents the energy dissipated in the transformation cycle.

Figure 10 depicts a typical stress-strain curve for initially fully austenitic Ni-Ti alloy. This curve is characterized by a Lüders-like deformation, which only appears during deformation in tension, associated to the martensitic transformation induced by stress (Stage II). The Lüders-like deformation occurs due to the propagation of deformation in macroscopic shear bands. [6] The stress-strain curve usually is divided in four different stages: Stage I – ideal linear behavior from austenite; Stage II – martensitic transformation induced by stress (Lüders-like deformation); Stage III – stress induced re-orientation of martensite; Stage IV – plastic deformation of re-oriented martensite and generation of irrecoverable slip.

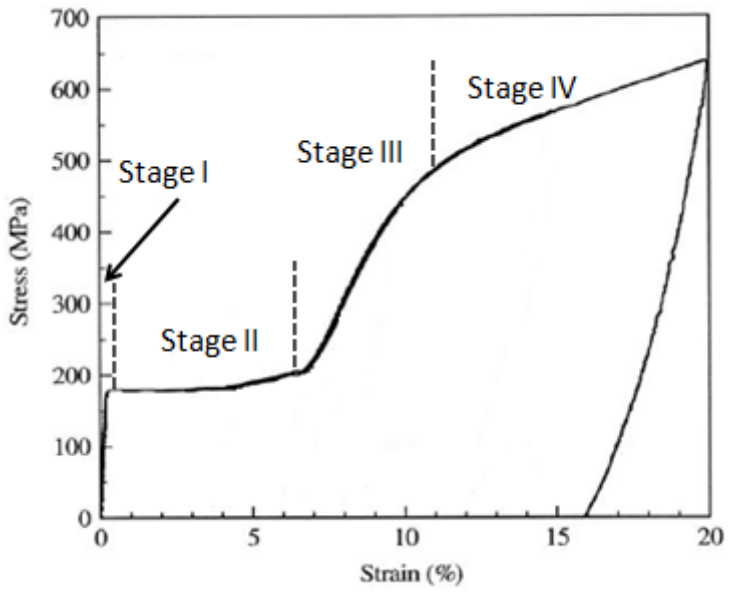

Figure 10 – Typical stress-strain curve for a fully austenitic NiTi SMA. [7]

Note that the stress-strain curve for a fully martensitic NiTi SMA (Figure 11) despite their similarities have some features that are very distinguishing. The main differences are that the plateau in the fully martensitic NiTi is reached for a minor stress level when comparing with fully austenitic NiTi, also the maximum strain achieved is lower for fully martensitic NiTi than for fully austenitic NiTi.

In the typical stress-strain curve for a fully martensitic there are also four stages: Stage I – ideal linear behavior of martensite where the twin boundaries remain stationary; Stage II – corresponds to the re-orientation of the variants due to detwinning associated with coalescence of some variants due to the movement between the ground boundaries. This self-propagating effect is known as “domino detwinning”; Stage III – second stage of linear behavior which is associated with detwinning assisted by deformation with elimination of the twin boundaries; Stage IV – is related with an irreversible deformation due to dislocations slip in the fully detwinned martensite. [7]

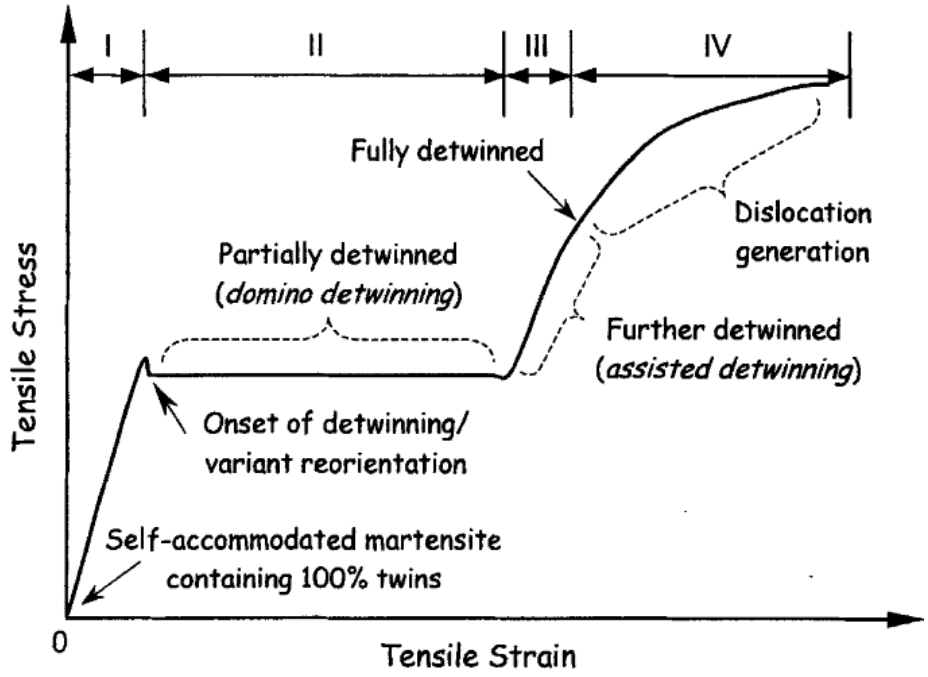

Figure 11 – Typical stress-strain curve for a fully martensitic NiTi SMA. [7]

Figure 12 shows the difference between the deformation mechanisms of stainless steel, which can accommodate higher stress by irrecoverable slip, and a superelastic NiTi alloy, which can accommodate higher deformation due to a reversible process by shifting to twinned martensite.

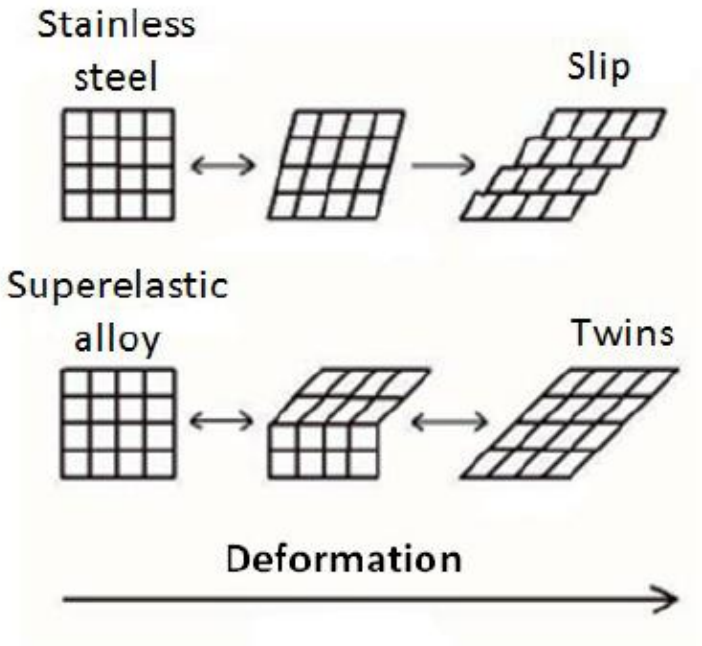

Figure 12 – Schematic representation of lattice changes in stainless steel and in a superelastic alloy. [8]

In literature there is some confusion over the terms pseudoelasticity (PE), SE and rubber-like behavior. In fact sometimes the terms PE and SE are used with the same meaning. When an apparent plastic deformation recovers just by unloading at a constant temperature (the Stress-

Strain curve is characterized by a closed loop), it is called PE, apart from its origin. PE is a generic term which encompasses both superelastic and rubber-like behavior. When a closed loop originates from a stress-induced transformation upon loading and the reverse transformation upon unloading, it is called SE. The rubber-like behavior occurs by the reversible movement of twin boundaries in the martensitic state. However, this singular behavior does not appear in Ni-Ti alloys. [9]

1.1.3.2 - Shape Memory Effect

SME was already introduced before. Here we present a more comprehensive explanation for this mechanical feature.

SME is a phenomenon such that even though specimen is deformed below A_s it regains its original shape by heating up to a temperature above A_f which leads to a reverse transformation. The deformation imposed to the specimen could be of any kind such as tension, compression or bending, as long as the strain is lower than some critical value. SME occurs when specimens are deformed below M_f or at a temperature between M_f and A_s, above which martensite becomes unstable. [9]

If we cool the sample to a temperature below M_f the martensite is formed in a self-accommodating manner. In this process the shape of the specimen does not change due to the self-accommodated transformation. By applying an external force, the twin boundaries move in order to accommodate the applied stress. If the stress is high enough, one single martensite variant will be favored and shape of the specimens is altered. By heating up the sample above A_f , the reverse transformation occurs, and, if this reverse transformation is crystallographically reversible, the original shape is regained. Note that for SME to exist, it is necessary to fulfill two conditions: the deformation proceeds solely by the movement of twin boundaries and the transformation is crystallographically reversible. If either one of these conditions is broken, complete SME is not observed.

Figure 13 shows the microstructural changes that occur in NiTi martensite under stress and which are the basis for the SME. In stage a), we have twinned martensite; in stage b) with the increase of the applied stress, martensite starts to be detwinned; in stage c), continuing to increase the stress, martensite stays fully detwinned; finally, if stage d) is reached, there is no possible way to recover the initial shape of the specimen, since the deformation induced is permanent, due to dislocation slip. When stage c) is finished, it is possible to recover the initial shape of the specimens just by heating up to A_f, having this way the SME.

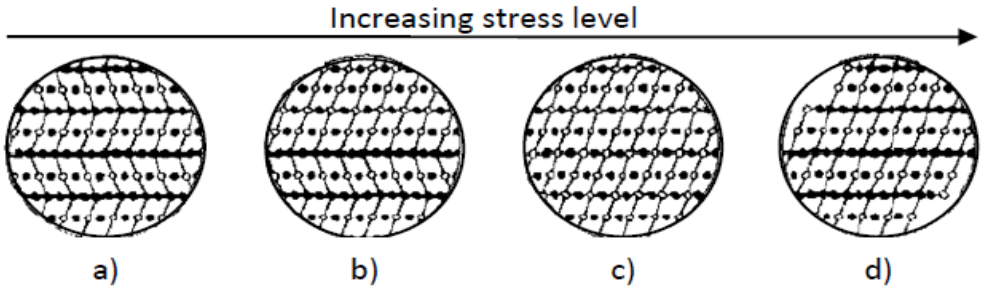

Figure 13 – Microstructural alteration occurred in martensitic NiTi: a) twinned martensite, b) partially twinned martensite, c) detwinned martensite, d) slipped martensite. [5]

If the specimen is deformed in a range of temperatures between M_f and A_s SIM also contributed to the deformation, in addition to the above process of variant coalescence.

1.1.1.3 - Existence of Superelasticity and Shape Memory Effect

Despite the fact that SE and SME were discussed separately, they are closely related. Figure 14 shows the relationship between these two features. It is expectable that both SE and SME are observable in the same specimen, depending upon the test temperature and as long as the critical stress for slip is high enough.

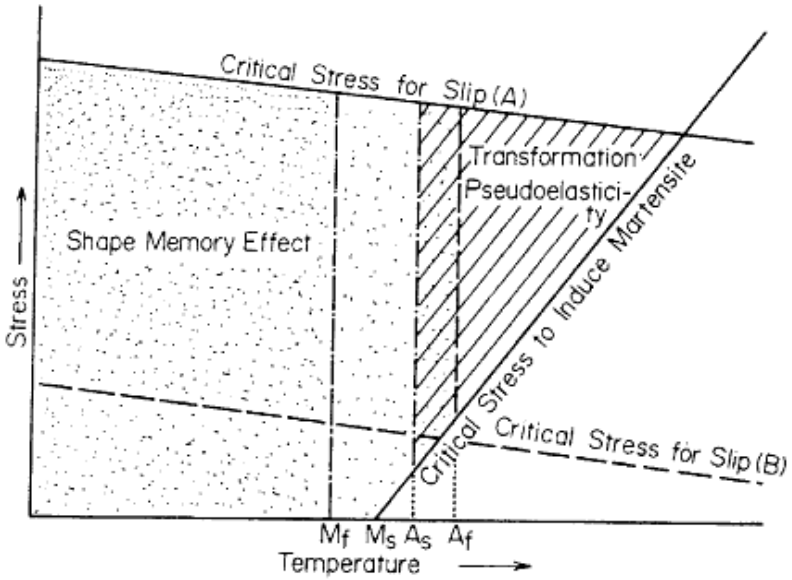

Figure 14 – Schematic diagram representing the region of shape memory effect and superelasticity in temperature-stress coordinates; (A) represents the critical stress for the case of high critical stress and (B) represents the critical stress for low critical stress. [3]

SE occurs above A_f where martensite is completely unstable in the absence of stress. SME occurs below M_f followed by heating up to A_f. Between A_s and A_f both occur partially. The straight line with positive slope represents the variation with temperature of the critical stress to induce martensite, following the Clausius-Clapeyron relationship ($d\sigma/dT = -\Delta S/\varepsilon$). With the increase of temperature, a higher stress is required to induce martensite. The straight lines with negative slopes (A and B) represent the critical stress for dislocation slip. It is possible to manipulate the straight line A just by a softening effect in the material, which will lead to a drop of the line. On the other hand, due to a hardening effect, the same line could raise and with that it is possible to manipulate a certain window for some mechanical feature, such as SE or SME. Since dislocation slip never recovers upon heating or unloading, the applied stress must be between the lines in order to realize SE or SME. SE will not occur if the critical stress for dislocation slip is as low as the line B, since slip occurs prior to the onset of SIM.

1.2 - Laser welding

1.2.1 - Basic Laser Fundamentals

Laser, an acronym for Light Amplification by Stimulated Emission of Radiation, is essentially a coherent, convergent and monochromatic beam of electromagnetic radiation with a wavelength ranging from ultra-violet to infrared. Laser can deliver very low (≈ mW) to extremely high (1-100 kW) focused power with a precise spot size/dimension and

interaction/pulse time (10^{-3} to 10^{-15} s) on to any kind of substrate trough any medium. [10] Laser can be employed in many different fields such as metrology, reprography, military, medical, etc.

In laser welding the high power density used for materials joining leads to a formation of a hole due to evaporation. The hole formed is transverse through the material, with the molten walls sealing up behind it. This is known as the "keyhole" weld, which is normally characterized by its parallel sided fusion zone and narrow width. Figure 15, shows different fusion zone profiles for different welding processes.

Process	Heat source intensity ($W\,m^{-2}$)	Fusion zone profile
Flux-shielded arc welding	5×10^6–10^8	
Gas-shielded arc welding	5×10^6–10^8	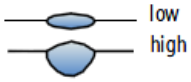
Plasma	5×10^6–10^{10}	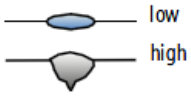
Laser or electron beam	10^{10}–10^{12}	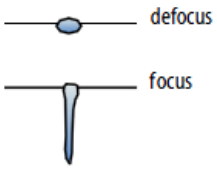

Figure 15 – Different fusion zone profiles for different laser welding techniques. [10]

Since the weld is rarely wide compared with the penetration, it can be seen that the energy employed in the process is being used for melting the interface to be joined and not most of the surrounding area as well. A term that define the concept of efficiency is known as "joining efficiency", which is defined as vt/P, where v is the travel speed (mm s^{-1}), t is the thickness of the sample to be welded (mm) and P is the incident power (kW). The higher the value of joining efficiency the less energy is spent in unnecessary heating, which can lead to the existence of a wider heat affected zone (HAZ) or to distortion.

Besides the keyhole welding there is also another possible mode of welding in laser welding: conduction-mode or conduction-limited welding. As stated before in keyhole welding there is sufficient energy per unit length to cause evaporation and hence a hole in the melt pool. The hole created is stabilized by the pressure from the vapor being generated. The keyhole behaves like an optical black body in that radiation enters in the hole being subjected to multiple reflections before being able to escape (see Figure 16, left side). Conduction-mode welding occurs when the power density at a given welding speed is insufficient to cause boiling and therefore to generate a keyhole. The weld pool has strong stirring forces driven by Marangoni-type forces from the variation in surface tension with temperature. The Marangoni force is related to surface-tension-temperature-gradient-driven fluid flow, where flow at the weld pool surface progresses from regions of low surface tension to regions of high surface tension. [11] In the conduction-mode welding since the heat transfer is controlled by

conduction the fusion zone (FZ) and the HAZ will be larger than in the keyhole mechanism (see Figure 16 to compare the effect of both mechanisms).

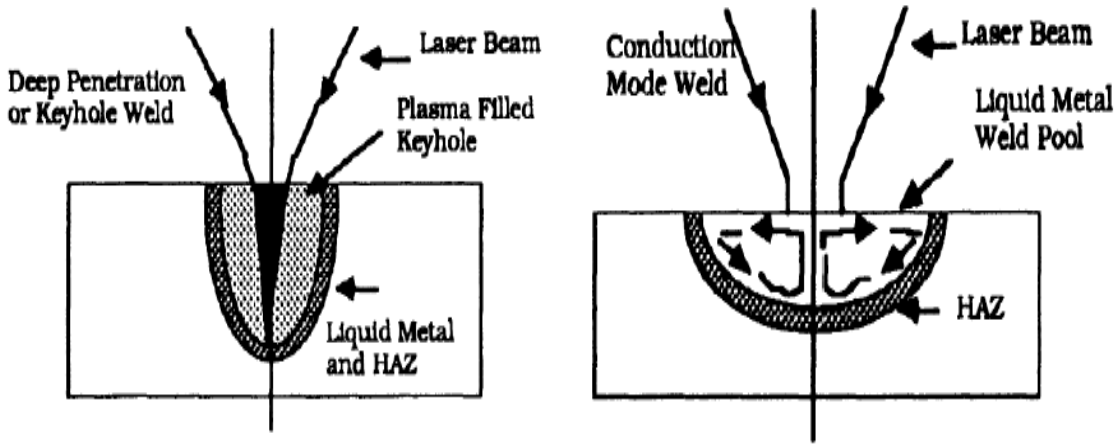

Figure 16 – Keyhole welding (on the left) and conduction-mode welding (on the right). [10]

It must be noticed that laser welding has many process parameters that need to be controlled in order to attain a good weld (Figure 17). Those process parameters are: beam properties such as power, pulsed or continuous laser, spot size and mode, wavelength; transport properties such as speed, focal position, joint geometries, gap tolerance; shroud gas properties such as composition and pressure; material properties such has composition and surface conditions.

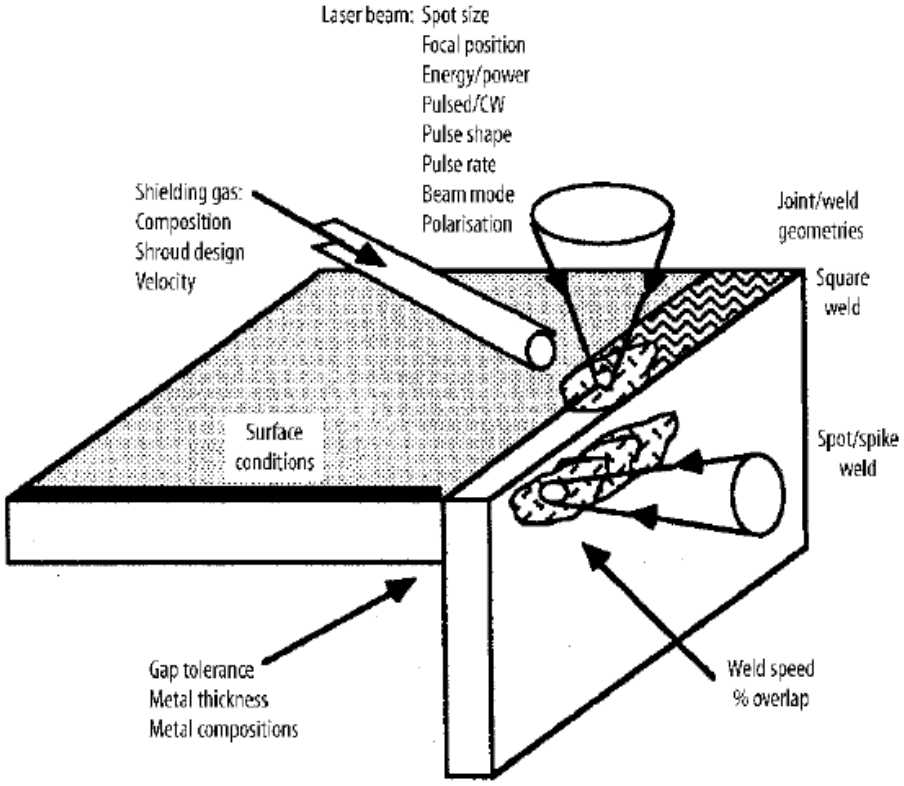

Figure 17 – Main process parameters to be controlled in laser welding. [10]

As depicted in Figure 18 metallic materials tend to absorb laser radiation, especially at wavelengths below 1 µm. Recent develops in laser industry has been the production of lasers with high power, low wavelength and good beam quality.

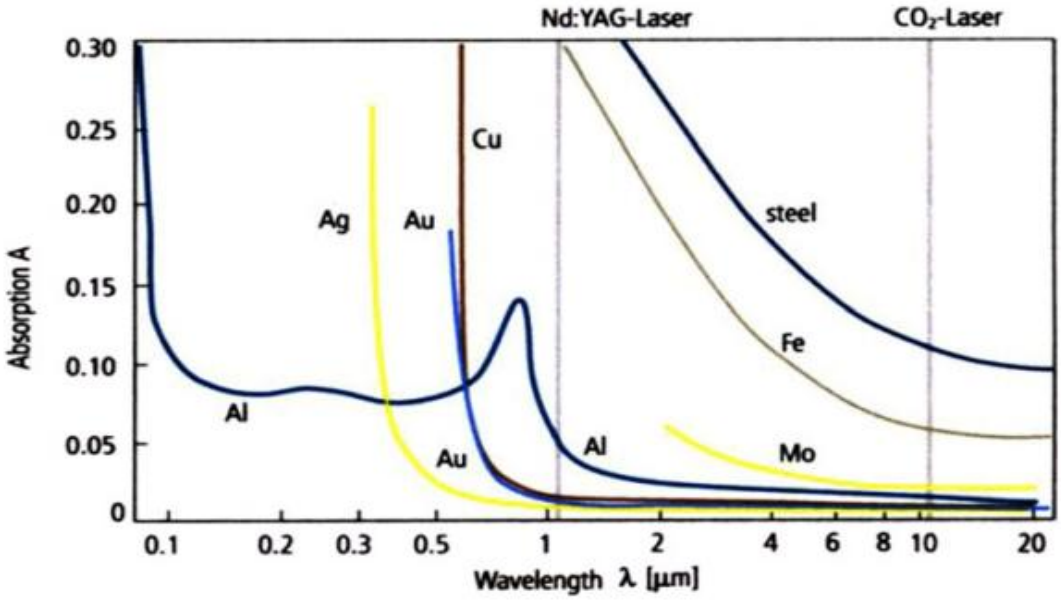

Figure 18 – Absorption of a number of metals as a function of laser radiation wavelength. [12]

Laser welding has some particular characteristics which are distinct from other welding processes. These characteristics are: high energy density, with a "keyhole" type weld, which causes less distortion; high processing speed and rapid start/stop; welds at atmospheric pressure; no filler required; narrow weld and relatively little HAZ, which means that laser welding can be used in near heat-sensitive materials; very accurate welding is possible; little or no contamination since protection gases can be used; relatively little evaporation loss of volatile components, which makes this technique very suitable for certain alloys such as Mg or Li alloys); relatively easy to automate the process. However some materials can be very difficult to join by this technique. For instance materials with high reflectivity (such as aluminum) can be difficult to join. Other disadvantages are the initial high cost of the equipment and the high cost with protection gases such as helium (He) or argon (Ar).

1.2.2 - Laser welding of NiTi

Due to the poor workability of NiTi alloys, suitable welding techniques must be used to obtain devices and components with different geometries. However the mechanical and functional behavior of these alloys is strongly influenced by possible thermal effects and modifications of the chemical composition associated with the welding process chosen. [13] There are not many joining techniques suitable for this class of materials. Among these techniques we have friction welding, resistance welding and tungsten inert gas (TIG). Laser welding is one of the most important joining techniques available for this class of materials. In particular the Nd:YAG laser, which was used to perform the similar NiTi joints, is suitable for welding low thickness components due to its high precision and reduced HAZ. [14]

Most of the work on laser welded NiTi presented in literature until now is based in NiTi wires [15], [16], [17] or in NiTi thin foils [18], [19]. Laser welding of NiTi sheets (with more than 0.5

mm thickness) [14], [20] is not as reported as the previous mentioned. Despite all the work done in similar welding of similar NiTi joints the effect in terms of the mechanical properties, chemical composition and therefore the phases present in the different parts of the welded specimens is not clear yet. In particular, the comprehension of the effect of long cycling in these materials is very important, in order to use this joining process with high reproducibility in NiTi SMA for several applications. Some cycling experiments regarding laser welded NiTi similar joints are presented in the literature, however these kind of experiments are characterized by a relatively low number of cycles (usually up to 20 cycles) and by low strain (up to 4%) achievements during the mechanical tests. One example of a cycling test with a slightly increase of the number of cycles (up to 30) and of the strain (up to 6%) was recently presented by Vieira *et al*. [21]

After welding the modifications introduced due to the laser processing tend to affect certain features over others. For instance, welded specimens tend to present lower ultimate tensile strength (UTS) and elongation to fracture. SME may prevail depending if the strain applied is not enough to induce an irreversible deformation of martensite. SE may have a greater or less extension depending on the chemical alterations that the FZ and the HAZ has suffered during the laser welding.

During welding, as mentioned before, the interaction of the laser beam with the material causes a localized fusion and in the neighboring regions there is a temperature increase without change of state.

In the FZ, if there is a preferential evaporation of one of the elements it may give rise to chemical composition changes. For the Ni-Ti system, it is expected that Ni has a higher evaporation rate than Ti (Figure 19). [22] Despite the existence of a shielding gas, these phenomena may still occur.

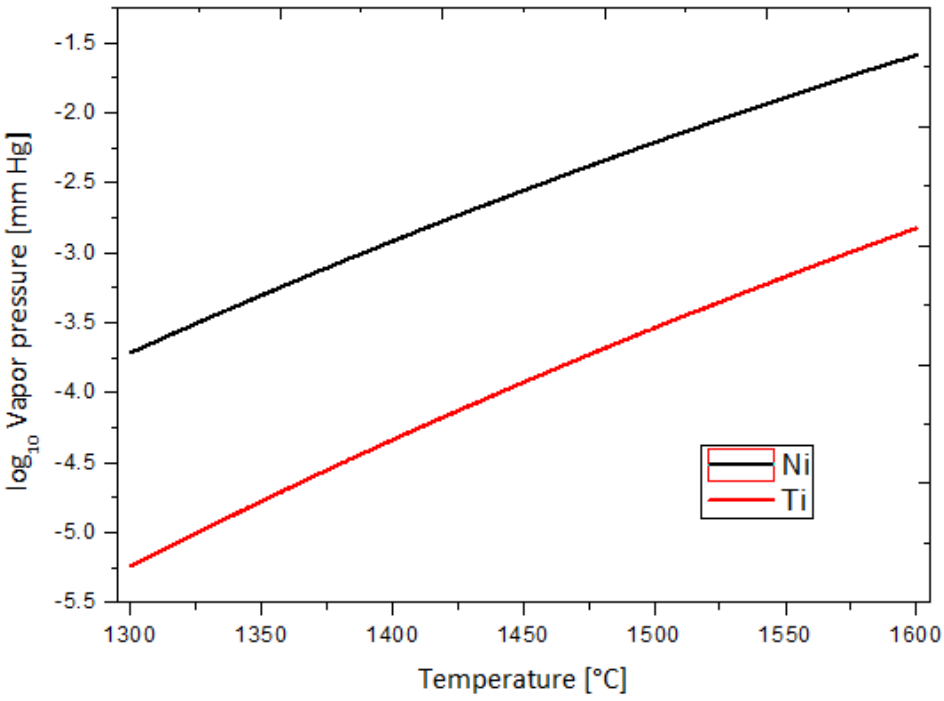

Figure 19 – Vapor pressure as a function of temperature for Ni and Ti.

In the HAZ, if the temperature is high enough, full solution may occur and, depending on the cooling rate, precipitation phenomena may take place, or not. This precipitation will lead to a chemical composition change in the surrounding matrix.

It is possible that the chemical compositions changes that may occur in the FZ and in the HAZ, as mentioned above, may alter the transformation temperatures of the welded samples.

1.3 - Justification of the Work Developed

The work developed during this Master Thesis is the continuation of the work developed by Vieira. [23] On that work similar and dissimilar butt joints using NiTi were laser welded and studied in order to access how laser welding influences the mechanical and microstructural characteristics of the welds. It was used a laser power source operating in continuous mode.

For this reason some of the methods and experimental results attained by Vieira will be presented in order to justify the work done during this Master Thesis.

For this work, as stated previously, the objective is to have a better understanding on how the microstructural features presented by the laser welded NiTi joints influence its mechanical behavior to cyclic loading/unloading, and correlate that influence with the process parameters chosen for the welding procedure.

2 - Materials and Methods

2.1 - Materials

Similar NiTi/NiTi butt weld joints were joined using superelastic NiTi alloy (50.8 at% Ni) plates with 1.0 ± 0.1 and 0.50 ± 0.05 mm thicknesses from *Memory-Metalle GmbH* Alloy S (superelastic standard alloy). The alloys had an A_f temperature of about 0 °C (according to the manufacturer), were flat annealed and surface oxide free. The flat annealing gave to the samples its shape in the austenitic state.

Physical and mechanical properties of NiTi SMA are presented in Tables 1 and 2.

Table 1 – Physical properties of NiTi SMA [24]

Physical properties of NiTi SMA						
Melting point	**Density**	**Specific heat**	**Coefficient of thermal expansion**		**Thermal conductivity**	
			Martensite	Austenite	Martensite	Austenite
[°C]	[kg/dm^3]	[J/kg.K]	[x10^{-6} K^{-1}]		[W/m.K]	
1300	6.45	322	6.6	11	8.6	18

Table 2 - Mechanical properties of NiTi SMA [24]

Mechanical Properties of NiTi SMA						
Young modulus		**UTS**		**Elongation**		**Poisson ration**
Martensite	Austenite	Cold worked	Fully annealed	Cold worked	Fully annealed	
[GPa]	[GPa]	[MPa]	[MPa]	[%]	[%]	-
70-83	28-41	1900	895	5-10	25-50	0.33

2.2 - Welding Process

Similar NiTi/NiTi butt welds were produced using a Nd:YAG diode-pumped laser from Rofin-Sinar, model DY 033, in continuous wave mode available at *Universidad Politecnica de Madrid* premises. An *ABB* robot remotely controlled the laser head movement. The main characteristics of the laser equipment are displayed in Table 3.

All the laser welded joints were prepared and are described in the Master Thesis of L. Alberty Vieira. [23]

Table 3 – Technical data of DY 033 Rofin Sinar Nd:YAG laser [23]

DY 033 *Rofin-Sinar* Nd:YAG technical data	
Wavelength	1064 nm
Maximum output power	3300 W
Number of cavities	6
Fiber diameter	400 µm
Optical arrangement	
Title angle	3°
Focal length	160 nm
Beam diameter	0.45
Intensity distribution	Gaussian

Plates of 35x35x1.0 and 35x35x0.5 mm were butt joined. Fixing and alignment of 1.0 and 0.5 mm thick plates were achieved using a positioning system specially designed for this purpose. The system assures that opposite plates were in the same plane and tight to each other, due to small compressive force applied by the mechanism. He and Ar were used to create an inert atmosphere. Welding direction was perpendicular to the rolling direction.

Welding parameters of 1.0 and 0.5 mm butt joints are presented in Tables 4 and 5. [23]

Table 4 – Welding parameters for 1.0 mm butt joints [23]

Welding parameters for 1.0 mm thick plates								
Sample reference	**Power**	**Welding speed**	**Heat input**	**FPP**	**Focused beam Ø**	**Argon**		**Helium**
						Air knife	Laterally	Back
	[W]	[mm/s]	[J/cm]	[mm]	[mm]	[bar]	[l/min]	[l/min]
A-A	990	25	396	0	0.45	7.5	40	50
B-B	990	20	495	0	0.45	7.5	40	50
C-C	990	15	660	0	0.45	7.5	40	50
D-D	1485	30	495	0	0.45	7.5	40	50
E-E	1485	25	594	0	0.45	7.5	40	50
F-F	1485	20	743	0	0.45	7.5	40	50
H-H	1980	40	495	0	0.45	7.5	40	50

Table 5 – Welding parameters for 0.5 mm butt joints [23]

Welding parameters for 0.5 mm thick plates								
Sample reference	**Power**	**Welding speed**	**Heat input**	**FPP**	**Focused beam Ø**	**Argon**		**Helium**
						Air knife	Laterally	Back
	[W]	[mm/s]	[J/cm]	[mm]	[mm]	[bar]	[l/min]	[l/min]
F-F	726	30	242	0	0.45	7.5	40	50
K-K	790	50	158	0	0.45	7.5	40	50
O-O	858	70	122	0	0.45	7.5	40	50

After welding specimens were cut using a precision cut-off machine *ATM GmbH model Brillant 211* equipped with a diamond wheel type *B102* from the same maker. Cutting parameters were the following: speed - 4000 rpm; feed rate - 1 mm/min; lubricant - multipurpose cutting fluid.

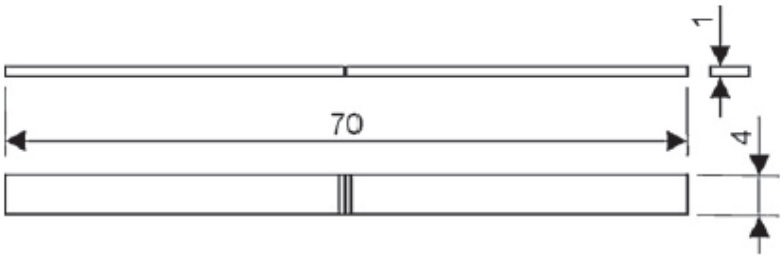

Figure 20 – Welded specimens attained after cutting.

2.3 – Characterization Techniques

2.3.1 - Differential Scanning Calorimetry

Differential scanning calorimetry (DSC) is a thermoanalytical technique in which the difference in the amount of heat required to increase the temperature of a sample and reference is measured as a function of temperature. The sample to be analyzed and the reference are both kept at a same temperature during the experiment. [25]

A *DSC 204 F1 Phoenix* model from *Netzsch* was used in order to perform high and low temperature structural tests, using liquid nitrogen on low-temperature tests. DSC was used in order to characterize the base material (BM) in terms of zero-stress structural transformation temperatures. Liquid nitrogen was used to cool down the system to about -160 °C. Upon heating the maximum temperature was of about 70 °C. The cooling and heating rate was of 10 °C/min.

2.3.2 - Mechanical Tests

2.3.2.1 - Uniaxial Static Tensile Tests

Uniaxial tensile tests were performed on the samples welded by Vieira. [23] These tests were performed at room temperature, at CENIMAT, on an *AUTOGRAPH SHIMADZU* model AG500Kng equipped with a *SHIMADZU* load cell type SFL-50kN AG with a total capacity of 50 kN. UTS and elongation to fracture were recorded.

2.3.2.2 - Cycling Tests

Considering UTS and elongation to fracture of welded samples presented in Tables 7 and 8 an alternated cycling routine with a total of 5 sets of cyclic tests was developed. The 5 sets of cyclic tests chosen are presented in Table 6. The equipment used is mentioned just above.

Table 6 – Alternated cycling routine for the welded samples

Set of cyclic test	Maximum strain	Cycles
1	10	60
2	8	60
3	10	60
4	8	60
5	10	360
Number of total cycles if the sample did not break : 600		

Sample K-K due to its mechanical properties (see Table 8) in stages 1, 3 and 5 was strained up to 9% instead of 10%.

If the sample tested would stand for the entire cycling routine it would stand to a total of 600 cycles. This kind of test, with the samples being subjected to very high strains during a large number of cycles, was not been reported in the literature yet.

From the cycling tests it was possible to analyze how the accumulated irrecoverable strain evolved with the increase of the number of cycles completed.

2.3.3 - Shape Memory Effect Evaluation

The experimental method for evaluating the SME of the welded joints is based on bending and free-recovery testing, following previous work developed by Vieira [23], tests were performed by bending the sample in the martensitic condition followed by the removal of the load and heating up to the parent phase.

These tests were conducted using liquid nitrogen and a dedicated device manufactured in house (see Figure 21).

Figure 21 – Device used for testing the shape memory effect.

Tests were performed as shown in Figure 22. Note that the bending is performed when the sample is dipped in the liquid nitrogen and the recovery took place at room temperature. The results are expressed in terms of the Ω angle, which represents the permanent deformation angle. For example, if Ω = 0 it means that the sample recovered to its initial shape.

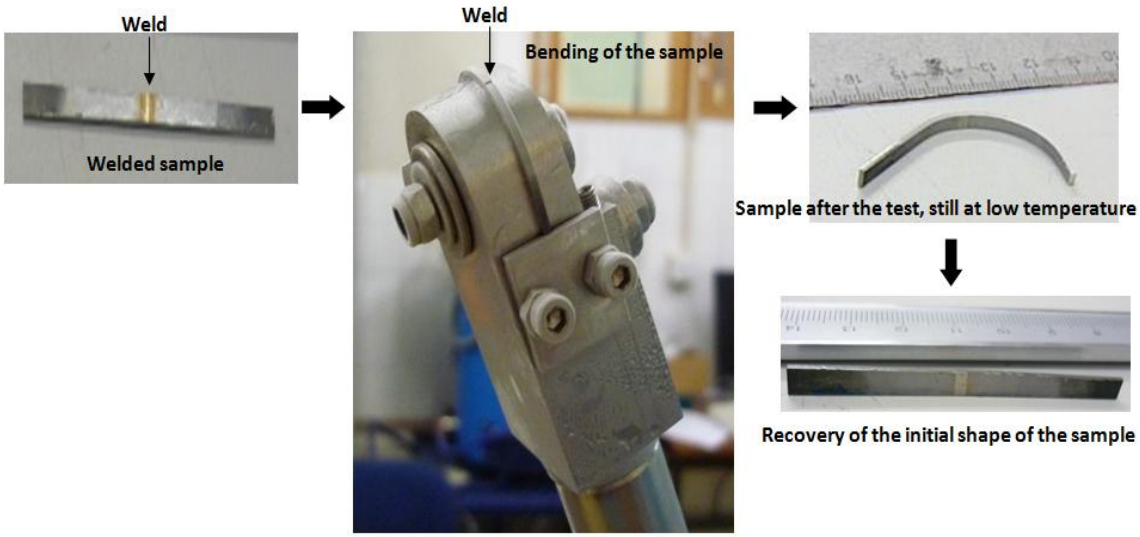

Figure 22 – Bending and free-recovery method used to analyze the shape memory effect of the welded samples.

SME was evaluated in a total of 12 specimens. Two sample of the base material were used in order to investigate if the rolling direction rolling direction of the base material could affect the shape memory effect, so it was used one sample cut perpendicular to the rolling direction (sample “MB1”) and other sample cut parallel to the rolling direction (sample “MB2”). To

investigate the influence of the angle between the rolling direction and the welding direction on the SME, it was used one sample with the rolling direction perpendicular to the welding direction (sample “Perpendicular”) and another one with both directions parallel to each other (sample “Parallel”). These samples were welded in the same conditions. Finally SME was evaluated in two samples with different thicknesses (0.5 and 1.0 mm, respectively samples K-K and F-F). All samples were tested four times, and the samples were positioned so that the face and the root of the weld bead were alternately submitted to tensile and compressive forces.

In order to assess if after the cycling tests the strain presented by the samples could be recovered, a different procedure was carried out. Samples B-B, C-C, F-F and K-K cycled 600 cycles, were dipped in the liquid nitrogen, bent and heated up above room temperature. Samples D-D and E-E were first heated up to around 70 °C and then were dipped in the liquid nitrogen, bent and heated up above room temperature. The heating of the samples before the dipping in liquid nitrogen was made to ensure that these samples before dipping had an uniform state (fully austenitic).

The 1.0 mm thick samples were subjected to a strain of 3.77% while 0.5 mm thick sample were subjected to 1.94% during SME evaluation.

2.3.4 - X-ray Diffraction Analysis

2.3.4.1 - Minor Introduction to X-ray Analysis

XRD is a tool for the investigation of the fine structure of matter. [26] This technique had its beginning in von Laue’s discovery in 1912 that crystals diffract x-rays, the obtained diffraction revealing the structure of the crystal. XRD is widely used for the determination of the crystal structure of materials, residual stresses, size of crystallites and preferential orientation of the grains in the analyzed material.

When a material is bombarded with x-rays of a fixed wavelength (which must be similar to the spacing of the atomic-scale crystal lattice planes) and at a certain incident angles, intense reflected x-rays are produced when the wavelengths of the scattered x-rays interfere constructively. In order for the waves to interfere in a constructive way, the differences in the travel path must be equal to integer multiples of the wavelength. When this phenomenon occurs, a diffracted beam of x-rays will leave the material at an angle equal to that of the incident radiation.

To illustrate this feature, let us consider a crystal with interplanar distances d, where the travel path length difference between the ray paths ABC and A’B’C’ is an integer multiple of the wavelength. Then, constructive interference will occur for a combination of that specific wavelength, crystal lattice planar and angle of incidence (Θ).

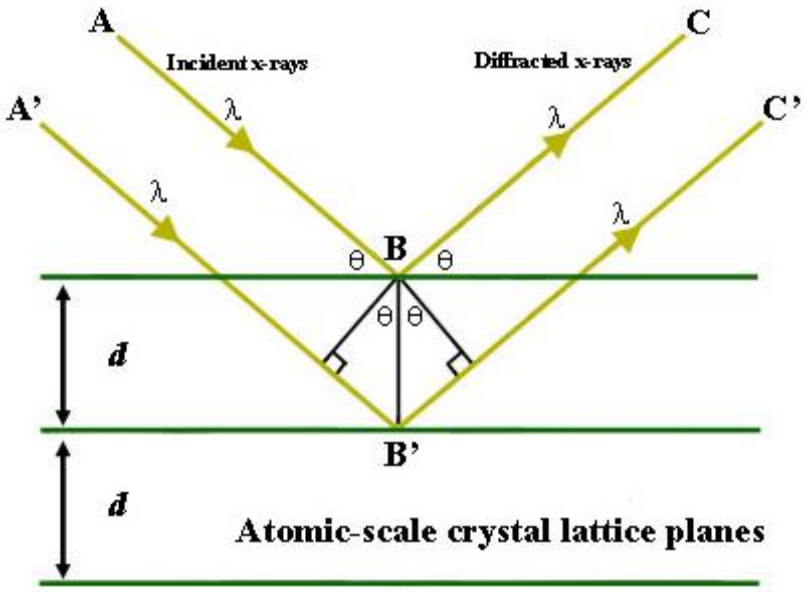

Figure 23 – Schematic representation of the Bragg's law. [27]

The general relationship between the wavelength of the incident x-rays, angle of incidence and spacing between the crystal lattice planes of atoms is known as the Bragg's law (proposed in 1913), which is expressed as: $n\,\lambda = 2\,d\,sin\,(\Theta)$, where n is an integer (the order of the reflection), λ is the wavelength of the incident x-rays, d is the interplanar spacing of the crystal and Θ is the angle of incidence. [26]

2.3.4.2 - Experimental Set-up for the Base Material

XRD analysis of the BM was performed using a Bruker diffractometer (rotating anode – XM18H, Cu-Kα radiation (1.5418 Å), 30 kV/100 mA, D5000 goniometer and TTK-450 chamber from Anton Paar) with conventional θ/2θ scanning at various temperatures from 120 to -180 °C.

2.3.4.3 - Experimental Set-up for the Welded Samples

XRD analysis was performed at DESY facilities (HEMS - High Energy Materials Science beamline) at PETRA III in Hamburg, Germany. It was used a wavelength of 0.1426 Å (87 keV). A 2D detector was used and the tests were held at room temperature (21 °C). Figure 24 presents the scheme used for the XRD measurements. The welding line (A) was kept horizontal by coinciding with the horizontal hairline of the theodolite. Laser was kept in the path for the X-ray which allowed foreseeing where on the sample the X-ray beam will hit. By moving the vertical motion motors remotely from the control room alignment is performed by illuminating the welding line in the specimen, with the laser beam. Scans are recorded successively from approximately 3 mm below (C) the welding line to approximately 3 mm above (B), in steps of 0.2 mm. The beam spot was of 0.1x0.1 mm. The exposure time was kept from 5 to 10 seconds.

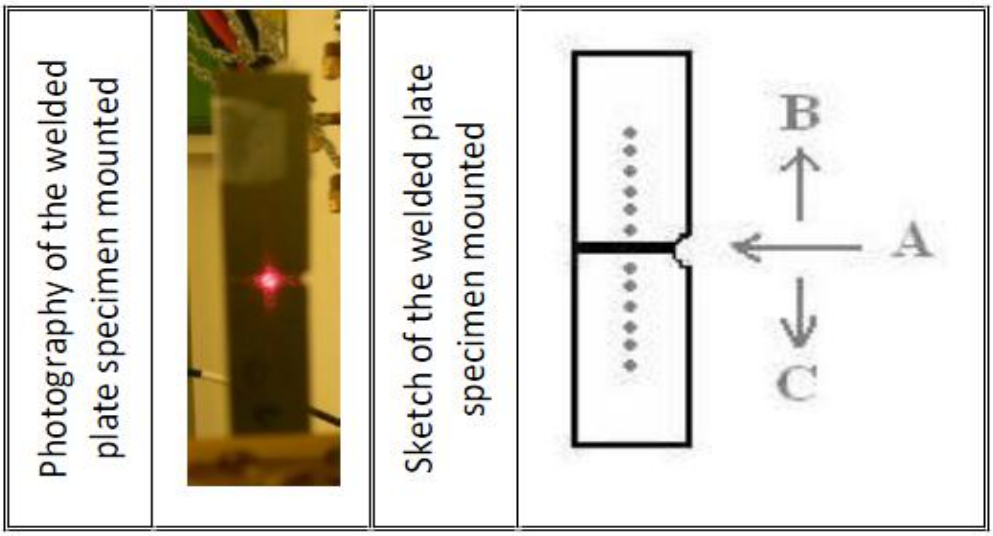

Figure 24 – Scheme used for the XRD measurements.

The data acquired was treated with the software Fit2D [28], obtaining XRD patterns from the Debye-Scherrer rings. The Debye-Scherrer rings are two-dimensional patterns consisting in concentric rings produced by the superposition of reflections of various crystals where the x-ray beam is focused and that are oriented according to a (hkl) plane fulfilling the diffraction condition of Bragg. [26] Figure 26 is a schematic representation of the attainment of Debye-Scherrer rings.

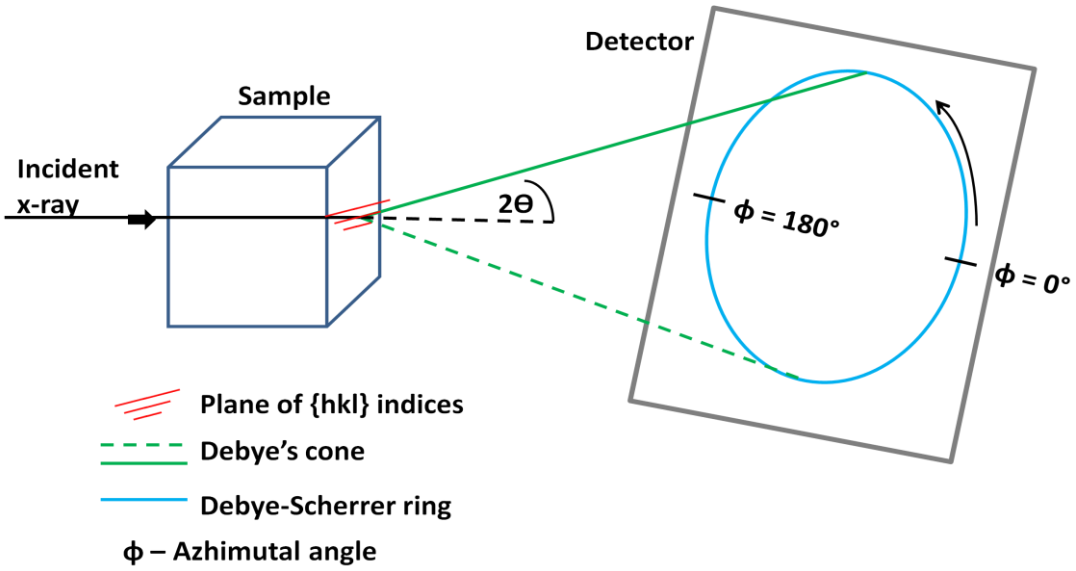

Figure 25 – Schematic representation of the mode of obtaining the Debye-Scherrer rings.

For a complete randomness of orientations every crystallographic plane of that family make the same diffraction angle relatively to the incident beam, which leads to the formation of a diffracted beam with conic symmetry. The intersection of the cones with a plane perpendicular to the cones axis gives the Debye-Scherrer rings.

Also, it was possible to obtain the XRD patterns of the welded sample where each spectra is the result of the integration from 0 to 360° (for Phi) made using Fit2D.

XRD technique was chosen to analyze the welded samples since the welding process can cause alteration in the phases present in the material. In particular, the welding procedure may alter the existing phases in the HAZ and in the FZ when comparing with the BM.

All welded samples were analyzed. In addition, two extra samples were studied, to examine the effect of the mechanical cycling on the microstruture: sample B-B after 4 and 600 cycles.

2.3.5 - Scanning Electron Microscopy

Scanning electron microscopy (SEM) was used in order to analyze the fracture mechanism of the similar welding of NiTi. For this purpose, it was used *ZEISS DSM 962 ESM*, belonging to Cenimat. The samples analyzed were coated with carbon.

3 - Experimental Results

This chapter aims to present the experimental results. For this, a brief description of the mechanical properties of the laser welded specimens [23] that constituted the basis for the cycling tests performed is presented.

Regarding the work developed during this Master Thesis, the results are organized in the following sequence:

- DSC analysis from the as-received plates which allow determining the transformation temperature ranges of the BM.
- XRD measurements that allow the structural characterization of BM at different temperatures. Also, XRD patterns of the welded samples to characterize the weld bead and its neighboring regions, identifying, at room temperature, the different phases in each zone of the welded samples (namely in the HAZ, FZ and BM), with a fine spatial resolution, will be presented. From this XRD data, it is also possible to identify different microstructural features, such as preferential orientation or existence of fine or coarse grain.
- Mechanical tests from cyclic load/unload of the welded samples and a summary of the evolution of the accumulated irrecoverable strain with the number of cycles.
- Tests to assess the influence of the welding parameters on the SME in the welded joints.
- SEM analysis of samples A-A and C-C, to understand the fracture mechanism of the welded joints that suffered premature rupture.

When justified, a short summary of the results in appropriated Tables is given in order to facilitate the interpretation of the experimental results in the discussion chapter.

3.1 - Mechanical Properties of the Welded Samples

The strength and ductility parameters from tensile tests results for 1.0 and 0.5 mm thick samples [23] are presented in Tables 7 and 8, respectively.

Table 7 – Strength and ductility parameters from tensile test results of 1.0 mm thick samples [23]

Strength and ductility parameters from tensile test results of 1.0 mm thick samples		
Sample reference	**UTS [MPa]**	**Elongation to fracture [%]**
A-A	637	12.1
B-B	511	10.6
C-C	530	11.1
D-D	482	10.1
E-E	337	6.5
F-F	522	11.3
G-G	439	10.4
H-H	501	11.5
I-I	394	10.3

Table 8 – Strength and ductility parameters from tensile test results of 0.5 mm thick samples [23]

Strength and ductility parameters from tensile test results of 0.5 mm thick samples		
Sample reference	**UTS [MPa]**	**Elongation to fracture [%]**
F-F	585	10.7
K-K	367	8.34
O-O	519	10.2

3.2 - Differential Scanning Calorimetry

The phase transformation temperatures for a zero-stress condition measured by DSC on the BM are depicted in Figure 26, while Table 9 summarizes the transformation temperatures.

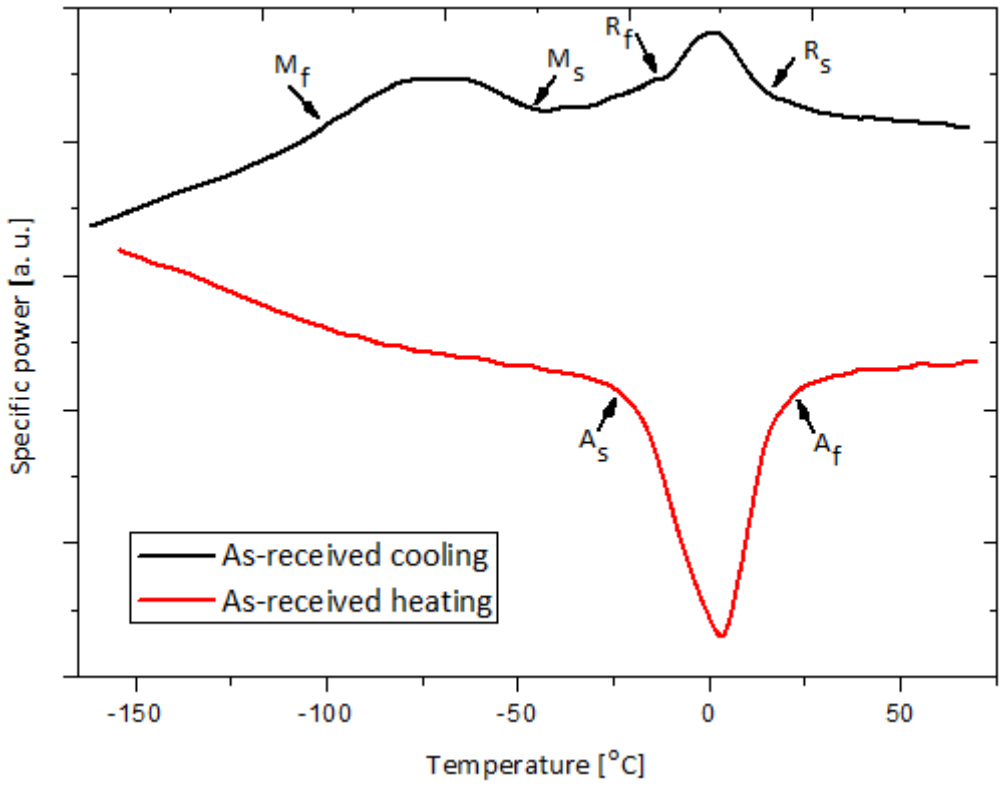

Figure 26 – DSC measurements of the base material for determination of the transformation temperatures

Table 9 – Summary of the transition temperatures of the base material

Transformation temperatures of the BM from DSC analysis						
	M_s [°C]	**M_f [°C]**	**R_s [°C]**	**R_f [°C]**	**A_s [°C]**	**A_f [°C]**
Upon heating	-	-	-	-	-22	24
Upon cooling	-53	-98	15	-12	-	-

DSC results show the existence of a two-step transformation upon cooling, identified by two exothermic peaks, with the transformation sequence from high to low temperature: austenite to R-phase and from R-phase to martensite. Upon heating, only one endothermic peak is observed.

3.3 - X-ray Diffraction Analysis

3.3.1 - Analysis of the Base Material subjected to Thermal Cycling

Figures 27 depicts the XRD analysis of the BM from 120 to -180 °C, and Figure 28 shows the contour lines of Figure 27.

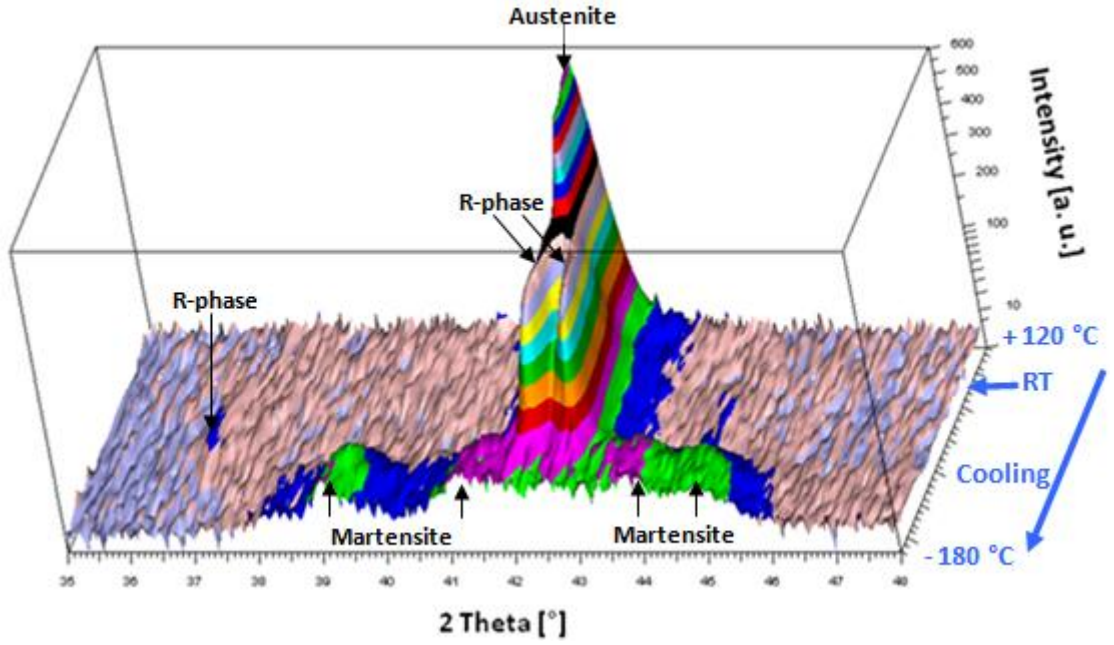

Figure 27 – XRD analysis of the BM from 120 to -180 °C (Cu-Kα radiation, 1.5418 Å).

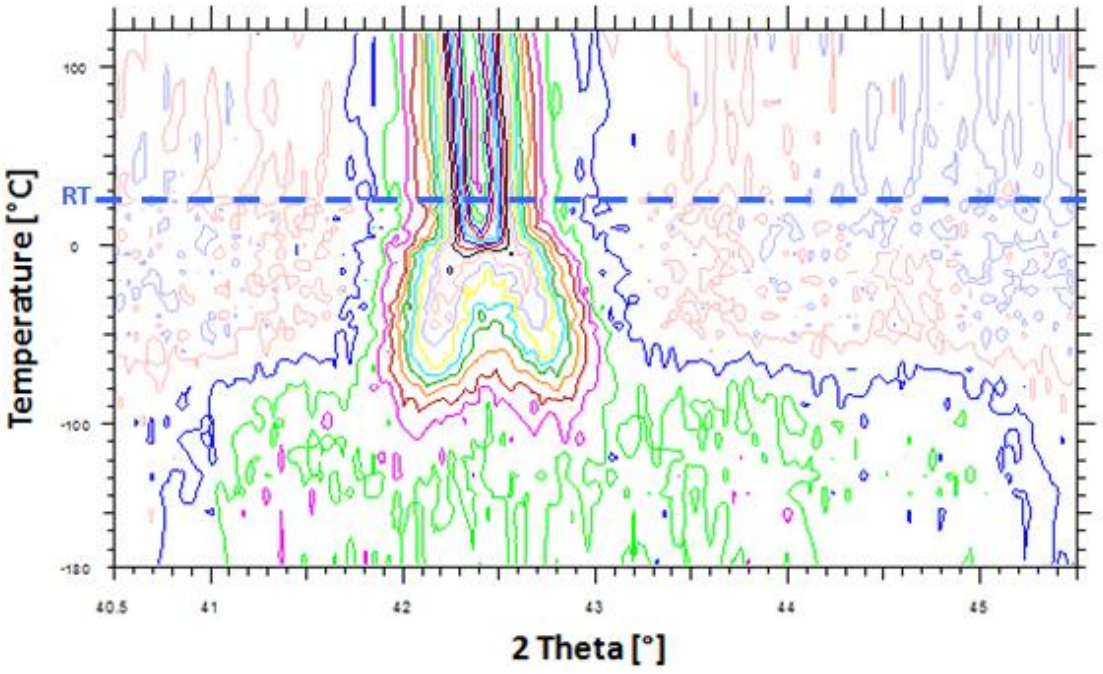

Figure 28 – Contour lines from the XRD analysis of the BM (Cu-Kα radiation, 1.5418 Å).

From Figures 27 and 28 it is possible to verify that close to room temperature (around 25 °C) there is evidence of the existence of R-phase. Martensite only starts to appear around -50°C.

3.3.2 - Analysis of the Welded Samples

3.2.2.1 - 1.0 mm thick samples

The XRD patterns along the samples A-A, B-B, C-C, D-D, E-E, F-F and H-H are depicted in Figures 29 to 37. For sample B-B there is also XRD patterns after 4 and 600 cycles, in order to access the microstructural modifications due to cycling tests. In 3D XRD graphs that will be now presented only austenite peaks are identified (with black arrows corresponding to a specific value of 2Θ), the remaining corresponding to martensite (no R-phase detected).

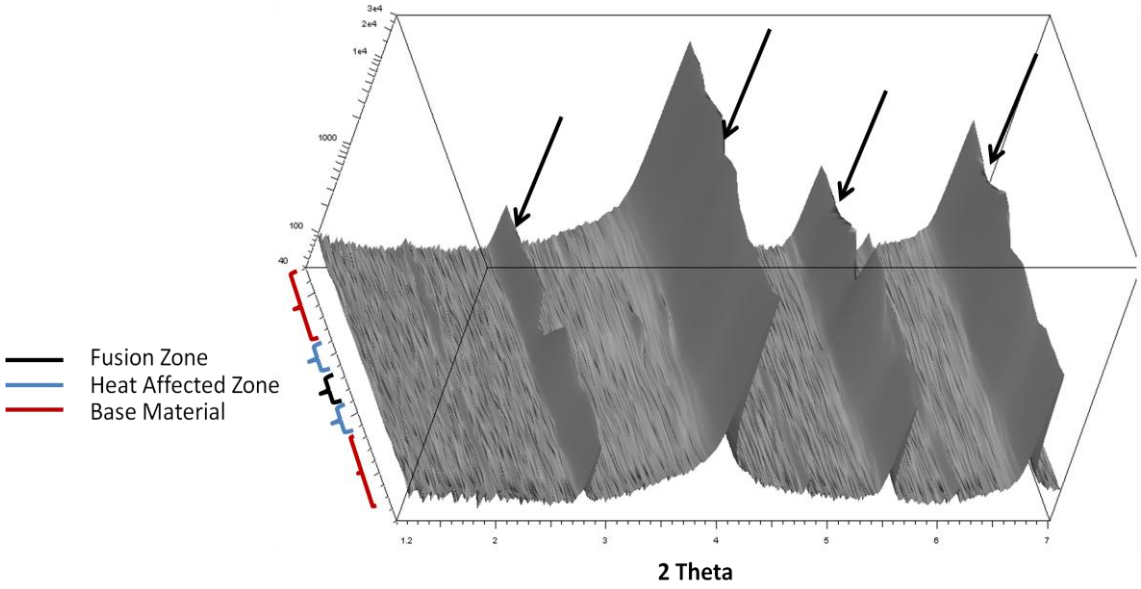

Figure 29 – XRD patterns along sample A-A (synchrotron radiation, 0.1426 Å wavelength).

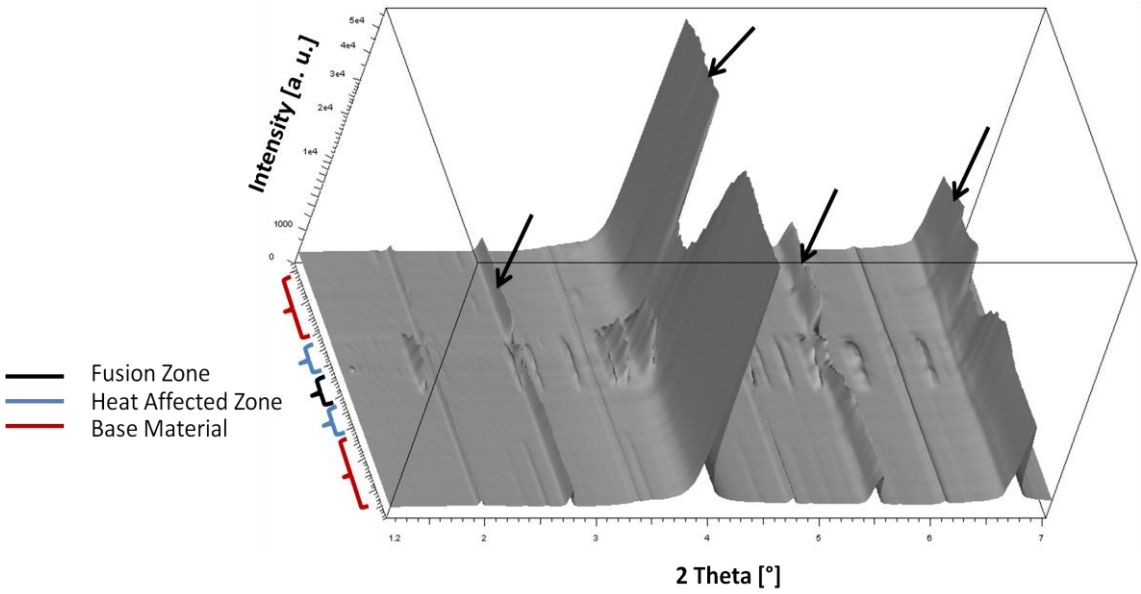

Figure 30 – XRD patterns along sample B-B (synchrotron radiation, 0.1426 Å wavelength).

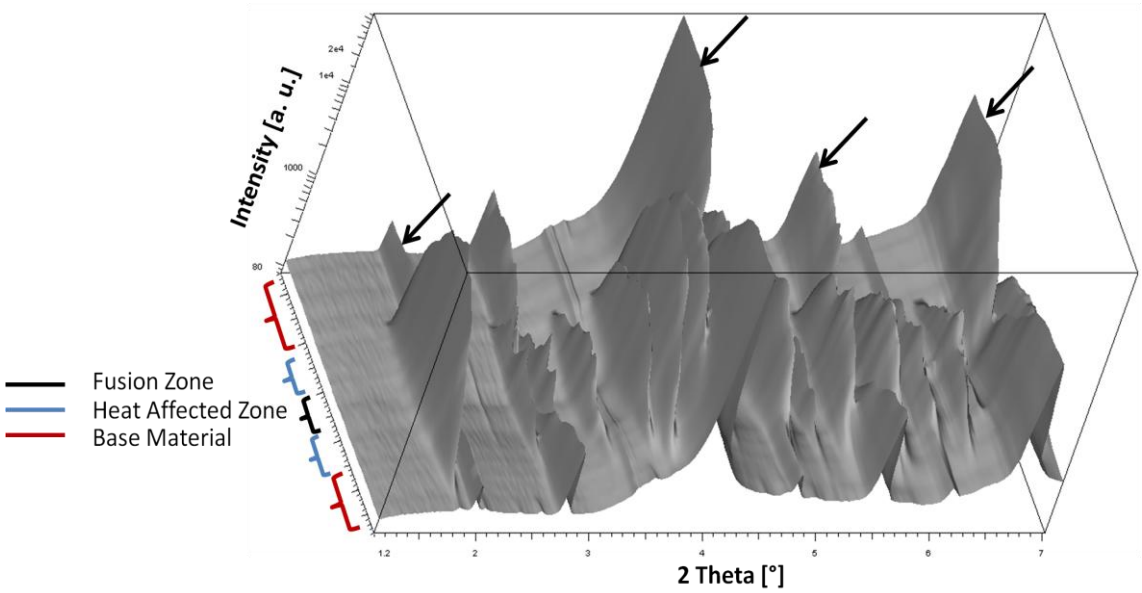

Figure 31 – XRD patterns along sample B-B after 4 cycles at 10% (synchrotron radiation, 0.1426 Å wavelength).

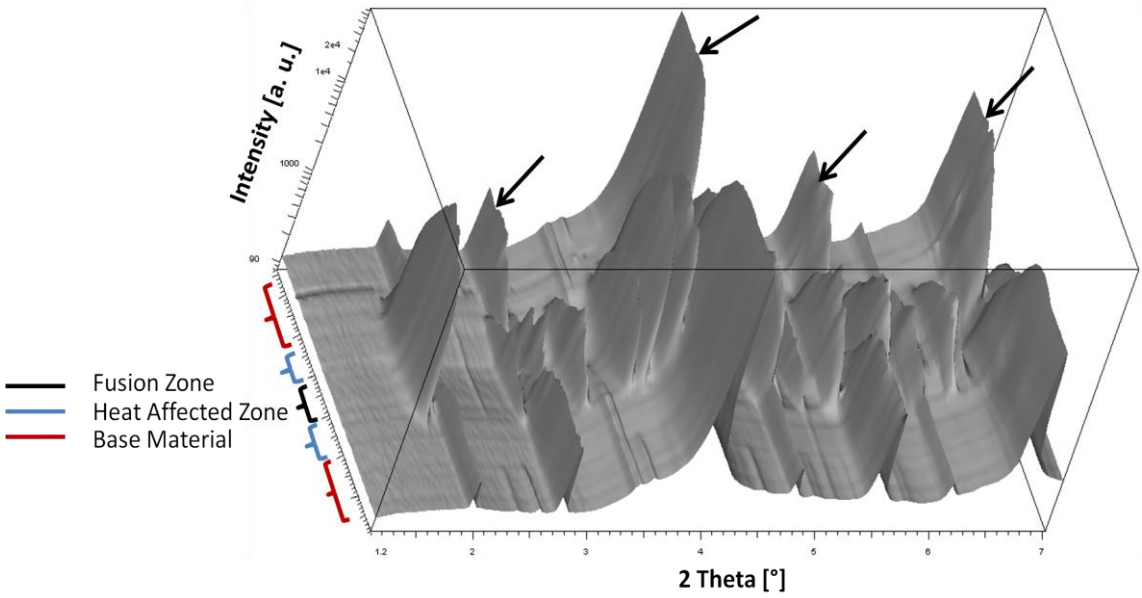

Figure 32 – XRD patterns along sample B-B after 600 cycles (synchrotron radiation, 0.1426 Å wavelength).

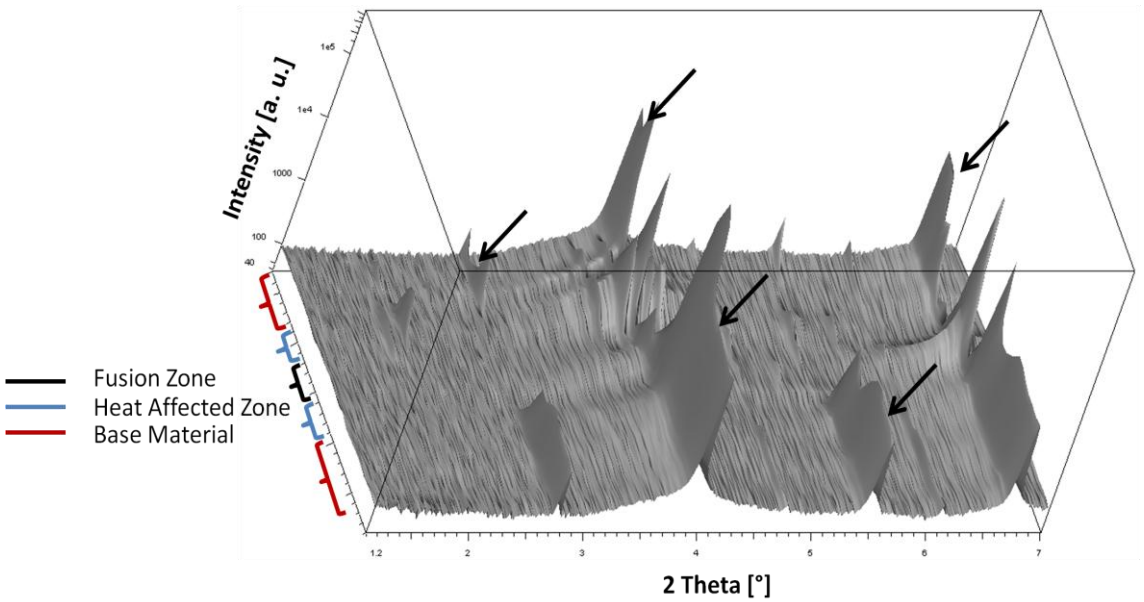

Figure 33 – XRD patterns along sample C-C (synchrotron radiation, 0.1426 Å wavelength).

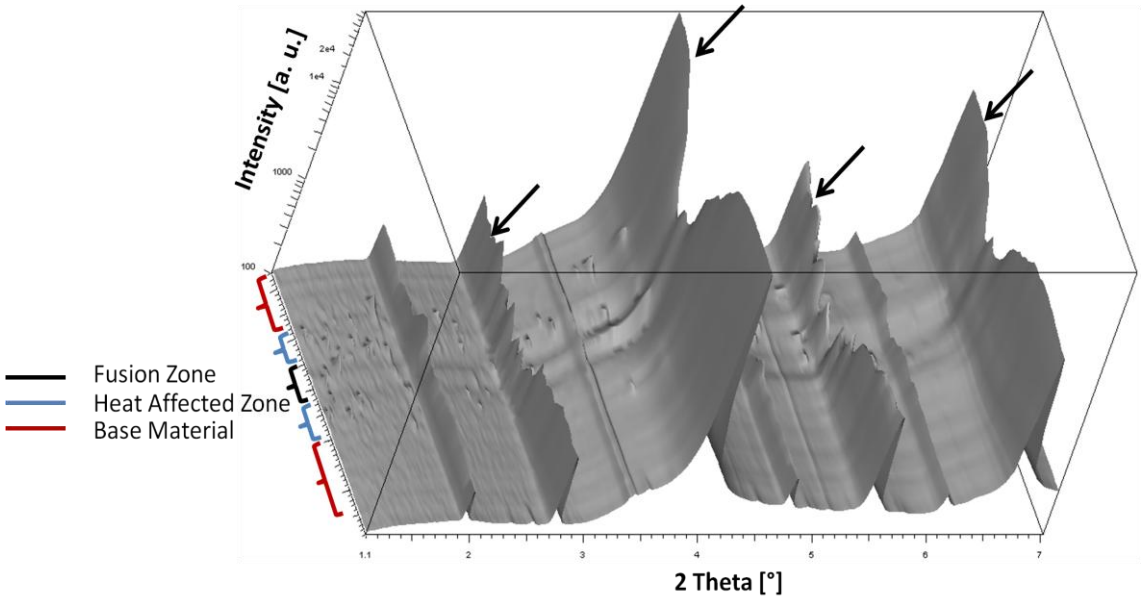

Figure 34 – XRD patterns along sample D-D (synchrotron radiation, 0.1426 Å wavelength).

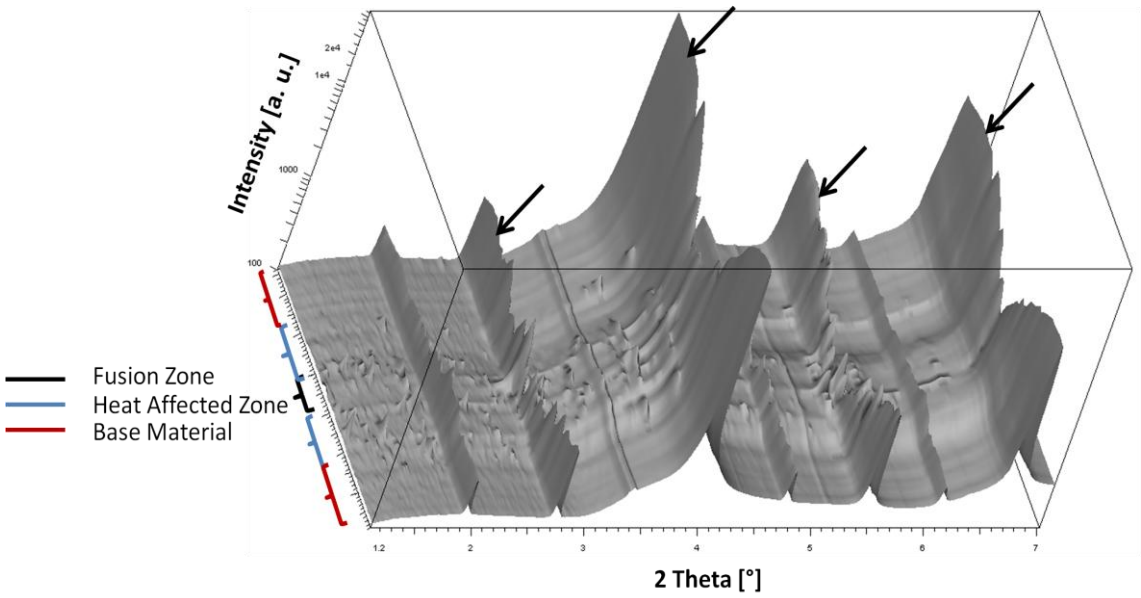

Figure 35 – XRD patterns along sample E-E (synchrotron radiation, 0.1426 Å wavelength).

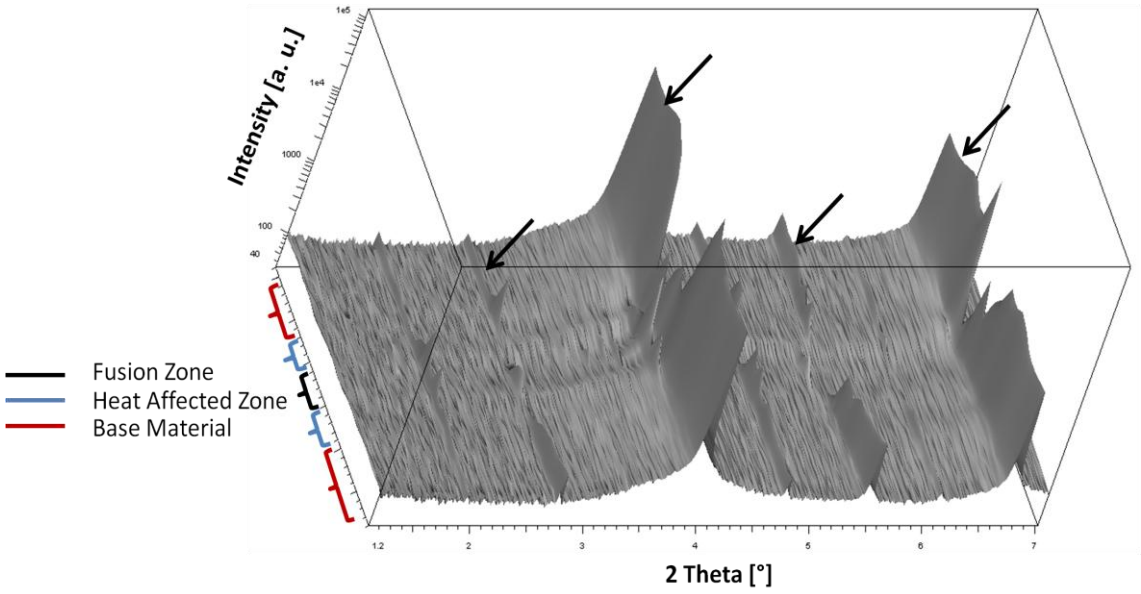

Figure 36 – XRD patterns along sample F-F (synchrotron radiation, 0.1426 Å wavelength).

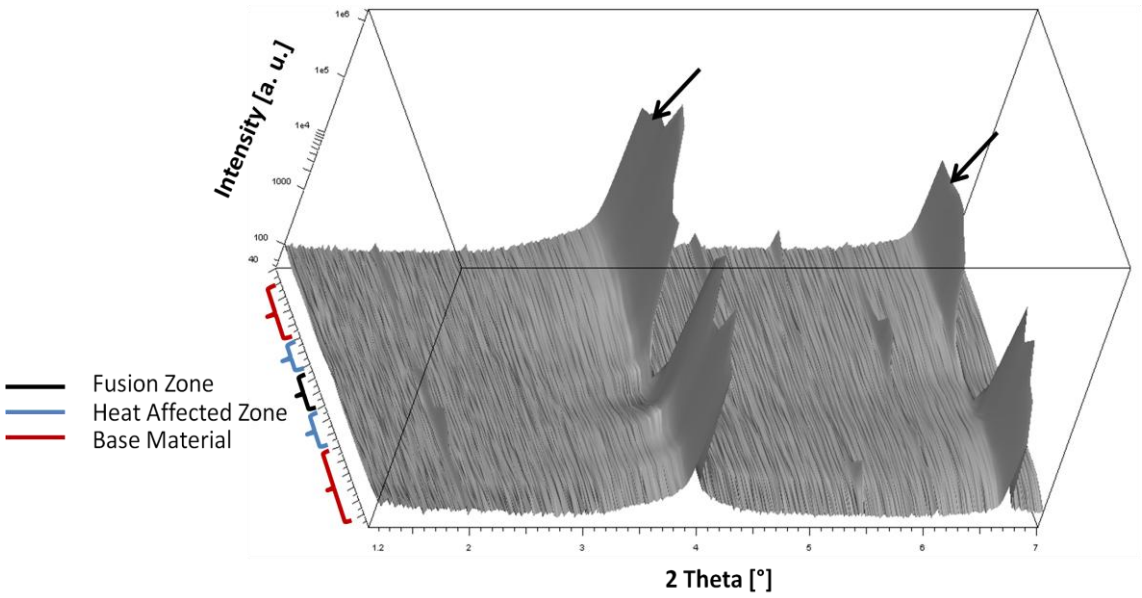

Figure 37 – XRD patterns along sample H-H (synchrotron radiation, 0.1426 Å wavelength).

From Figures 29 to 37 it is possible to verify the existence of different phases in each of the major regions of a weld (BM, HAZ and FZ). For all samples in the BM there is only austenite, while in HAZ and FZ there is martensite and austenite, but with a major prevalence of martensite in the FZ when comparing to austenite.

Tables 10 summarizes how the relative amounts of martensite and austenite in the BM, HAZ and in the FZ vary amongst different samples with 1.0 mm thickness.

Table 10 – Summary of the existing phases present in different zones of the analyzed samples 1.0 mm thick

Summary of the existing phases and their relative amounts between samples welded with the same laser power	
Samples A-A, B-B and C-C	All samples have martensite and austenite in the FZ. Sample A-A has a higher amount and sample C-C the lower amount of martensite. In the BM there is only austenite.
Samples D-D, E-E and F-F	Sample D-D and E-E have approximately the same amount of martensite, with a slight increase for sample E-E. Sample F-F has a lower amount of martensite than samples D-D and E-E. In the BM there is only austenite.

Sample B-B after 4 and 600 cycles presents a higher amount of martensite in the HAZ and in the FZ when comparing with sample B-B without any mechanical cycle. Sample H-H had also martensite and austenite in the weld bead with a greater prevalence of martensite.

3.2.2.2 - 0.5 mm thick samples

The XRD patterns along the samples F-F, K-K and O-O are depicted in Figures 38 to 40.

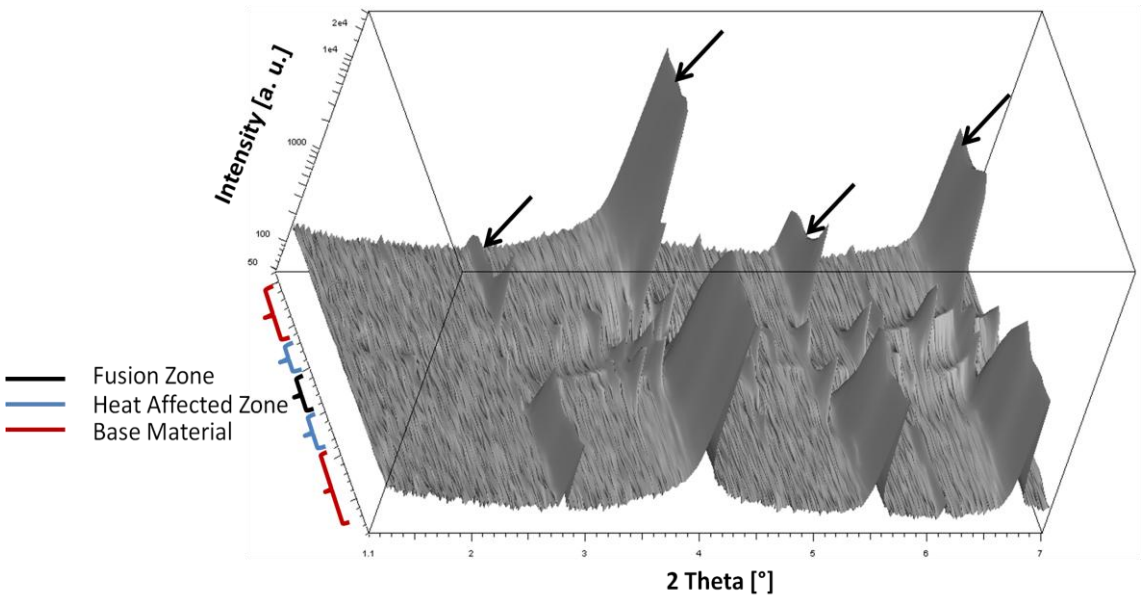

Figure 38 – XRD patterns along sample F-F (synchrotron radiation, 0.1426 Å wavelength).

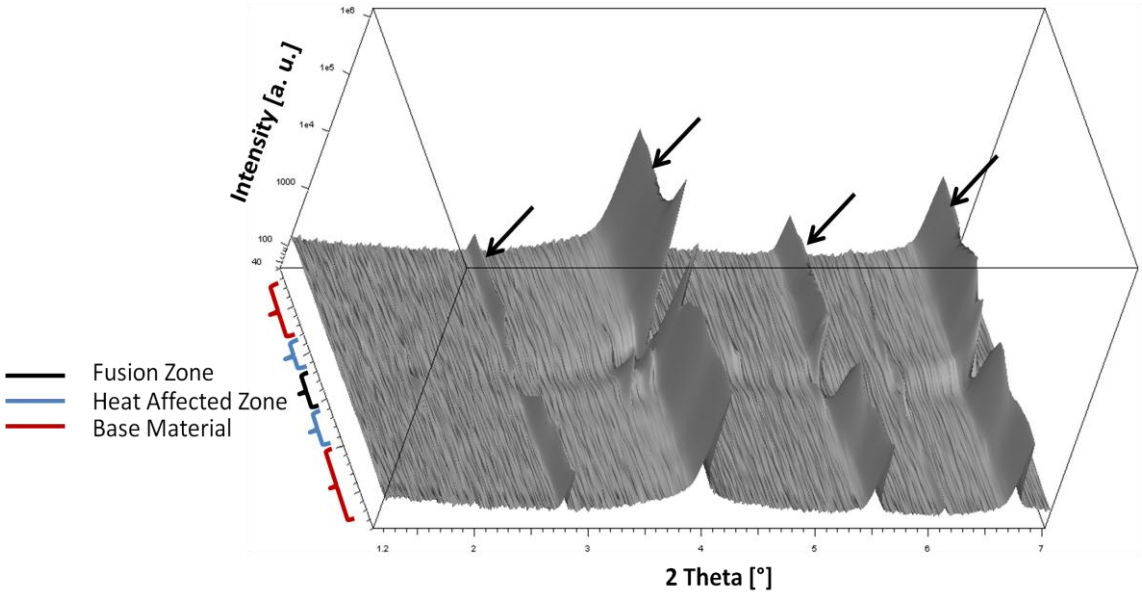

Figure 39 – XRD patterns along sample K-K (synchrotron radiation, 0.1426 Å wavelength).

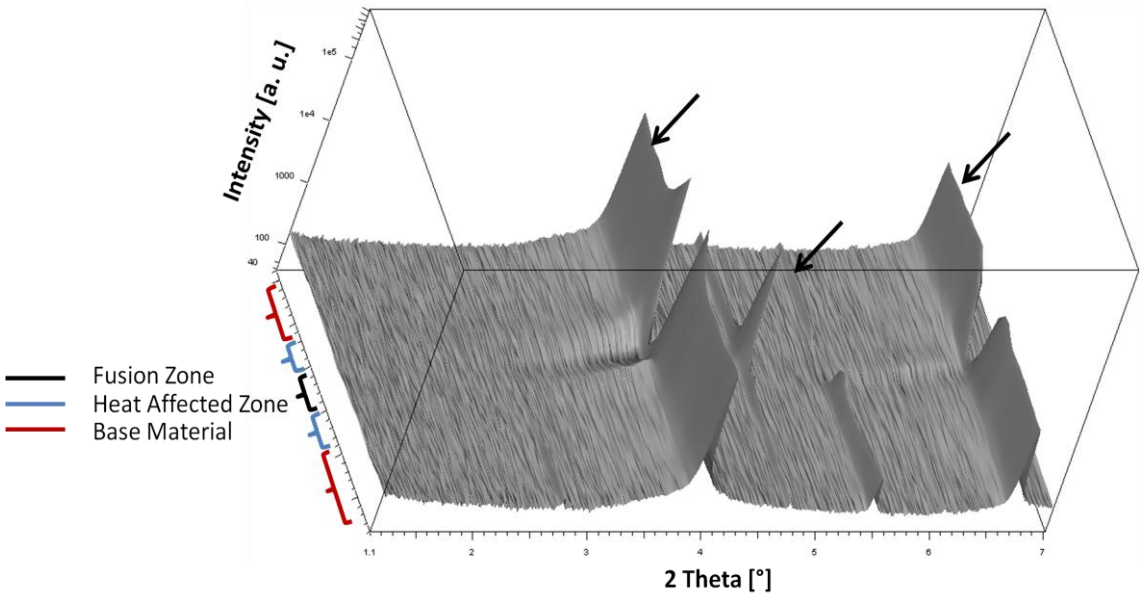

Figure 40 – XRD patterns along sample O-O (synchrotron radiation, 0.1426 Å wavelength).

For 0.5 mm thick samples there is also only austenite in the MB, while HAZ and FZ both have martensite and austenite. As it will be discussed later for these samples there is no possibility to make a reasonable comparison between the relative amounts of martensite existing in each sample.

3.4 - Cycling Behavior

3.4.1 - 1.0 mm Samples

3.4.1.1 - Cycling Tests

The results obtained from the cycling tests performed on 1.0 mm thick samples are summarized in Table 11.

Table 11 – Summary of the cycling tests performed on 1.0 mm thick welded samples

Summary of the cycling tests performed on 1.0 mm thick welded samples				
Sample reference	Rupture at			
	Number of test set	Cycle number	Total cycles	Where
A-A	5	61	301	Base material
B-B	No rupture	-	600	-
C-C	No rupture	-	600	-
D-D	No rupture	-	600	-
E-E	No rupture	-	600	-
F-F	No rupture	-	600	-
H-H	1	45	45	Weld bead

Figures 41 to 47 present the evolution of the cycling behavior for samples with 1.0 mm thickness.

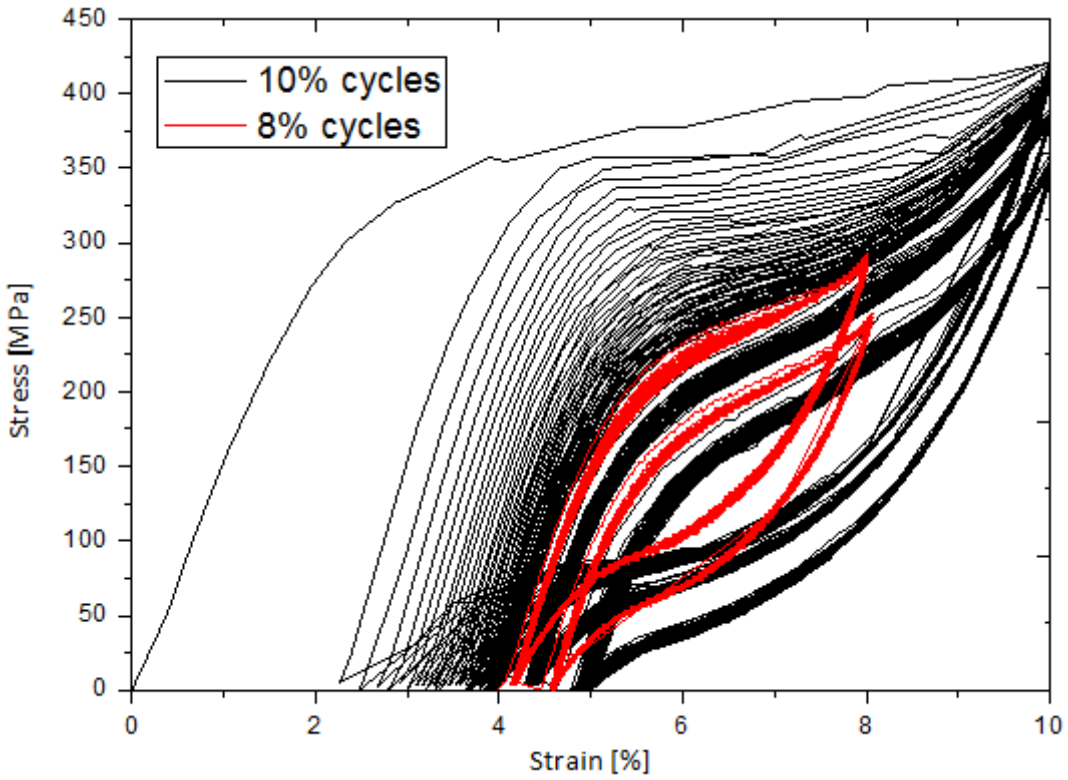

Figure 41 – Cycling test of sample A-A.

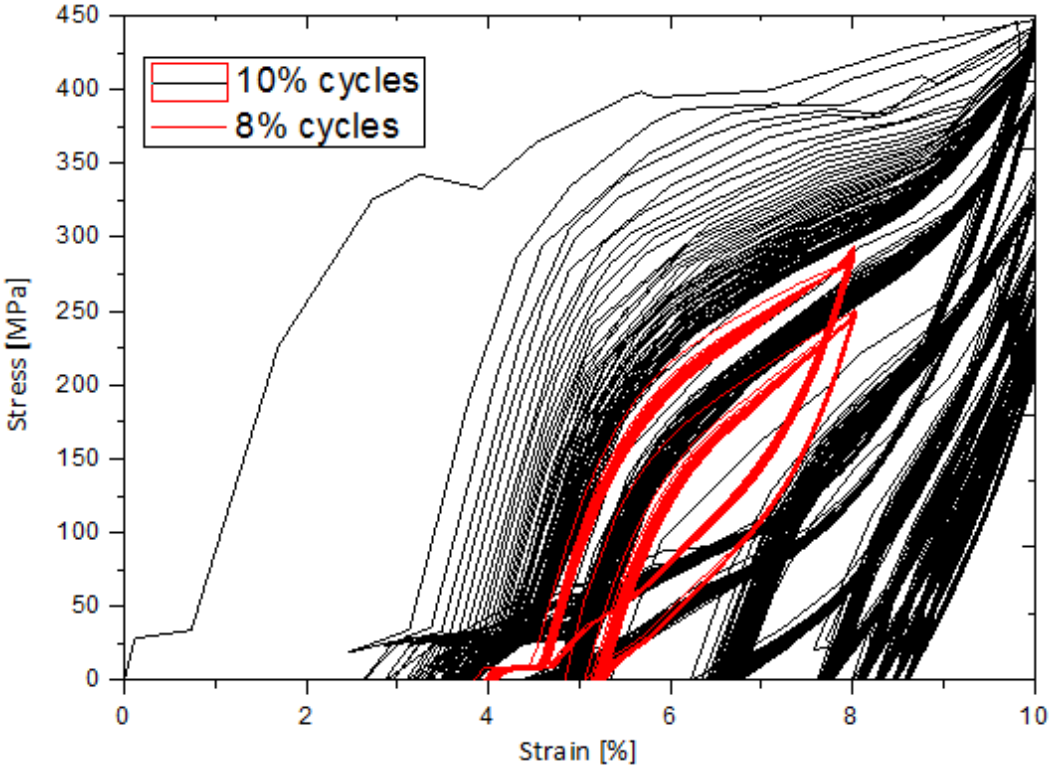

Figure 42 – Cycling test of sample B-B.

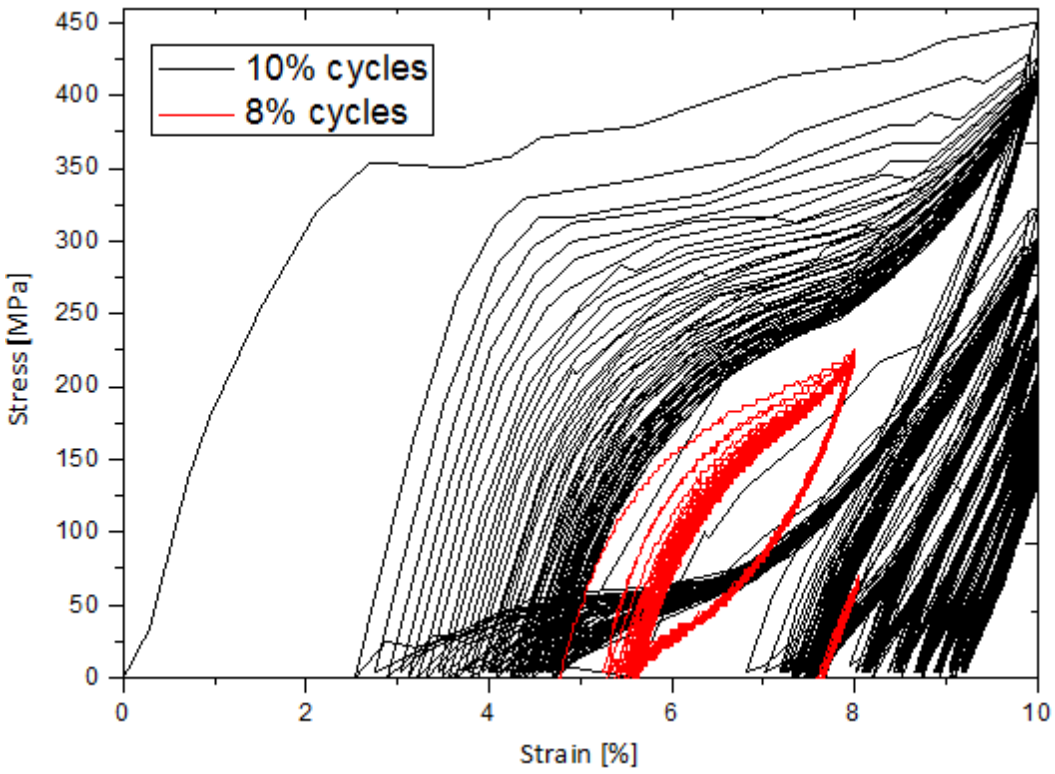

Figure 43 – Cycling test of sample C-C.

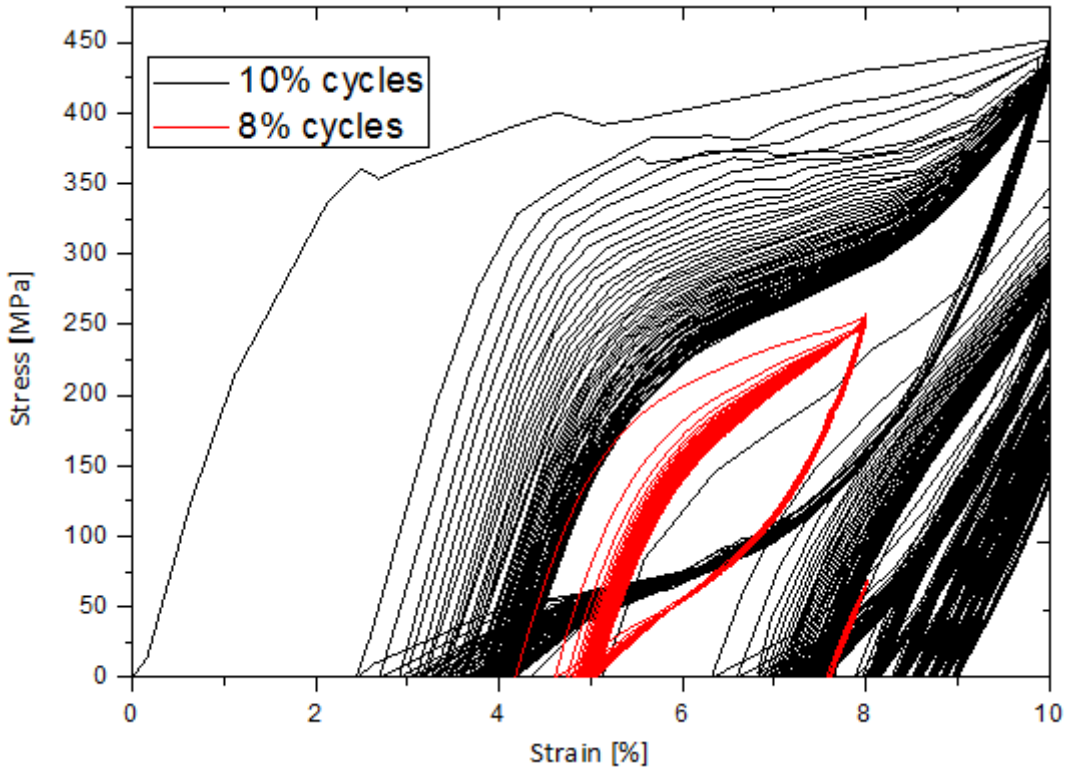

Figure 44 – Cycling test of sample D-D.

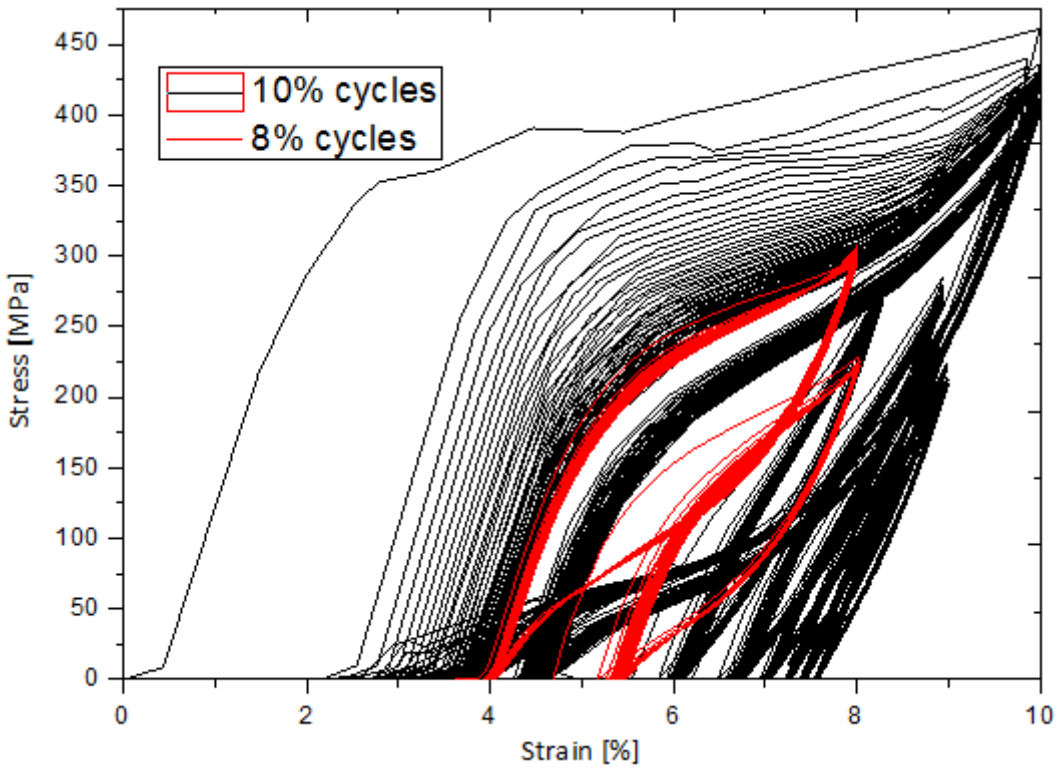

Figure 45 – Cycling test of sample E-E.

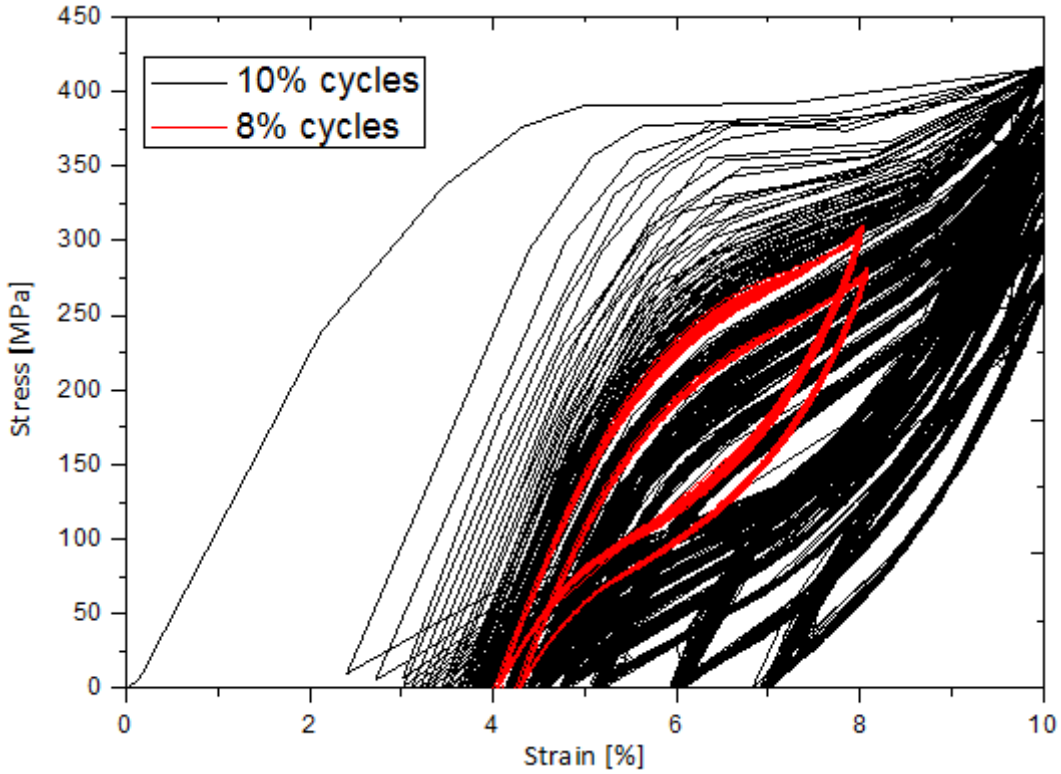

Figure 46 – Cycling test of sample F-F.

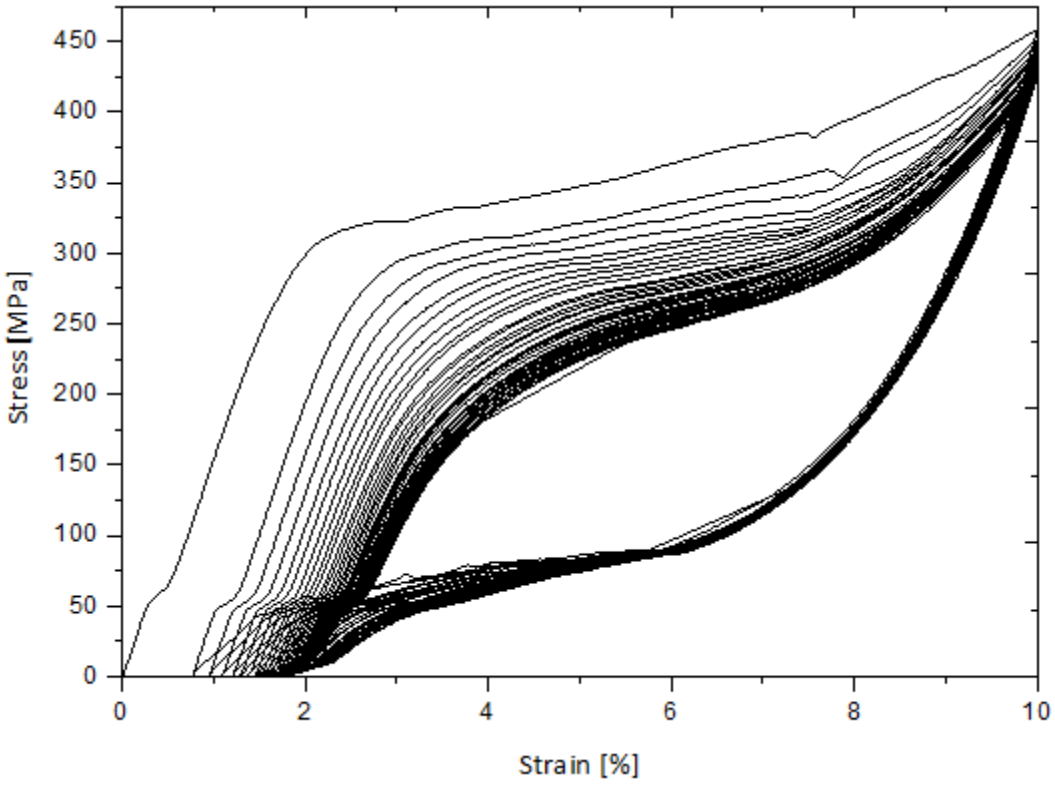

Figure 47 – Cycling test of sample H-H.

The cycling tests show that, for all samples, there is a convergence of the hysteretic loops from the first cycle to the last one of each cycling test. The superelastic plateau is clearly defined on the first set of the tests performed. On the following sets of the cyclic tests this plateau is not as evident as it was on the first set, though it is still present.

There is also a decrease in the stress of the SIM and reverse transformation with the increase of the number of cycles. This decrease is larger in the SIM transformation than in the reverse transformation.

Samples B-B, E-E and H-H show the existence of R-phase. Sample B-B shows the existence of two different SIM regions that only appear in the initial cycles of the first set of cycling tests. For sample B-B in the fourth set of cycling tests (second set of red lines in the cycling result) there is only elastic deformation without SIM regions due to a high increase of the accumulated irrecoverable strain in the previous cycles. A zoom from the beginning of the cycling test for sample B-B is depicted in Figure 48, to evidence the existence of R-phase associated to the existence of a plateau below 100 MPa.

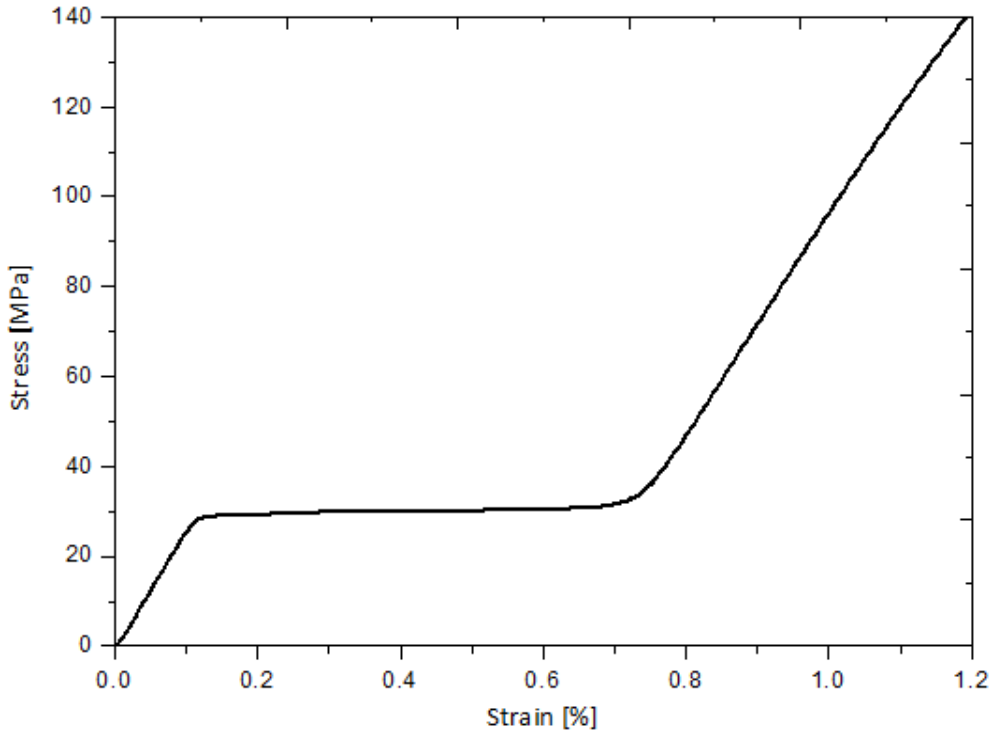

Figure 48 – Zoom from the beginning of the cycling test of sample B-B to show the existence of R-phase.

The irrecoverable strain after the first cycle is higher than 2% for all samples, except for sample H-H where it is lower than 1%.

3.4.1.2 - Accumulated Irrecoverable Strain

As it can be depicted on the cycling tests presented above the accumulated irrecoverable strain with the number of cycles of each sample differs. Table 12 summarizes the final value of accumulated irrecoverable strain at the end of the cycling test performed. During the "Discussion" section, several Figures with the evolution of the accumulated irrecoverable strain with the number of cycles will be presented in order to facilitate the interpretation of the results attained.

Table 12 – Summary of the accumulated irrecoverable strain after the cycling test for 1.0 mm thick samples

Summary of the maximum accumulated irrecoverable strain		
Sample	**Number of cycles**	**Accumulated irrecoverable strain after the cycling test [%]**
A-A	301	5.01
B-B	600	8.62
C-C	600	9.21
D-D	600	9.01
E-E	600	8.99
F-F	600	7.21
H-H	45	1.93

It must be noticed that all samples undergoing the entire cycling routine present an accumulated irrecoverable strain after the test ranging from 7.21 to 9.21%.

3.4 .2 - 0.5 mm Samples

3.4.2.1 - Cycling Tests

Table 13 summarizes the results of the cycling tests performed on 0.5 mm thick samples.

Table 13 – Summary of the cycling tests performed on 0.5 mm thick welded samples

Summary of the cycling tests performed on 0.5 mm thick welded samples				
Sample reference	Rupture at			
	Number of test set	Cycle number	Total cycles	Where
F-F	1	35	35	Base material
K-K	No rupture	-	600	-
O-O	1	38	38	Base material

Figures 49 to 51 depict the cycling test results of 0.5 mm thick samples.

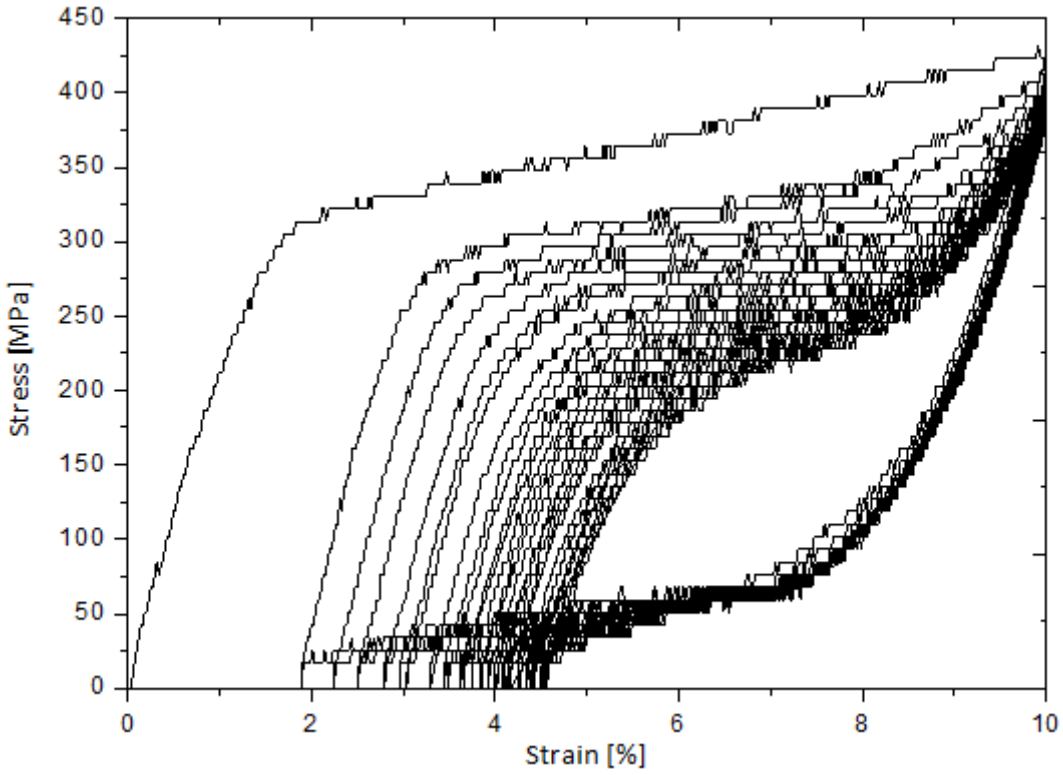

Figure 49 – Cycling test of sample F-F.

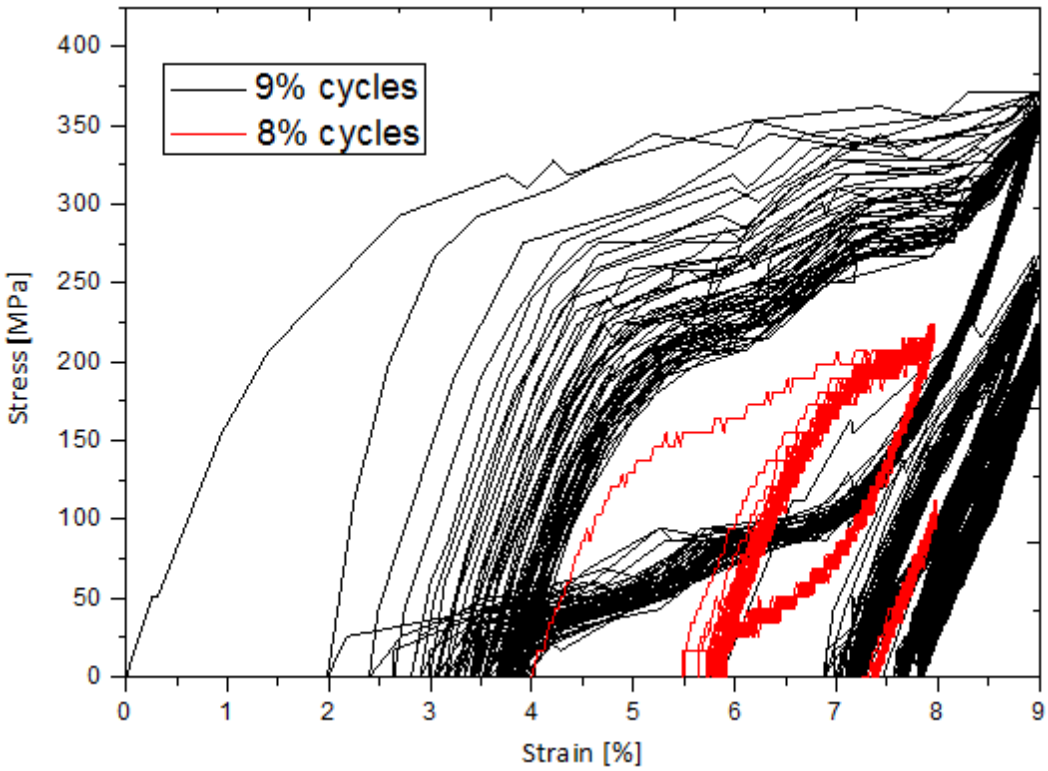

Figure 50 – Cycling test of sample K-K.

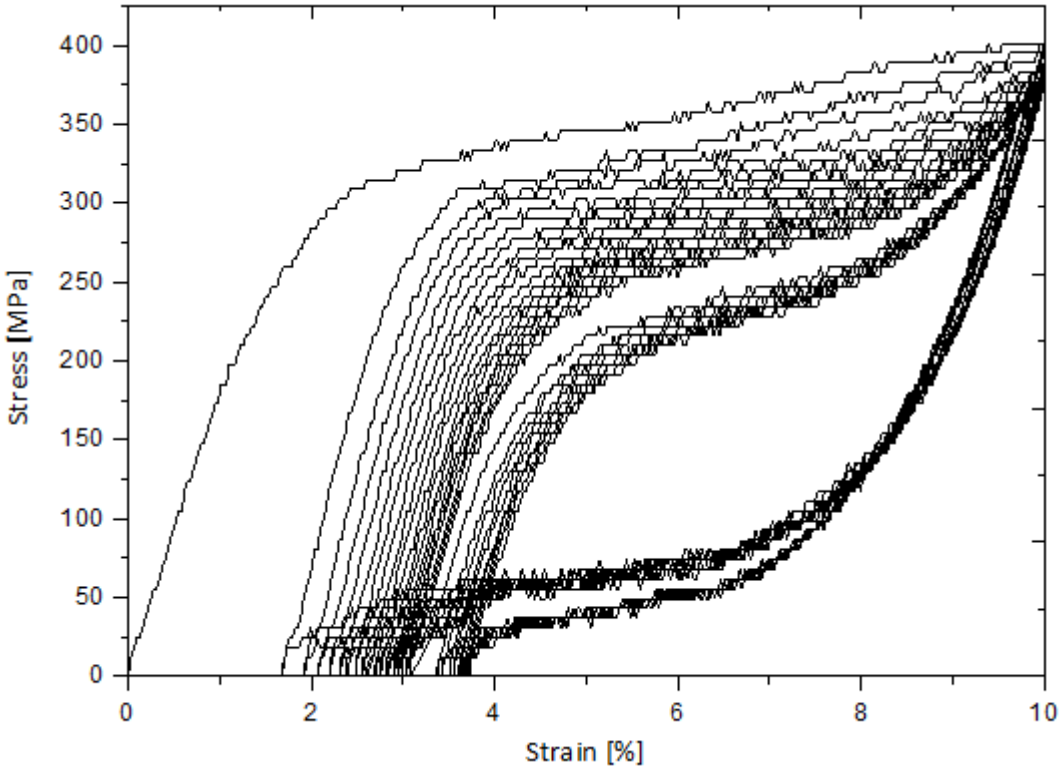

Figure 51 – Cycling test of sample O-O.

The observations of 0.5 mm thick samples are very similar to the ones mentioned for 1.0 mm thick samples. Namely, the convergence of the hysteretic loops from the first to the last cycle

and the decrease of the stress to induce SIM and the reverse transformation with the increase of the number of cycles. Sample K-K was the only one that was able to stand the full cycling routine without rupture, although the maximum strain achieved for this sample was 1% lower than for samples F-F and O-O. For sample F-F and O-O the superelastic plateau is well defined, while for sample K-K this good definition is only visible on the first and second sets of the cycling test. During In the fourth set of cyclic tests sample K-K only shows elastic deformation.

Samples F-F and O-O both suffered rupture in the BM in the first set of cycling tests after a total of 35 and 38 cycles, respectively.

3.4.2.2 - Accumulated Irrecoverable Strain

Since the samples F-F and O-O suffered rupture at a low number of cycles when comparing to sample K-K in Table 14 we present the accumulated irrecoverable strain after cycles 35, for sample F-F, 38 for sample O-O, and 38 and 600 for sample K-K in order to make a reasonable comparison of the results attained.

Table 14 – Summary of the accumulated irrecoverable strain after the cycling test for 0.5 mm thick samples

Summary of the maximum accumulated irrecoverable strain		
Sample	**Number of cycles**	**Accumulated irrecoverable strain after the cycling test [%]**
F-F	35	4.70
K-K	38	3.79
O-O	38	3.87
K-K	600	7.86

For 0.5 mm thick samples will be also presented appropriated Figures, in the “Discussion” section in order to compare the evolution of the accumulated irrecoverable strain for all samples with the increase of the number of cycles.

3.5 - Shape Memory Effect Evaluation

The results attained from the SME evaluation are depicted in Table 15 in terms of the permanent deformation angle, Ω.

Table 15 – Summary of the results attained from SME tests

Summary shape memory effect tests performed	
Sample	**Permanent deformation angle Ω [degrees]**
MB1	0
MB2	0
Parallel	0
Perpendicular	2
K-K (0.5 mm)	0
K-K after 600 cycles	0
B-B after 600 cycles	0
C-C after 600 cycles	0
D-D after 600 cycles	0
E-E after 600 cycles	0
F-F (1.0 mm)	0
F-F after 600 cycles	0

Only the sample welded with the rolling direction perpendicular to the welding direction exhibits a permanent deformation angle, despite this value is almost negligible. For all samples, even for those who are cycled 600 times, there is no evidence that the SME is affected by the welding procedure.

3.6 - Scanning Electron Microscopy Observations

Figures 52 to 54 depicts the fracture surfaces of sample A-A (P = 990W, v = 25 mm/s).

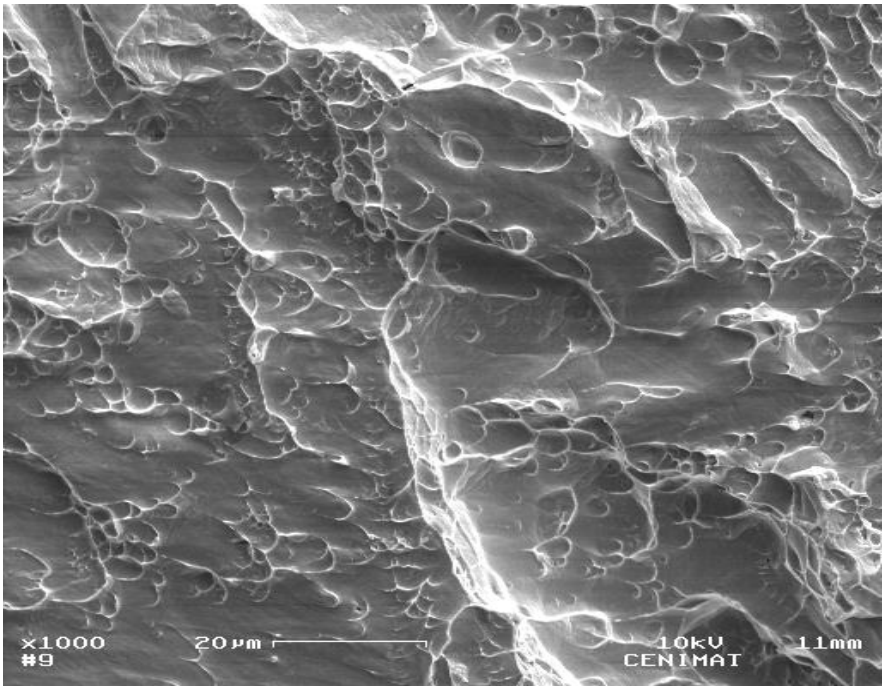

Figure 52 – SEM analysis of fracture surface of sample A-A.

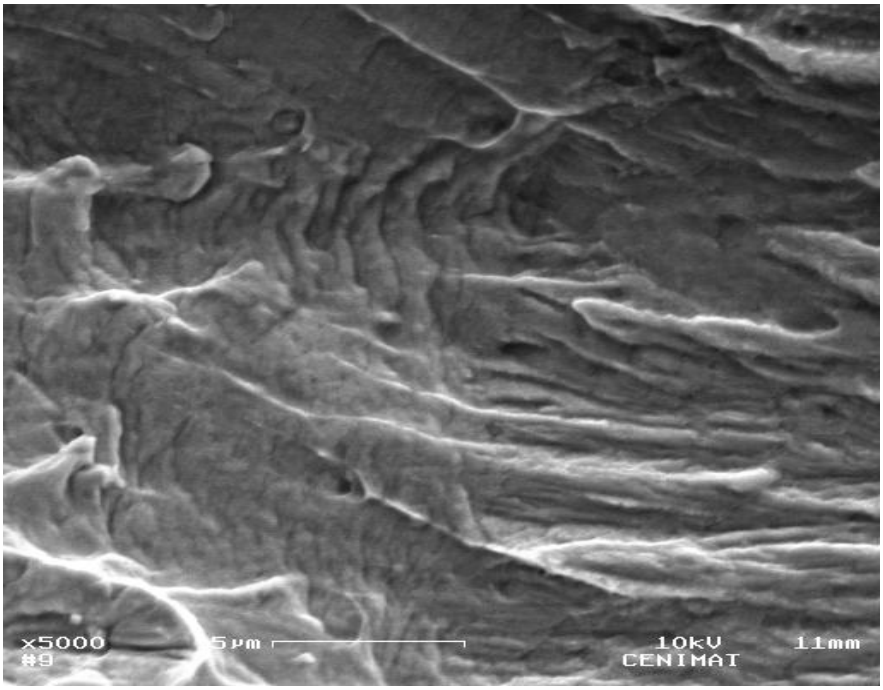

Figure 53 – SEM analysis of fracture surface of sample A-A.

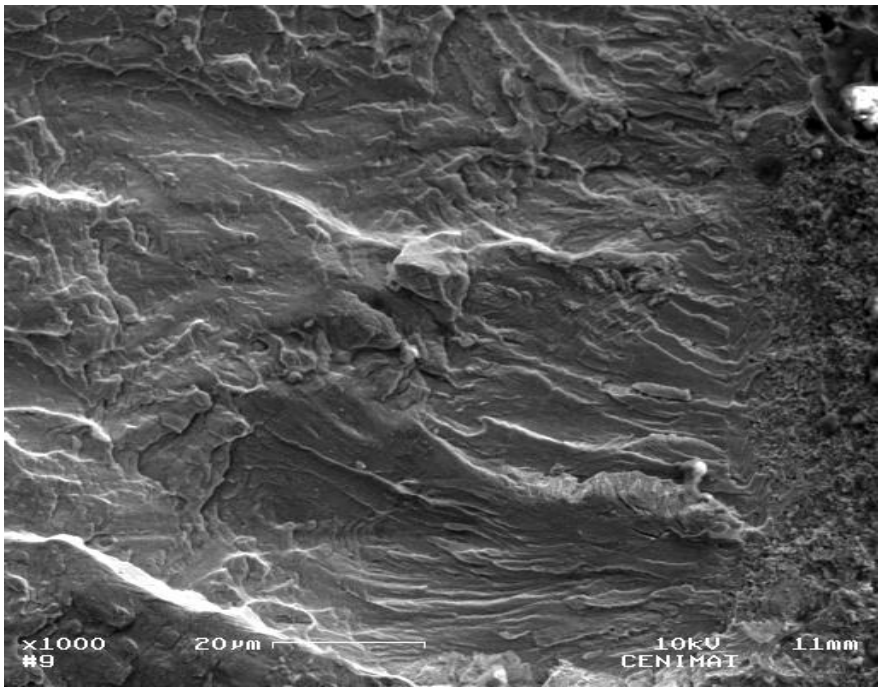

Figure 54 – SEM analysis of fracture surface of sample A-A.

Figures 52 and 53, correspond to the beginning of the fracture depicting the existence of dimples, as well as successive progression of the crack occurred due to fatigue. Figure 54, corresponding to the ending of the fracture shows that, at this final step, the crack spread in a catastrophic way, with a fragile character.

For sample H-H (P = 1980 W, v = 40 mm/s) the fracture surfaces are depicted in Figures 55 and 56.

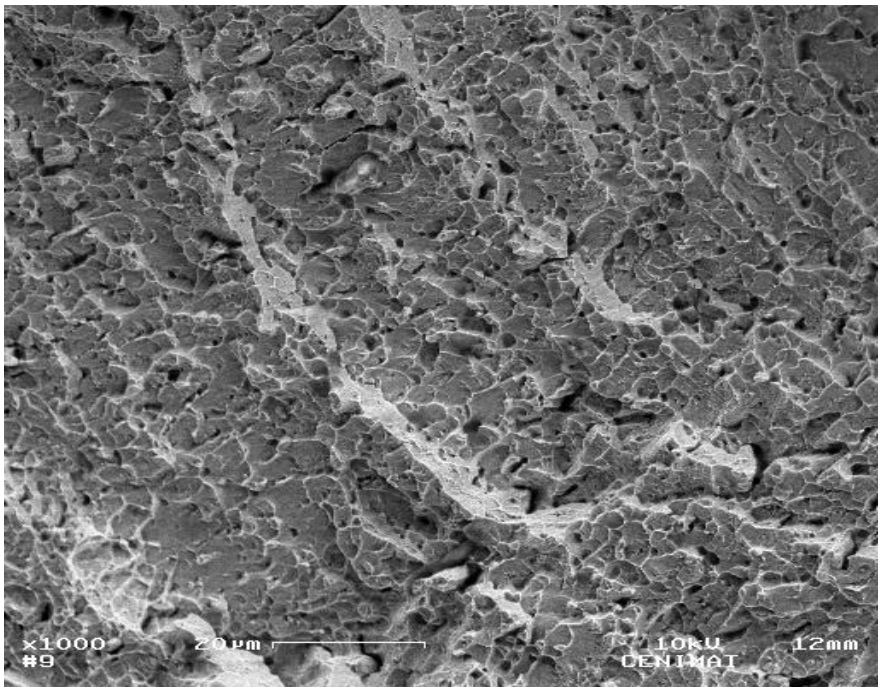

Figure 55 – SEM analysis of fracture surface of sample H-H.

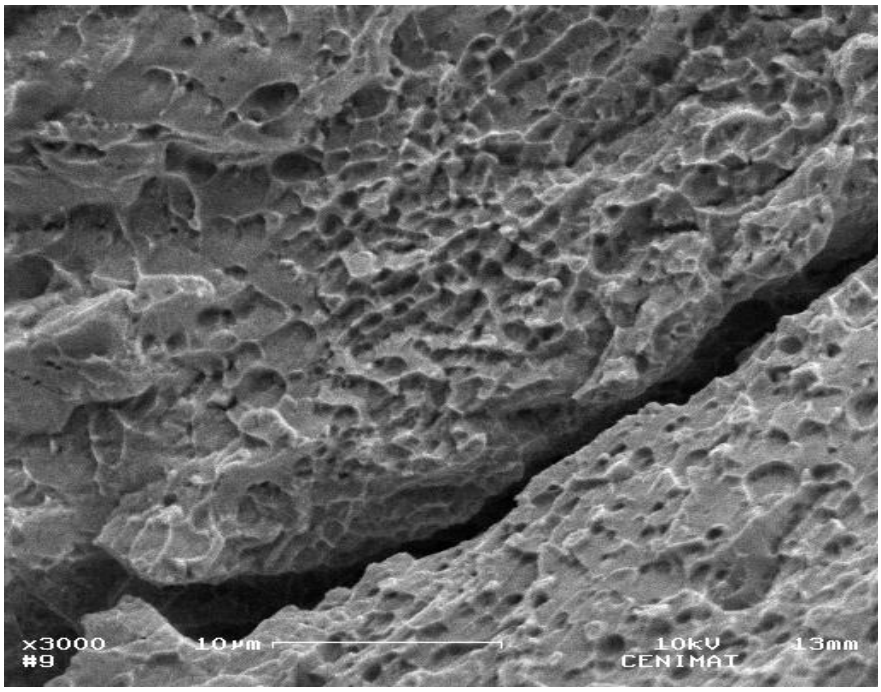

Figure 56 – SEM analysis of fracture surface of sample H-H.

For sample H-H there is also the existence of a large amount of dimples with a fragile character at the end of the fracture due to catastrophic propagation of the cracks.

4 - Discussion

The objective of this Thesis is to correlate the mechanical behavior under cycling of similar laser joints of NiTi with the structure of the weld bead and neighboring regions. This discussion will focus on how the laser welding procedure influences the welds microstructure and its mechanical behavior.

For 1.0 mm thick samples, the parameters can be discussed either individually (welding speed and laser power), or they can be discussed as a combination, where the heat input (HI) is analyzed. The present discussion will be done differently, that is, by fixing one of the parameters and varying the other and vice-versa.

During this discussion the XRD analysis, DSC and mechanical tests will be presented in order to determine the influence of the process parameters on the microstructure of the laser welded joints. This information will be used in order to understand the SE behavior of the welds under cyclic loading.

Finally, SEM of fracture surfaces of samples A-A and H-H that suffered premature rupture will be presented for trying to understand the fracture mechanisms underlying the failure of these samples under cyclic mechanical loading.

For 0.5 mm thick samples, due to the shortage of samples, when comparing to the 1.0 mm thick samples, the analysis will be made taking into consideration the HI introduced during the welding.

In the final section the SME evaluation of the analyzed samples will be presented.

4.1 - 1.0 mm thick samples

The 1.0 mm thick samples have shown a good performance under mechanical cycling. A total of 600 cycles was achieved, except for sample A-A, with strains up to 10%. Even for sample A-A, rupture occurred in the BM instead of the weld bead. The rupture in the BM may be due to the existence of surface defects on the plate that induced premature failure.

4.1.1 - Influence of the Welding Speed For a Fixed Laser Power

In this work the samples that were studied were welded with laser power of 990, 1485 and 1980 W. For each laser power used, three different welding speeds were tested (resulting in three different samples for each laser power chosen), except for laser power of 1980 W, where just one sample was tested. For this reason the study about the influence of the different welding parameters was limited to the samples welded with 990 and 1485 W.

The samples welded with the laser power mentioned before show a similar behavior regarding the number of cycles that were able to stand during the cycling tests. Only one sample suffered premature rupture at 301 cycles, while all other samples lasted for the entire cycling routine (600 cycles). For this reason we will now start this discussion with two different sub-section where we analyze the influence of the welding speed by fixing the laser power and the influence of laser power by fixing the welding speed. Another sub-section was added to verify the influence of the HI introduced during welding on the samples.

4.1.1.1 - Influence of Welding Speed for a Laser Power of 990 W

For the samples with a laser power of 990 W the main differences are evident in the evolution of the accumulated irrecoverable strain with the number of cycles. The cycling tests just by themselves do not present big differences between the samples. For this reason, in first place we present and discuss the evolution of the accumulated irrecoverable strain and next, the small differences in the cycling tests will be discussed in greater detail, taking into consideration what was already mentioned during the discussion of the evolution of the accumulated irrecoverable strain.

In this sub-section, samples to be analyzed are sample A-A, B-B and C-C, with welding speed of 25, 20 and 15 mm/s, respectively.

The accumulated irrecoverable strain for samples A-A, B-B and C-C is depicted in Figure 57.

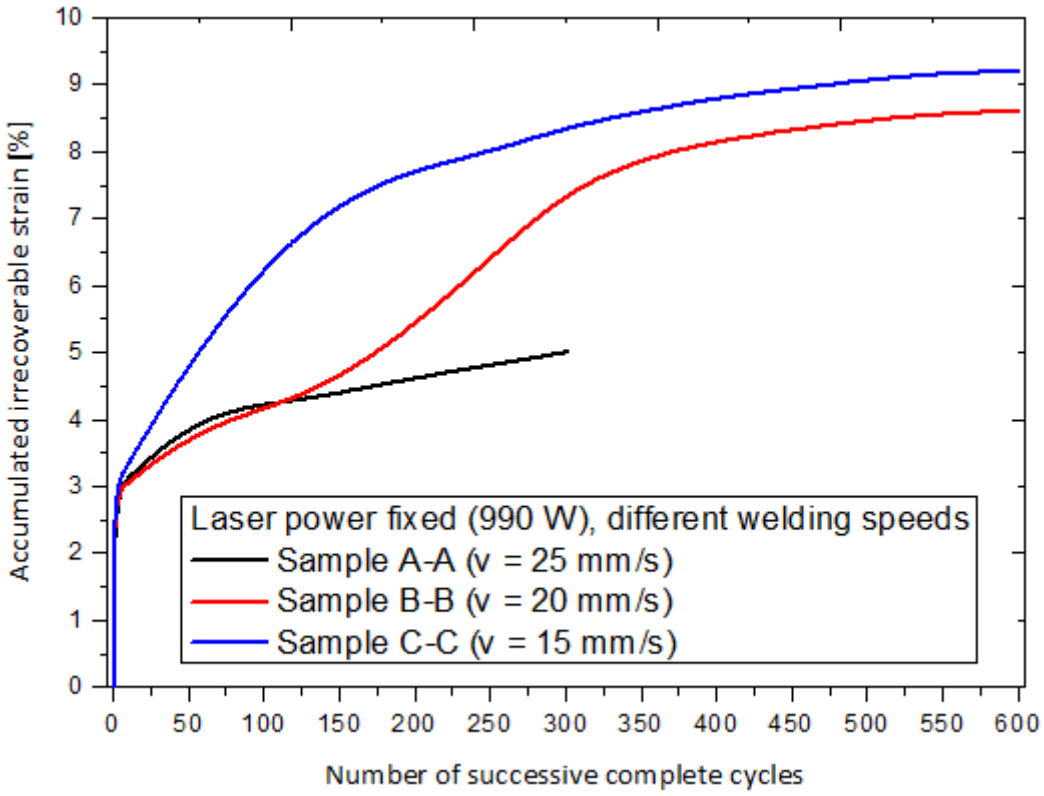

Figure 57 – Comparison between the accumulated irrecoverable strain over the number of successive cycles for samples A-A, B-B and C-C.

Before beginning the discussion about the behavior present in Figure 57, it must be taken into consideration that XRD of the welded samples shows that all samples have both austenite and martensite in the FZ and in the HAZ. The relative amounts of each phase in these zones vary, as it will be discussed. In the BM there is only austenite, as expected, since there was no influence of the thermal cycle in this zone. All these features are crucial to understand the behavior presented by the samples.

For all samples the irrecoverable stain after the first cycle is above 2%. This high value of irrecoverable strain after the first cycle is due to martensite stabilization. This stabilization consists in the transformation of twinned martensite, that exist in the weld bead, to

detwinned martensite meaning that part of the shape is not recovered during the unloading. It could be recovered by heating the sample above A_f. This martensite exists in the welded samples as a result of the welding process and the stress applied leads to generation of detwinned martensite and, as a consequence, there is a significant irrecoverable strain after the first cycle. After martensite stabilization the accumulated irrecoverable strain tends to increase, due to localized stresses that tend to exceed the stress to induce detwinned martensite. By heating the samples above $A_{f,}$ part of the detwinned martensite existing in the FZ and in the HAZ, as a result of the cycling tests, become austenite and thus, at least some part of the original shape of the welded specimens would be recovered due to the SME. However it must be noted that, may not be enough eating up to A_f since, when in the presence of some internal stresses the temperature to achieve the start and the finish of the austenitic phase rises as stated by Tobushi *et al*. [29]

The stabilization of martensite is very clear when taking in consideration the XRD analysis made in sample B-B without any mechanical cycling and after 4 and 600 cycles. While in the uncycled sample there is evidence of some martensite in the weld bead, in the sample that was cycled four times there is evidence of a great amount of martensite in this zone, due to stabilization of martensite referred above. After 600 cycles the amount of martensite increases very slightly, when compared to the sample cycled four times. This means that the stabilization of martensite occurs significantly in the first cycles, which allows to understand the quick increase of the accumulated irrecoverable strain in those early cycles. The stabilization of martensite occurs due to increase of the dislocation density that tends to block the interface, and thus do not allow the reversible transformation to occur.

Around the 25^{th} cycle the accumulated irrecoverable strain of sample C-C tends to increase much more than in samples A-A and B-B. The evolution with the number of cycles is not equal for all samples, since for sample B-B and C-C there is evidence of stabilization of the accumulated irrecoverable strain after the 500^{th} cycle, while for sample A-A there is no evidence, as the sample suffered premature rupture.

The reason why sample C-C shows a higher accumulated irrecoverable strain when compared to sample A-A and B-B for the same number of cycles may be explained as follows: although both samples have been welded with the same laser power, the welding speed was different. Sample C-C had a welding speed lower than sample A-A and B-B which gives to sample C-C a higher value of HI during the welding. With the increase of the HI the HAZ and the FZ tend to have a higher extension, which may amplify the possible effects of the welding process on the material. As stated previously, the transformation temperatures of NiTi alloys are strongly dependent on the chemical composition and laser welding may cause compositional changes in the FZ and in the HAZ as a result of volatilization of elements (which may occur in the FZ), due to oxidation phenomena or, most likely, due to the dissolution of pre-existing precipitates which reprecipitation is not enabled, leading to a change in the temperature transformation of the FZ and the HAZ. This may imply that at room temperature, at which the cycling tests were performed, instead of having the samples fully austenitic, since the BM had an A_f temperature of about 24 °C, it is possible to exist martensite at room temperature in the referred areas, as shown be the XRD analysis. Taking that into consideration, it can be said that a higher HI will

gives rise to a higher extension of the FZ and the HAZ and, as a consequence, more martensite exists in the specimens due to a greater effect of the HI in the welded specimens.

Also in the FZ there are compressive stresses, while in the HAZ there are tensile stresses. [30] If the HAZ of sample C-C is wider, then, in the early cycles, is easier to achieve stress states that induce this irrecoverable strain. In the following cycles due to the accumulation of residual stresses during the cycling tests, the compression stress in the FZ tend to decrease, but since sample C-C has a bigger FZ and a higher amount of martensite, it is easier to achieve the stress to induce the transformation from detwinned to twinned martensite, thus increase the accumulated irrecoverable strain with the number of cycles.

These considerations can be valid since for samples A-A and C-C the XRD analysis depicts that there is a higher amount of martensite in the HAZ and in the FZ than for sample A-A. The higher amount of martensite in sample A-A is due to a higher value of HI when compared to sample C-C. Sample B-B has an amount of martensite intermediate between samples A-A and C-C, according to the XRD analysis, which allows to understand why the curve of the accumulated irrecoverable strain is between the curves of samples A-A and C-C.

Aside from the considerations mentioned above, part of the irrecoverable strain presented by the specimens may be due to the introduction of defects due to the welding process and/or to dislocations into the HAZ during the loading path. [20]

It must be noticed also that the accumulated irrecoverable strain increase with the number of cycles is not only due to the existent martensite, since there is austenite in the BM and this part of the specimens are also subjected to stresses during the cycling tests. Part of the increase in the irrecoverable strain can also be explained taking in consideration that during the cycling tests performed, the austenite/martensite interface in the BM travels forward and backward in the specimens, causing to pile up dislocation around scattered defects which will cause an accumulation of microscopic residual stresses, and in the end will have an important effect on the macroscopic response of the tested specimens. [31]

The existence of martensite in the FZ, as stated before, may be due to a preferential volatilization of Ni compared to Ti (see section 1.6.2 – Laser Welding of NiTi Similar Joints). Since the vapor pressure of Ni is of two orders of magnitude higher than Ti, it means that the evaporation rate of Ni will be significantly higher than for Ti. The evaporation of Ni may explain the existence of martensite in the FZ at room temperature, since that for M_s being higher than room temperature it is needed an enrichment in Ti, which may occur due to the preferential evaporation of Ni. Despite the use of a shielding gas during welding to prevent a significant evaporation of elements, since the transformation temperatures are quite dependent of the chemical composition of the matrix, the preferential evaporation of Ni (which is equivalent to a Ti enrichment), even in a small scale, could lead to a significant change in the transformation temperatures, in particular, by raising M_s above room temperature.

It is known that Ni has a higher vapor pressure than Ti at high temperatures (see Figure 19 where it were calculated the values of vapor pressure for both elements as a function of temperature, taking in consideration [22]). A higher vapor pressure is equivalent to a higher evaporation rate.

Oxidation phenomena may also have occurred, since Ti has a higher tendency to oxidize than Ni. [32] If, in fact, oxidation of Ti had occurred the molar fraction of Ti would decrease causing also a decrease in the M_s temperature. Since in the HAZ and in the FZ there is martensite it is not possible that the M_s temperature had decrease, instead, it should have increased.

This will lead to another possibility to explain the existence of martensite in the HAZ: i) during heating if the temperature is high enough it could lead to full solution; ii) during cooling depending on the cooling rate it could enable the precipitation. In the zones where the temperature was higher and full solution may have existed, the cooling rate is higher which may not enabled re-precipitation. In the zones where the temperature was not enough to occur full solution the cooling rate was lower, which may have enabled Ni rich precipitates, as Ni_3Ti or Ni_4Ti_3. These Ni-rich precipitates will cause a Ti enrichment of the surrounding matrix. A higher Ti content will cause an increase of the transformation temperatures, in particular, M_s is higher than the room temperature, which justifies the existence of martensite in the samples at room temperature.

Figure 58 depicts a "bump" in a 2Θ value corresponding to a peak position for Ni_4Ti_3. This "bump" however is only visible in the HAZ (black line), while in the FZ (red line) and in the BM (blue line) there is no evidence of the "bump".

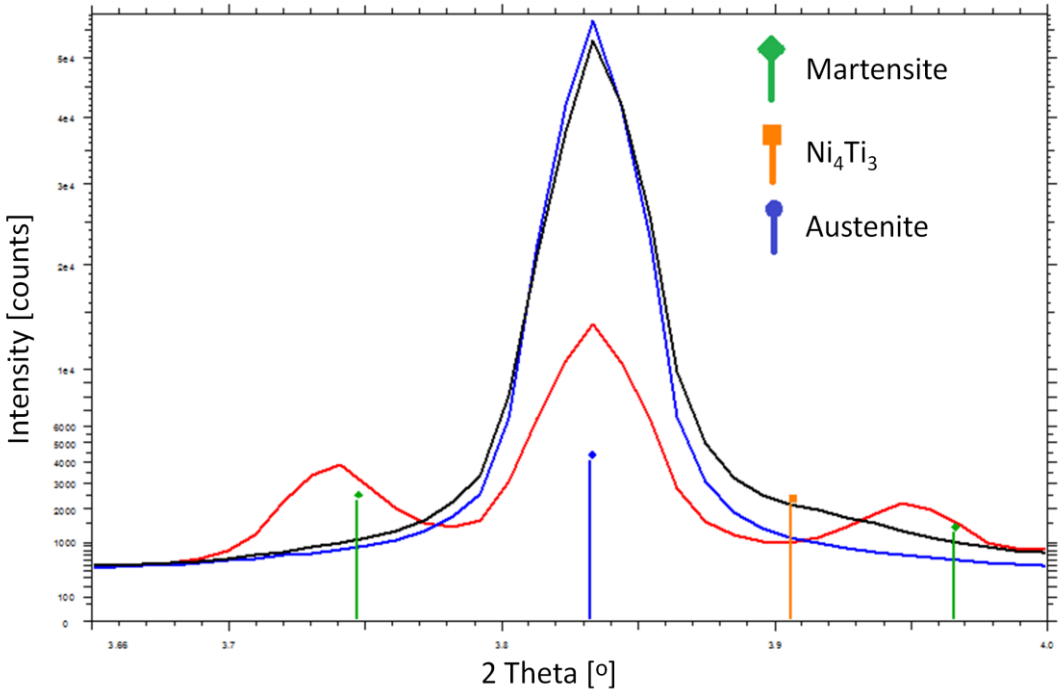

Figure 58 – Superposition of three different diffractograms corresponding to three different zones of samples B-B: blue corresponds to the BM; red corresponds to FZ; black corresponds to the HAZ.

Regarding the differences between the cycling tests of samples A-A, B-B and C-C the following was observed:

Sample A-A exhibits a smooth transition from the elastic part to the superelastic plateau. The existence of martensite in the HAZ and in the FZ, as depicted by the XRD analysis, may explain this behavior. The smooth transition may be explained as an easy deformation of martensite during "domino detwinning". The weld bead has a softening effect at the beginning of the

superelastic plateau, which causes more elongated loops and, as a consequence, the absorbed energy per loop decreases.

The cycling test for sample B-B shows the existence of R-phase. This can be explained since in the XRD analysis performed on the BM at different temperatures, there is evidence of R-phase near room temperature and this is consistent with the DSC data for the BM. Knowing that the thermal hysteresis for the R-phase transformation is very small [33], and since the range of temperatures at which the transformation austenite ⇔ R-phase is very close to room temperature (R_s = 15 °C, upon cooling and A_f = 24 °C, upon heating, as it can be depicted from the DSC analysis), any slight variation in the temperature at which the cycling tests were performed, may induce the existence of some R-phase.

Sample B-B also exhibits two different plateaus associated with SIM. These plateaus, however, are only noticed in the early cycles of the first set of cyclic tests. The existence of these plateaus can be explained by recrystallization that is known to affect the critical stress for SIM. In particular, it tends to decrease the critical stress to induce SIM. [34] For these samples the thermal cycle may cause recrystallization to happen in the austenite of the HAZ, while austenite in the BM was not affected. This means that the austenite in the HAZ will transform into martensite at a lower stress level than the austenite in the BM. Despite the existence of two superelastic plateaus, sample B-B also exhibits the smooth transition mentioned for sample A-A.

Sample C-C has a similar behavior as sample A-A. However, when compared to sample B-B, the fourth set of cyclic tests of sample C-C just showed elastic deformation while for samples A-A and C-C there is still evidence of the superelastic plateau. This is due to the accumulated irrecoverable strain of each sample, which tends to vary between samples, as discussed previously.

4.1.1.2 - Influence of Welding Speed for a Laser Power of 1485 W

Analyzing comparatively samples welded with a laser power of 990 W and 1485 W the main difference is observed in the evolution of the accumulated irrecoverable strain. For this reason we first discuss this behavior and after the existing differences in the cycling tests of these samples.

The evolution of the accumulated irrecoverable strain for those samples (Figure 59) depict that samples D-D and E-E have a similar behavior which is also similar to sample C-C. On the other hand, sample F-F has a similar behavior to sample B-B. The reason why there is two different behaviors (one like the one presented by samples C-C, D-D and E-E and the other like the one presented by sample B-B and F-F), may be due to the HI introduced during the welding and because of geometrical constraints of the weld bead and will be discussed later.

It was noticed for these that samples the one with lower HI (sample F-F) has a lower irrecoverable strain, which is the opposite behavior to the one present in the first set of samples (A-A, B-B and C-C). This is due to the combined influence of the HI and the weld bead geometry and will be discussed later.

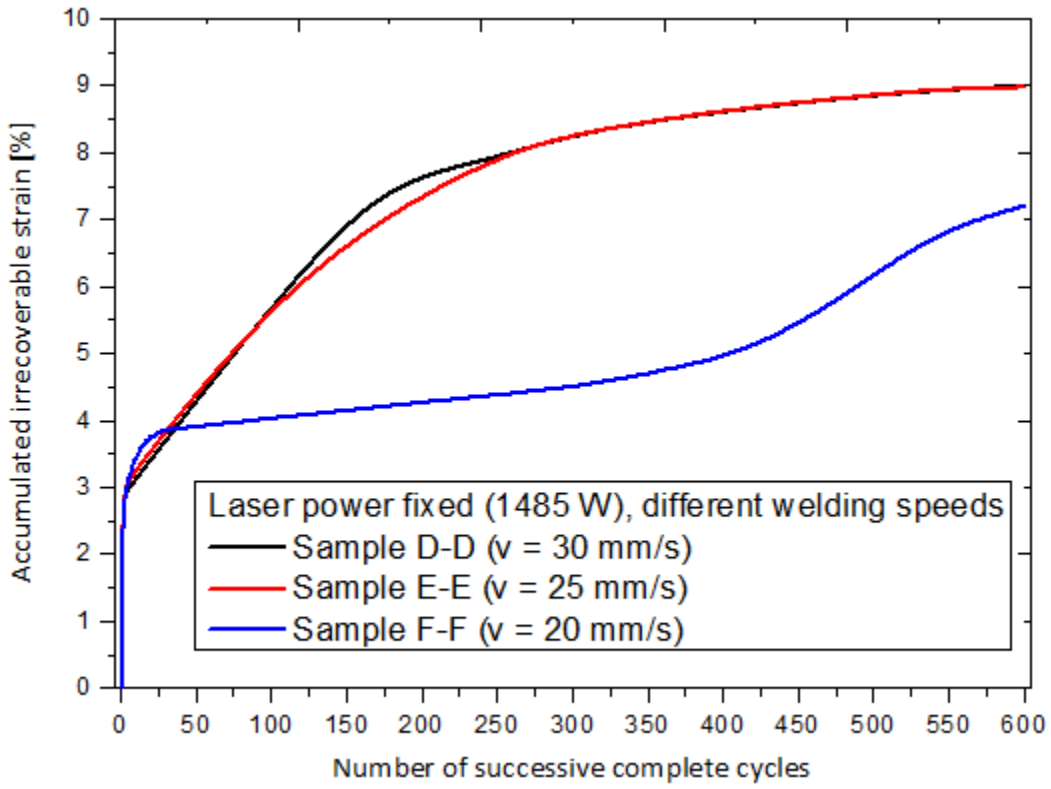

Figure 59 – Comparison between the accumulated irrecoverable strain over the number of successive cycles for samples D-D, E-E and F-F.

The reason why samples D-D and E-E have the same behavior regarding the evolution of accumulated irrecoverable strain is partially explained by the amount of martensite existent in the FZ and in the HAZ. XRD of these zones for these samples showed that the difference in the relative amount of martensite was negligible. On the other hand, sample F-F has a lower amount of martensite in those regions, which explains that the accumulated irrecoverable strain is lower than for samples D-D and E-E. Sample F-F, although corresponding to a higher HI than D-D and E-E, does not have a higher amount of martensite, as it would be expected. The reason for this will be discussed later.

From the cycling tests it is withdrawn that the behavior of these samples is similar to the ones presented by samples A-A, B-B and C-C. However, it must be noticed that for sample F-F there is a slight variation in the slope of the elastic part of the curve around 250 MPa. This effect may be due to recrystallization phenomena, which were not manifested by the existence of double plateau as for sample B-B, mentioned before.

By comparing the evolution of the accumulated irrecoverable strain, it is noticed that there is a different behavior between the analyzed samples. That difference may be due to the welding speed chosen for each sample. Regarding the cycling tests of the analyzed samples, there is no significant differences, existing only some samples that present recrystallization phenomena, due to the welding procedure, more clearly than others.

4.1.2 - Influence of the Laser Power For a Fixed Welding Speed

As stated before the cycling tests do not appear to be specially influenced by the welding parameters. Instead, the evolution of the accumulated strain with the number of cycles shows a different behavior for some of the welded samples. For this reason the discussion that will be resumed will take only in consideration the influence of the welding parameters, in this case the influence of the laser power, on the evolution of the accumulated irrecoverable strain.

4.1.2.1 - Influence of Laser Power for a Welding Speed of 25 mm/s

Samples A-A and E-E were welded with a welding speed of 25 mm/s and a laser power of 990 and 1485 W. The evolution of the accumulated irrecoverable strain for these samples is depicted in Figure 60.

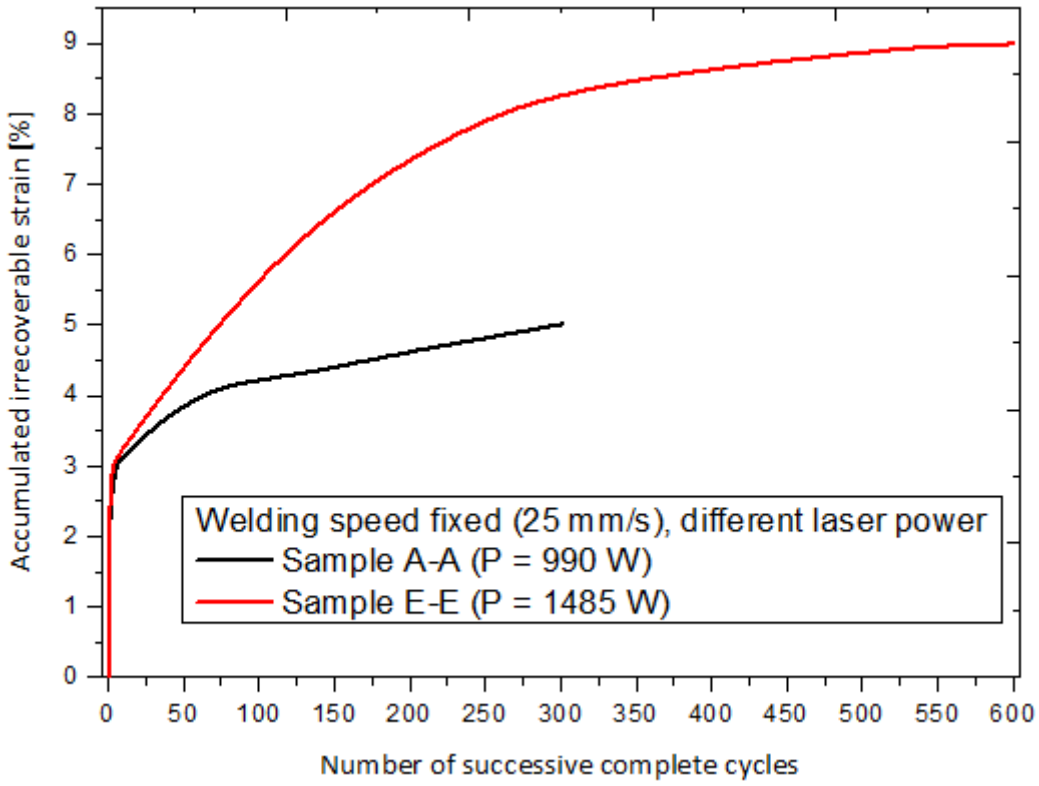

Figure 60 – Comparison between the accumulated irrecoverable strain over the number of successive cycles for samples A-A and E-E.

It must be noticed that samples A-A and E-E exhibit a similar behavior of the accumulated irrecoverable strain up to 100 cycles. After sample E-E shows a tendency to decrease the slope of the curve while sample A-A it is the opposite behavior. Above 301 cycles it is not possible compare both behaviors since sample A-A suffered premature rupture. However, it can be inferred that after those cycles sample A-A did not show any tendency to stabilize the accumulated irrecoverable strain, as it was observed in sample E-E. Sample E-E presents a tendency to a stabilization of the accumulated irrecoverable strain to a constant value of about 8.99%.

4.1.2.2 - Influence of Laser Power for a Welding Speed of 20 mm/s

Samples B-B and F-F were welded with a welding speed of 20 mm/s and a laser power of 990 and 1485 W, respectively. The evolution of the accumulated irrecoverable strain for these two samples is depicted in Figure 61.

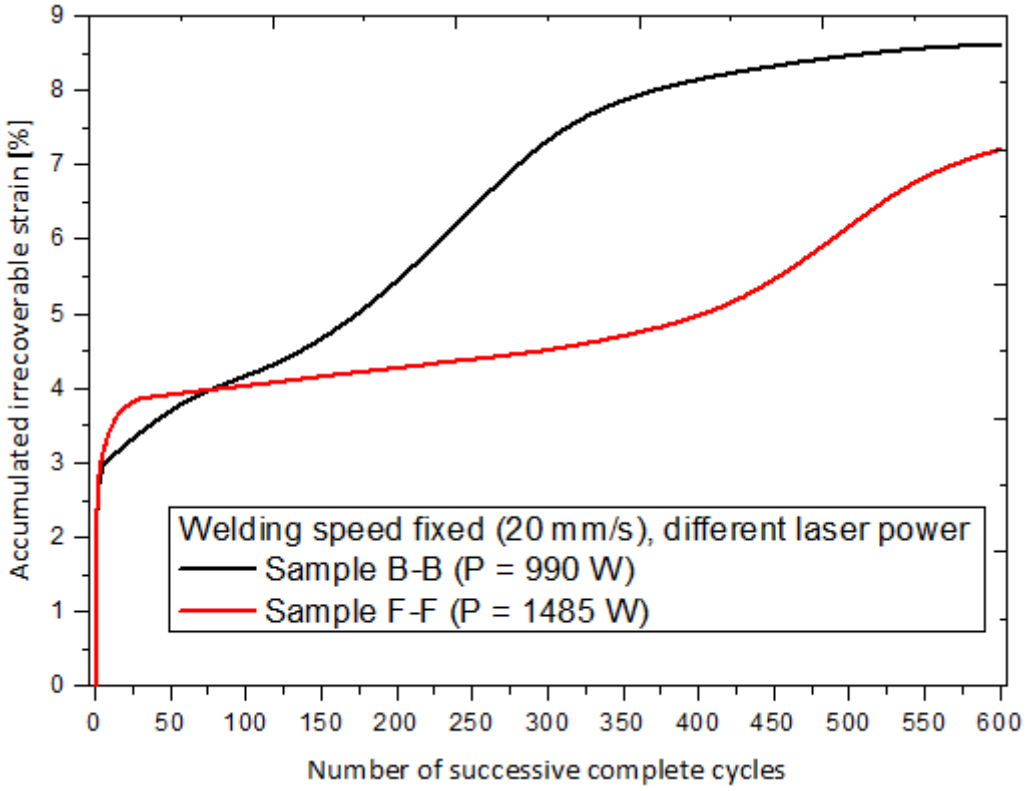

Figure 61 – Comparison between the accumulated irrecoverable strain over the number of successive cycles for samples B-B and F-F.

As for samples B-B and F-F there is no evidence of a well defined behavior. Sample B-B has a total of four abrupt changes (the first one from the 1st to the 10th cycle; the second one from the 11th to the 110th cycle; the third one from the 111th cycle to the 350th cycle; and the forth one from the 351st until the last cycle). Sample F-F exhibits three abrupt changes (the first one from 1st to the 30th cycle; the second one from the 31st to the 420th cycle; and the last one from the 421st until the last cycle). It is especially notorious that the second abrupt change for sample F-F is characterized by a plateau where the accumulated irrecoverable strain appears to stabilize but after there is a large increase in the accumulated irrecoverable strain without any indication of a possible stabilization to a constant value.

When compared to the influence of the welding speed for a fixed laser power it appears that it is easier to compare the evolution of the accumulated irrecoverable strain by fixing a laser power and varying the welding speed.

As it was present above there is some correlation between the samples analyzed previously (section “Influence of the Welding Speed for a Fixed Laser Power”), while in this section there

is no apparent relationship between the analyses performed for the couple samples A-A and E-E and B-B and F-F.

4.1.3 - Effect of the Heat Input

The analysis of the behavior of the welded samples by accessing the influence of the welding speed for a fixed laser power and vice-versa, leads to the existence of differentiated situations, depending on the sample. This may lead to an error when choosing which welding parameter most influences the behavior of the welded samples. For that reason, will be discussed the influence of the HI introduced during the welding procedure. The HI is a combination of the single parameters analyzed previously (welding speed and laser power).

It was already mentioned that the stabilized behavior is easier to be achieved by fixing the laser power and varying the welding speed. Taking this in consideration we now discuss how the HI introduced during the welding may or may not lead to a good behavior, like the one presented by samples C-C, D-D and E-E. Good behavior means that there are no abrupt changes in the evolution of the accumulated irrecoverable strain and that there is a convergence to a constant value after a certain number of cycles performed.

Figure 62 [23] depicts that the weld bead width on the face and on the root had a parabolic behavior with the HI. Between 500 and 675 J/cm, approximately, there is a local maximum.

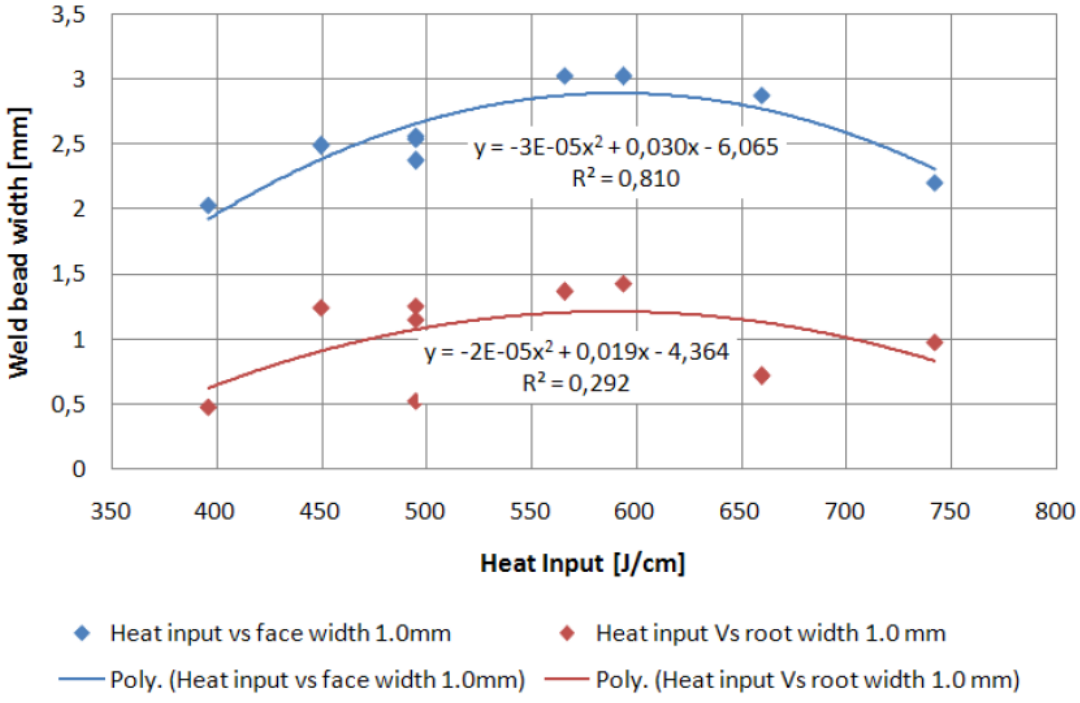

Figure 62 – Relation of the welding power and the width between face and root for the same heat input. [23]

The samples with the best mechanical behavior have a HI value in this range. Particularly C-C has 660 J/cm, D-D 495 J/cm (which is a value very close to the lower limit) and E-E with 594 J/cm. On the other hand samples that did not have a good relation regarding the evolution of the accumulated irrecoverable strain have values of HI outside the mentioned range. In particular sample A-A has 396 J/cm, sample B-B has 495 J/cm and sample F-F 743 J/cm.

In fact sample F-F, was expected to have more martensite than samples D-D and E-E, as mentioned before, due to a higher value of HI when comparing those two samples. However, existing geometrical constraints, which are translated in this case for a lower width of the weld bead, when comparing with samples D-D and E-E, justify the existence of a smaller amount of martensite for sample F-F.

Despite samples B-B and D-D have the same value of HI (495 J/cm) their behavior is not the same. This may be explained taking into consideration that this value of HI is slightly lower than the lower limit of 500 J/cm mentioned before. This may be indicative that outside the range where the local maximum is defined, but, near those values it is possible to have a good behavior. However, it may not be present every single time. In order to avoid this situation the HI should be higher than 500 J/cm but lower than 675 J/cm.

It is also known that, in laser welding, there are two distinctive modes: keyhole and conduction mode. The power density during welding was of about 0.1556 and 0.2334 MW/cm^2, for the samples welded with 990 and 1485 W, respectively. According to [35] for these values of power density we have a transition mode from conduction to keyhole mode, meaning that we have a mix of both methods during welding. This is also clear by analyzing the width in the face and in the root. The difference between the width in the face and in the root can reach up to four times, which is consistent with the existence of a conduction mode in the face and a keyhole mode in the root.

This geometrical feature may also influence the behavior of the accumulated irrecoverable strain. In particular it is noticed that the samples with lower widths in the face and in the root, those which the HI value is outside the stabilization range, have a random behavior. Though it is frequently mentioned that laser welding is a suitable joining technique because it reduces the extension of the FZ and the HAZ, it may be not fully true, since for some situations a better behavior is exhibited for a wider extent of FZ and HAZ.

The reason why the samples with higher HAZ and FZ present a better behavior can be explained as follows: it is known that laser welding alters significantly the microstructure of the welds. These alterations may have a smooth transition from the HAZ to the BM giving a more extended zone affected by the thermal cycling. On the other hand, samples with a narrower extent of HAZ and FZ will show a sharper transition when reaching the BM, which may explain the irregularities observed in the evolution of the accumulated irrecoverable strain.

The XRD analysis performed on Petra III, for samples A-A and C-C, which allowed a very localized structural analysis in the weld bead and neighboring regions, also confirms the influence of the HI. Figure 63 depicts the plots of intensity vs azimuthal angle, ϕ, for the crystallographic planes {110}, {111} and {211}.

In the BM and in the HAZ (columns on the left and in the middle, respectively) there is a similar trend indicating that the texture of these two zones should not differ significantly. However, closer to the FZ (right column), it is possible to detect spikes in correspondence to spotty Debye-Scherrer rings (see Figure 66). This feature is more clearly noticed for the crystallographic plane {110} for sample C-C, although the trend is similar in both samples. The

higher values of intensity measured for sample C-C are due to grain coarsening resulting from a higher value of HI also resulting on a larger extension of HAZ and FZ.

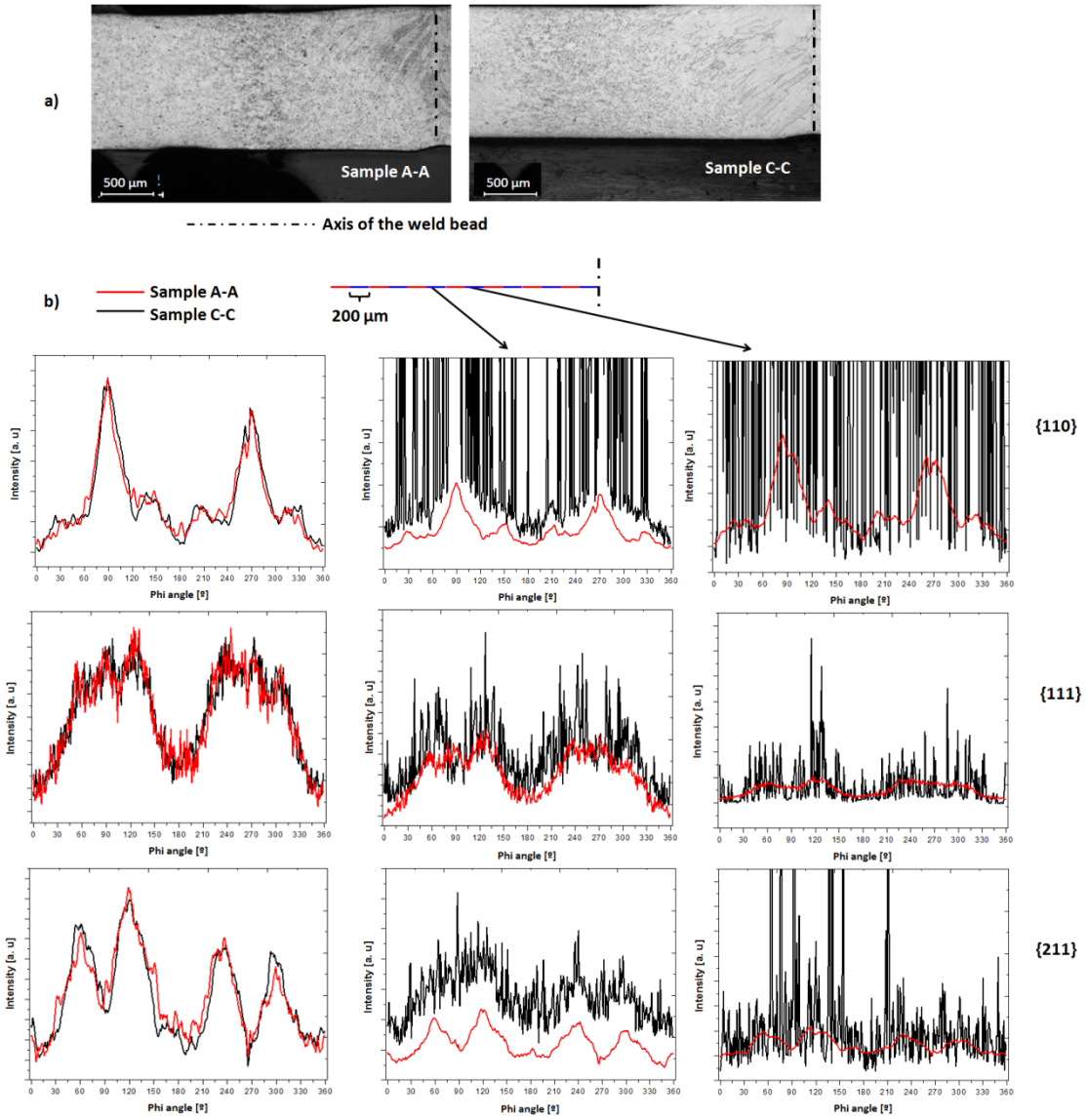

Figure 63 – Plots of intensity vs ϕ angle for different crystallographic planes in samples A-A and C-C.

The Debye-Scherrer rings for samples A-A and C-C in the BM, HAZ and in the FZ are presented in Figures 64 to 66, respectively.

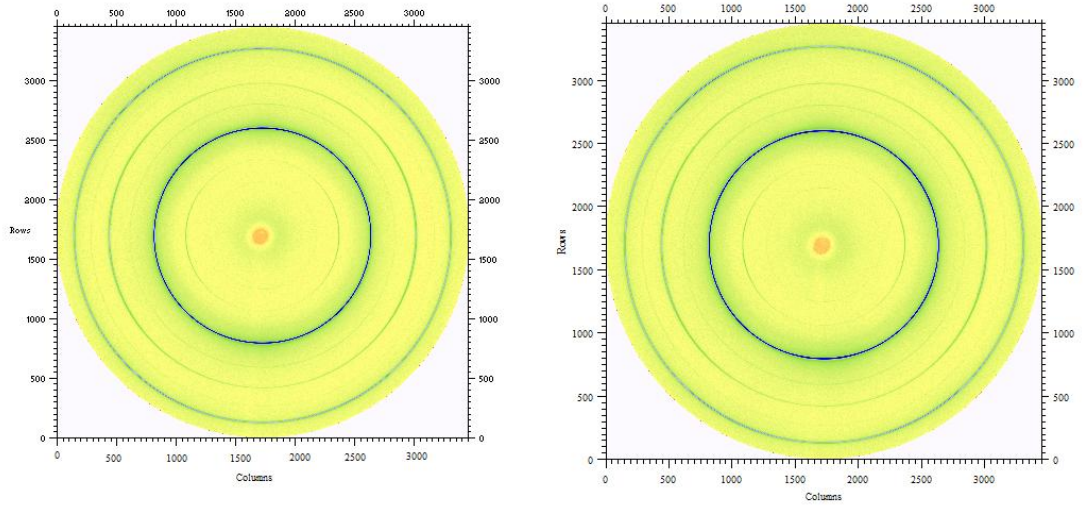

Figure 64 – Debye-Scherrer rings from the base material for samples A-A (on the left) and C-C (on the right).

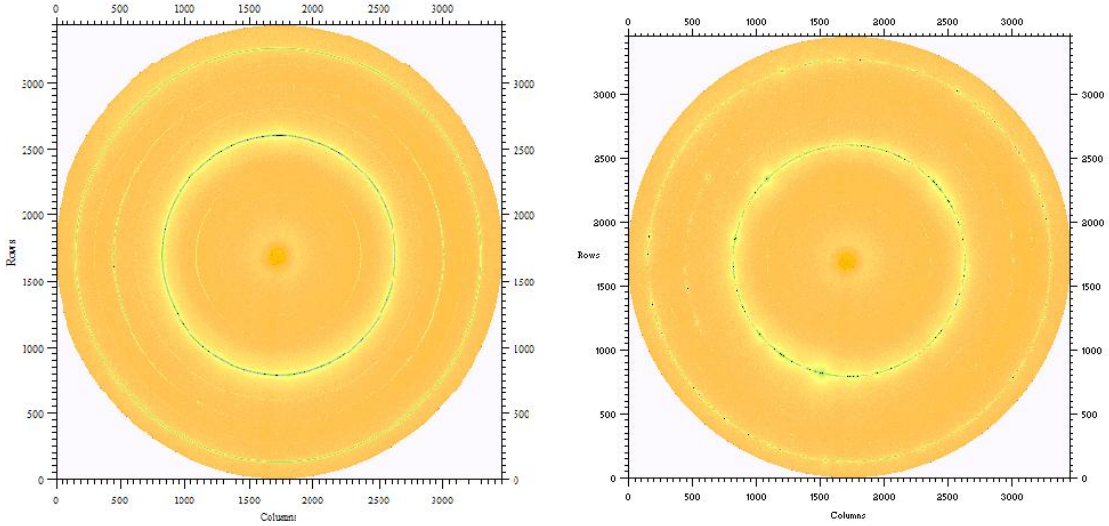

Figure 65 – Debye-Scherrer rings from the heat affect zone for samples A-A (on the left) and C-C (on the right).

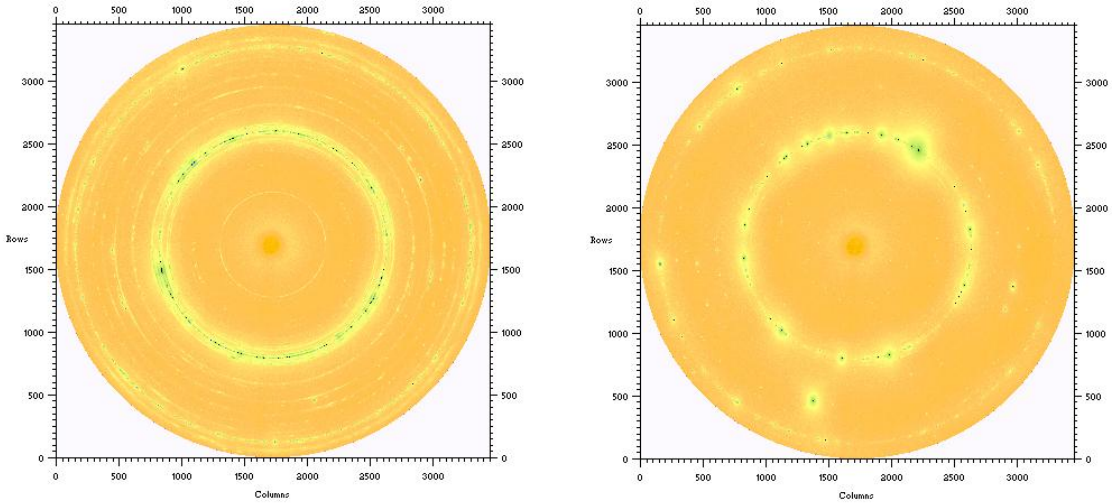

Figure 66 – Debye-Scherrer rings from the fusion zone for samples A-A (on the left) and C-C (on the right).

Debye-Scherrer rings in Figure 64 are rings very well defined for both samples. However, in Figure 65 for sample C-C there are spotty zones, while for sample A-A there is still no evidence of that. This is due to larger extension of the affected zones due to the welding process, which are more extensive for sample C-C as a result of higher HI, which makes the spotty Debye-Scherrer rings appear at a distance further to the axis of the weld bead when comparing to sample A-A. In Figure 66 both samples present the already mentioned spotty Debye-Scherrer rings as a result of the existence of a coarse grain microstructure in the FZ.

Sample H-H, due to specificity of the welding parameters used during its welding was not yet compared by any means with any other sample. However, regarding the cycling tests, its behavior does not differ significantly from the other samples the same happening for the evolution of the accumulated irrecoverable strain. Its premature rupture in the weld bead, after 45 cycles, without any evidence of fatigue may, however, indicate that the welding parameters are not adequate for having good mechanical characteristics. Sample H-H also has the same HI as samples B-B and D-D, however its bad mechanical behavior may indicate that its laser parameters (high laser power and high welding speed) are not suitable for promoting good cycling properties.

4.1.4 - SEM Analysis of Fracture Surfaces

The SEM observations from samples A-A and H-H allow us to understand that the beginning of the fracture has a ductile character due to the existence of very large amount of dimples. [36] For sample A-A that suffered rupture at 301 cycles, there is evidence of the propagation of the crack due to fatigue, which is visible in Figure 53 (in “Experimental Results” Chapter).

At the end of the fracture, both samples show a catastrophic propagation of the cracks which lead to the failure under mechanical cycling. It must be noticed that the rupture of sample A-A occurred in the BM, most probably be due to some irregularity pre-existent on the surface of the sample before the mechanical cycling.

Since the objective of this Thesis was not to evaluate the failure mechanisms of the welded samples, no further comments about the fracture surfaces of these samples will be made.

4.2 - 0.5 mm thick samples

As mentioned before, due to shortage of samples, the discussion will be made taking only in consideration the effect of the HI in the mechanical properties of 0.5 mm thick samples.

The samples analyzed show a great disparity in the number of cycles that were able to stand. While sample K-K was able to stand the entire 600 cycles, samples F-F and O-O suffered premature rupture in the BM after 35 and 38 cycles, respectively. For that reason, the comparison between the evolution of the accumulated irrecoverable strain of these samples will be made by analyzing the behavior of samples F-F and O-O until rupture and sample K-K until 38 cycles, so that a real comparison may be possible. After, we present the full evolution of the accumulated irrecoverable strain for sample K-K and the existing difference between the cycling tests of all samples.

4.2.1 - Effect of the Heat Input

The evolution of the accumulated irrecoverable strain for all samples to a maximum of 38 cycles is depicted in Figure 67. As for the 1.0 mm thick samples the quick increase of the accumulated irrecoverable strain in the early cycles is due to martensite stabilization. This is corroborated by the XRD analysis performed on these samples that show the existence of martensite in the FZ and in the HAZ. The increase of the accumulated irrecoverable strain may be explained taking into consideration what was discussed for the 1.0 mm thick samples and for that reason no more comments about that will be made.

The curve corresponding to sample F-F (with higher HI), depicts higher values of accumulated irrecoverable strain, while sample O-O (with lower HI), depicts lower values. This may be due to the existence of more martensite in sample F-F due to a higher value of HI. For 0.5 mm thick samples it was not possible to compare qualitatively the amount of martensite of each sample. This is due to lower thickness of the samples and to the existence of coarse grain, which makes difficult to discern about the relative amounts of martensite for each sample. However, it is expected, taking in consideration Figure 67, that sample F-F has a higher amount of martensite, while sample O-O has the lower amount of martensite. Sample K-K should have an intermediate amount of martensite since its curve lays between the ones of samples F-F and O-O.

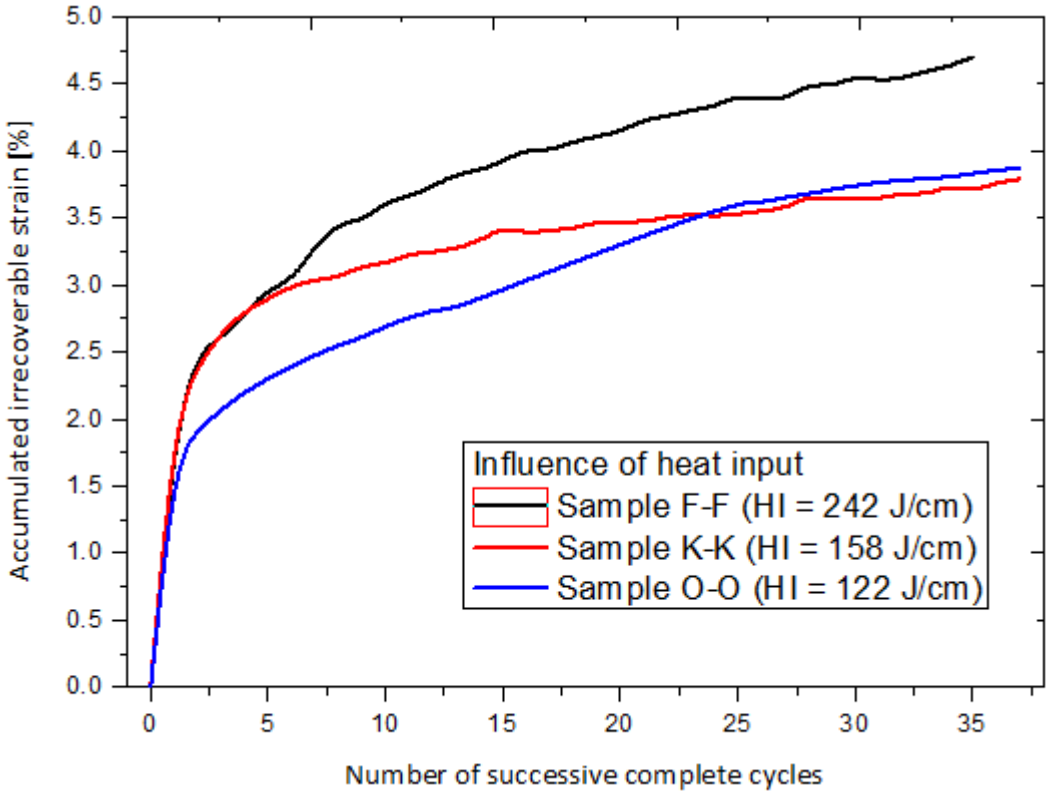

Figure 67 – Comparison between the accumulated irrecoverable strain over the number of successive cycles for samples F-F, K-K and O-O.

The fact that samples F-F and O-O suffered premature rupture at a low number of cycles when comparing to sample K-K, may be due to the existence of some heterogeneities in the BM, which may have facilitated the initiation and the propagation of the fracture.

The full evolution of the accumulated irrecoverable strain with the number of cycles for sample K-K is presented in Figure 68.

It is clear that the behavior presented by this sample is similar to the ones presented by 1.0 mm thick samples which had what was considered a good behavior. The stabilization of the accumulated irrecoverable strain starts to occur around 350th cycle, which is earlier than for 1.0 mm thick samples, and it stabilized to a value of 7.85%.

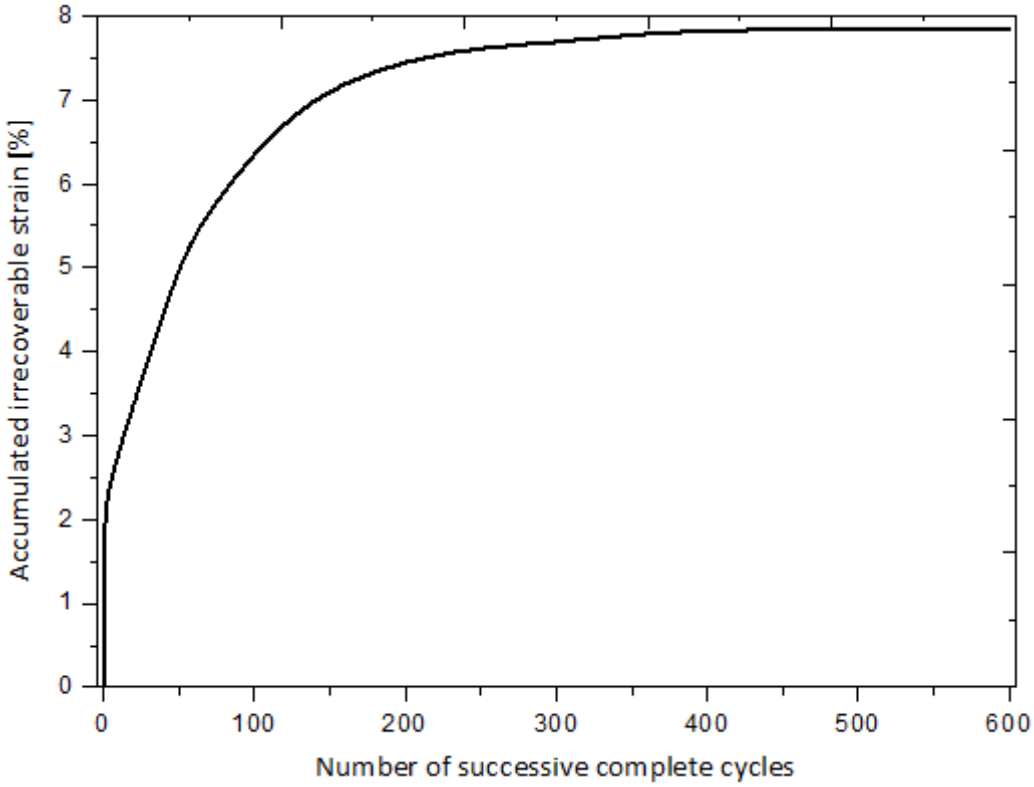

Figure 68 – Evolution of the accumulated irrecoverable strain for sample K-K.

Comparing the cycling tests of each sample, it is clear that in the first set of cyclic tests there is a clear definition of the superelastic plateau for all samples. The general comments made for the 1.0 mm thick samples apply for these samples.

Sample K-K in the fourth set of cyclic tests only presents an elastic behavior without any evidence of the superelastic plateau. On the next set, it only presents the start of the superelastic plateau due to the increase of the accumulated irrecoverable strain until that set of cyclic tests.

4.3 - Shape Memory Effect Evaluation

As presents before all samples recovered their initial shape, except for sample that was welded perpendicular to the rolling direction. However on this sample there was a lack of penetration in the root up to 20% in material thickness, and even so this sample was able to stand to the complete SME test despite the tensile forces on the root.

For the other samples the return to its original shape occurred in less than 1 minute, without any help of a heater, which is a remarkable result.

The weld thermal cycle experienced by the material fully destroys its initial structure in the FZ. In the HAZ the thermal cycle is variable according to the distance to the weld centerline. However, a confinement effect exists due to the very narrow region where transformations occur, thus, in the mesoscale, the material retains its initial shape. It must be noticed that the shape memory recovery may have occurred mostly because the local deformation did not exceed the maximum recoverable strain by the SME.

The results of the SME tests performed on the cycled samples let us conclude that part of the accumulated irrecoverable strain imposed during the cycling tests may in fact be recovered. However, what we can only control, regarding the initial shape of the samples, is the distortion imposed during the mechanical cycling and that distortion is recovered when performing the SME tests or just my heating up the samples above A_f. We do not control, however, the elongation of the samples, so it is not possible to say that all the strain imposed to the samples during the cycling tests can be recovered, but some part of it is recovered, as mentioned before.

5 - Conclusions and Future Work

The effect of the welding parameters on the SE and SME properties of NiTi similar welds was studied. In this work the mechanical behavior under cycling of the welded samples was analyzed and was interpreted taking into consideration the studies conducted about the microstructure of the welds in its different regions (MB, HAZ and FZ).

For 1.0 mm thick samples it was shown that the welding parameters influence the number of cycles that the samples were able to resist and the evolution of the accumulated irrecoverable strain. Concerning the HI introduced during welding, there is a specific range of values where good mechanical behavior may be obtained. Within this range optimization should be done by fixing a laser power and varying the welding speed. Outside this range the behavior is not very well defined. Laser powers of 990 and 1485 W are suitable for having good mechanical properties in the weld joints. However, very high values of laser power (1980 W) combined with very high welding speeds, are not suitable for the successful joining of these alloys. All samples show a great resistance to the cycling tests performed (600 cycles), except the one welded with a laser power of 1980 W (45 cycles).

Microstructural changes in the FZ and in the HAZ were also identified by XRD, where it was possible to observe the existence of both martensite and austenite, while the BM was austenitic. These microstructural alterations are associated to a shift of the M_s temperature, which is then above room temperature. In the FZ the existence of martensite at room temperature, is due to a preferential evaporation of Ni, which causes a Ti enrichment of the material, thus leading to a raise of the M_s temperature. For the HAZ the thermal cycle imposed during the welding procedure enables Ni-rich precipitation, like Ni_4Ti_3, which causes an enrichment in the surrounding matrix and a shift of M_s to higher temperatures.

The existence of martensite in the FZ and in the HAZ does not prevent strain recover by superelastic behavior of the remaining material (BM). For every sample, a superelastic plateau was observed during the mechanical cycling. However, the existence of martensite leads to a significant increase of the accumulated irrecoverable strain during the early cycles. After a certain number of cycles, the stabilization of the accumulated irrecoverable strain is reached. Part of irrecoverable strain imposed to martensite during the cycling tests may, in fact, be recovered as the results from the SME of the cycled samples show. Since the range of temperatures where the transformation austenite $\Leftrightarrow$ R-phase occurs is very close to room temperature, in some of the mechanical tests it could be noticed the effect of the existence of R-phase.

The thermal cycle imposed during the welding procedure induce recrystallization phenomena in the HAZ. This effect can be noticed in the cycling tests and can be translated by a change of the slope in the region before reaching the superelastic plateau or even with the existence of double superelastic plateau.

For 0.5 mm thick samples a set of three different HI values was studied, with no common values of power and/or welding speed which limited the study. These samples have more heterogeneities than the 1.0 mm thick samples, which may explain its premature rupture. The sample that did not break until the end of the cycling routine depicts a good behavior in terms

of the accumulated irrecoverable strain, meaning that the welding parameters used are suitable for a successful joining.

The shape memory evaluation showed that the welded samples do exhibit SME after welding. Even after mechanical cycling of laser welds that did not break, SME is observed. It must be noticed that the shape memory recovery occurs in less than 1 minute. The permanent deformation angle (2°) exhibited by one of the samples may be explained by the existence of welding defects: lack of penetration up to 20% in material thickness.

Regarding future work, as it was mentioned, a specific laser power and/or welding speed influence the thermal cycle during welding. It would be interesting to model these phenomena and its influence on this class of materials (NiTi alloys). The use of fatigue machines to access the fatigue strength of the samples and its correlation with the welding parameters would also be interesting. This would be useful for possible applications of this technique for joining this kind of alloy for the aerospace industry, for example.

Other protocols of cycling tests may also be studied. In particular, after each set of cycling tests, it would be interesting to stabilize thermal and mechanically the samples before imposing another set of cyclic tests. The effect of the temperature at which the mechanical cycling is carried out may also be studied. For instance, it would be interesting to cycle the samples when they are fully austenitic and compare the results between the tests performed at room temperature and at high temperature.

The effect of heat treatments on the welded samples could also be studied in order to suppress the R-phase, taking in consideration the specificity of the desired applications.

6 - References

[1] D. C. Lagoudas, *Shape Memory Alloys: Modeling and Engineering Applications*. Springer, 2008.

[2] W. J. Buehler, J. V. Gilfrich, and R. C. Wiley, "Effect of Low Temperature Phase Changes on the Mechanical Properties of Alloys near Composition TiNi," *Journal of Applied Physics*, vol. 34 (1963), pp. 1475 –1477.

[3] K. Otsuka and X. Ren, "Physical metallurgy of Ti–Ni-based shape memory alloys," *Progress in Materials Science*, vol. 50 (2005) pp. 511–678, Jul. 2005.

[4] J. Ryhänen, E. Niemi, W. Serlo, E. Niemelä, P. Sandvik, H. Pernu, and T. Salo, "Biocompatibility of nickel-titanium shape memory metal and its corrosion behavior in human cell cultures," *Journal of Biomedical Materials Research*, vol. 35 (1998) pp. 451–457.

[5] J. A. Shaw and S. Kyriakides, "Thermomechanical aspects of NiTi," *Journal of the Mechanics and Physics of Solids*, vol. 43 (1995) pp. 1243–1281.

[6] P. Sittner, Y. Liu, and V. Novak, "On the origin of Lüders-like deformation of NiTi shape memory alloys," *Journal of the Mechanics and Physics of Solids*, vol. 53 (2005) pp. 1719–1746.

[7] G. Tan and Y. Liu, "Comparative study of deformation-induced martensite stabilisation via martensite reorientation and stress-induced martensitic transformation in NiTi," *Intermetallics*, vol. 12, (2004) pp. 373–381.

[8] J. Ryhänen, *Biocompatibility Evaluation of Nickel-titanium Shape Memory Metal Alloy,* PhD dissertation presented at the Faculty of Medicine,, 1999.

[9] K. Otsuka and C. M. Wayman, Eds., *Shape Memory Materials*. Cambridge University Press, 1999.

[10] W. M. Steen and J. Mazumder, *Laser Material Processing*. Springer, 2010.

[11] K.-H. Grote and E. K. Antonsson, Eds., *Springer Handbook of Mechanical Engineering*, 1st ed. Springer, 2009.

[12] L. Quintino, A. Costa, R. Miranda, D. Yapp, V. Kumar, and C. J. Kong, "Welding with high power fiber lasers – A preliminary study," *Materials & Design*, vol. 28 (2007) pp. 1231–1237.

[13] A. Falvo, F. M. Furgiuele, and C. Maletta, "Functional behaviour of a NiTi-welded joint: Two-way shape memory effect," *Materials Science and Engineering: A*, vol. 481–482 (2008) pp. 647–650.

[14] A. Falvo, F. M. Furgiuele, and C. Maletta, "Laser welding of a NiTi alloy: Mechanical and shape memory behaviour," *Materials Science and Engineering: A*, vol. 412 (2005) pp. 235–240.

[15] X. J. Yan, D. Z. Yang, and X. P. Liu, "Influence of heat treatment on the fatigue life of a laser-welded NiTi alloy wire," *Mater. Charact.*, vol. 58 (2007) pp. 262–266.

[16] B. Tam, M. Khan, and Y. Zhou, "Mechanical and Functional Properties of Laser-Welded Ti-55.8 Wt Pct Ni Nitinol Wires," *Metallurgical and Materials Transactions A*, vol. 42 (2011) pp. 2166–2175.

[17] H. Gugel, A. Schuermann, and W. Theisen, "Laser welding of NiTi wires," *Mater. Sci. Eng. A-Struct. Mater. Prop. Microstruct. Process.*, vol. 481 (2008) pp. 668–671.

[18] C. Chan, H. Man, and T. Yue, "Effects of Process Parameters upon the Shape Memory and Pseudo-Elastic Behaviors of Laser-Welded NiTi Thin Foil," *Metallurgical and Materials Transactions A*, vol. 42, (2011) pp. 2264–2270.

[19] Y. G. Song, W. S. Li, L. Li, and Y. F. Zheng, "The influence of laser welding parameters on the microstructure and mechanical property of the as-jointed NiTi alloy wires," *Mater. Lett.*, vol. 62 (2008) pp. 2325–2328.

[20] A. Tuissi, S. Besseghini, T. Ranucci, F. Squatrito, and M. Pozzi, “Effect of Nd-YAG laser welding on the functional properties of the Ni–49.6at.%Ti,” *Materials Science and Engineering: A*, vol. 273–275 (1999) pp. 813–817.

[21] L. A. Vieira, F. M. B. Fernandes, R. M. Miranda, R. J. C. Silva, L. Quintino, A. Cuesta, and J. L. Ocaña, “Mechanical behaviour of Nd:YAG laser welded superelastic NiTi,” *Materials Science and Engineering: A*, vol. 528 (2011) pp. 5560–5565.

[22] E. A. Brandes and G. B. Brook, Eds., *Smithells Metals Reference Book, Seventh Edition*, 7th ed. Butterworth-Heinemann, 1998.

[23] L. M. A. Vieira, “Laser welding of shape memory alloys”, MSc Thesis on Mechanical Engineering presented at Faculdade de Ciência e Tecnologia da Universidade Nova de Lisboa, 2010. [Online]. Available: http://run.unl.pt/handle/10362/4760. [Accessed: 10-May-2012]

[24] “Nitinol Technical Properties.” [Online]. Available: http://jmmedical.com/resources/221/Nitinol-Technical-Properties.html. [Accessed: 24-May-2012].

[25] G. Höhne, W. Hemminger, and H.-J. Flammersheim, *Differential Scanning Calorimetry*. Springer, 2003.

[26] B. D. Cullity, *Elements of X-ray Diffraction*, 2nd ed. Addison-Wesley Publishing Company, 1978.

[27] “Bragg’s Law reflection.” [Online]. Available: http://serc.carleton.edu/research_education/geochemsheets/BraggsLaw.html.

[28] A. Hammersley, “Fit2D program.” [Online]. Available: http://www.esrf.eu/computing/scientific/FIT2D/.

[29] H. Tobushi, H. Iwanaga, K. Tanaka, T. Hori, and T. Sawada, “Deformation behaviour of TiNi shape memory alloy subjected to variable stress and temperature,” *Continuum Mechanics and Thermodynamics*, vol. 3 (1991) pp. 79–93.

[30] C. M. Branco, A. A. Fernandes, and P. M. S. T. Castro, *Fadiga de estruturas soldadas*. Fundação Calouste Gulbenkian, 1986.

[31] K. Tanaka, T. Hayashi, Y. Itoh, and H. Tobushi, “Analysis of thermomechanical behavior of shape memory alloys,” *Mechanics of Materials*, vol. 13 (1992) pp. 207–215.

[32] S. Seong, O. Younossi, and B. W. Goldsmith, *Titanium: Industrial Base, Price Trends, and Technology Initiatives*. Rand Corporation, 2009.

[33] J. Uchil, K. Mohanchandra, K. Mahesh, and K. Ganesh Kumara, “Thermal and electrical characterization of R-phase dependence on heat-treat temperature in Nitinol,” *Physica B: Condensed Matter*, vol. 253 (1998) pp. 83–89.

[34] B. Strnadel, S. Ohashi, H. Ohtsuka, T. Ishihara, and S. Miyazaki, “Cyclic stress-strain characteristics of Ti-Ni and Ti-Ni-Cu shape memory alloys,” *Materials Science and Engineering: A*, vol. 202 (1995) pp. 148–156.

[35] E. Assuncao, S. Williams, and D. Yapp, “Interaction time and beam diameter effects on the conduction mode limit,” *Optics and Lasers in Engineering*, vol. 50 (2012) pp. 823–828.

[36] D. Hull, *Fractography: Observing, Measuring and Interpreting Fracture Surface Topography*. Cambridge University Press, 1999.